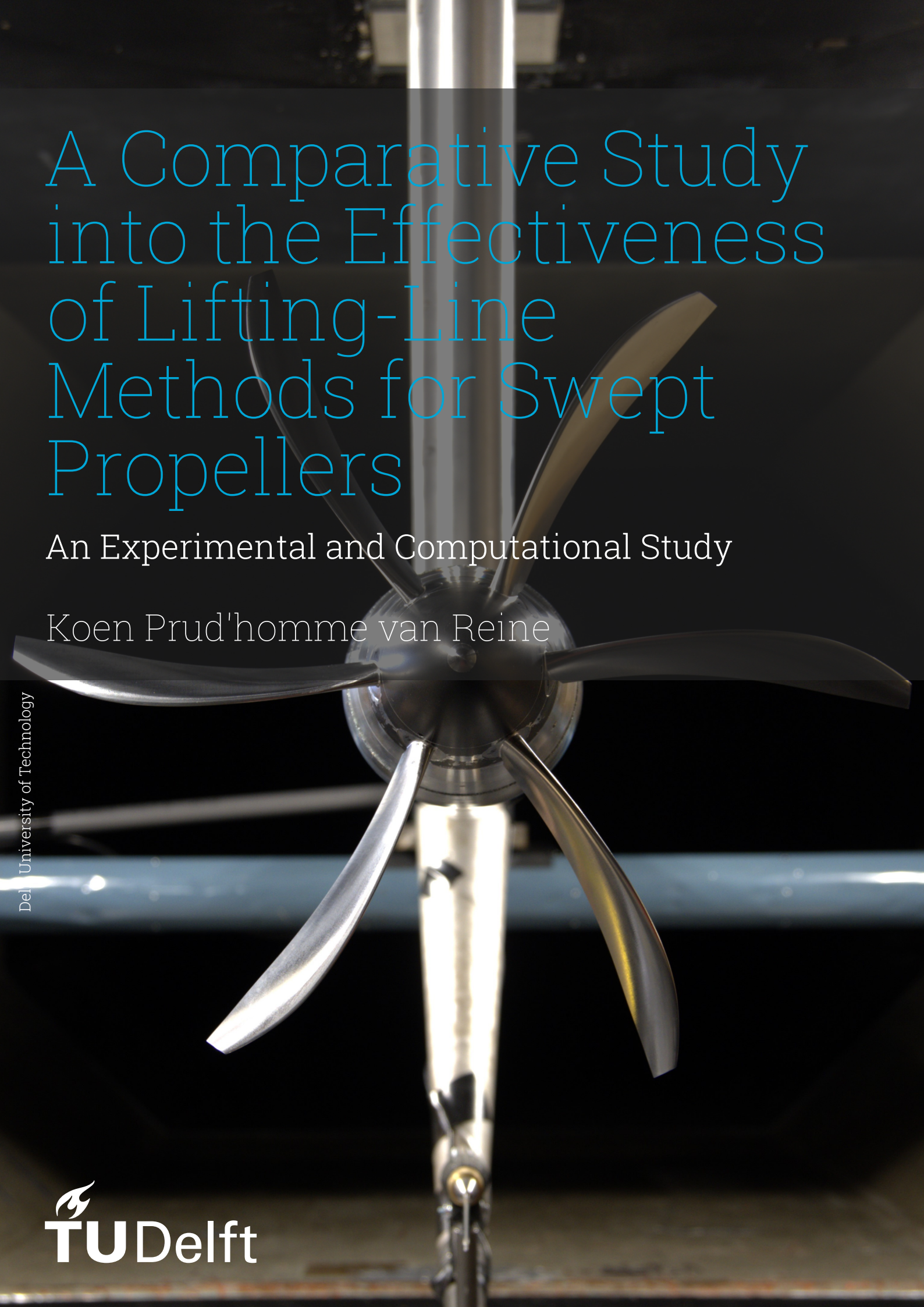

A Comparative Study into the Effectiveness of Lifting-Line Methods for Swept Propellers

An Experimental and Computational Study

Koen Prud'homme van Reine

Delft University of Technology

TU Delft

A Comparative Study into the Effectiveness of Lifting-Line Methods for Swept Propellers

An Experimental and Computational Study

by

Koen Prud'homme van Reine

to obtain the degree of Master of Science
at the Delft University of Technology,
to be defended publicly on Wednesday, 3 September at 14:00

Student number:	4878965	
Project duration:	December 2024 – September 2025	
Thesis committee:	Prof. Dr.-Ing. G. Eitelberg,	TU Delft, Chair
	Dr. ir. T. Sinnige,	TU Delft, Supervisor
	Dr. J. Sodja,	TU Delft, External member

Cover: XPROP-Λ in the Low-Turbulence Tunnel
(Image by Tomas Sinnige)

An electronic version of this thesis is available at http://repository.tudelft.nl/.

TU Delft

Preface

This thesis is the culmination of a project that started in December 2024 and has been a constant presence in my life since then. I started with a singular goal: I wanted to conduct a wind tunnel test as part of my master's thesis. Additionally, I once quite strongly proclaimed my dislike of propellers to a friend of mine and said that I would try to avoid them at all costs. However, I backtracked on this when Tomas proposed the following: an investigation into the effectiveness of low-level aerodynamic models on incorporating the effect of sweep on propeller blades, done by conducting a wind tunnel test for which new blades needed to be drawn in CAD and produced. This seemed too good to be true, and I quickly and gladly accepted his proposal, and the results of that decision lie here before you. I can also quite confidently say that I like propellers now. They are wings and spin, what's not to like?

Over the past few months, I have learned a lot about countless topics. I have learned that nothing is ever as easy as you imagine, that wind tunnel testing is a lot more involved than you see from the outside, that turning a CAD model into a metal part is harder than you imagine, even if you imagine that it is hard. I have learned that the plug-and-play software will neither plug nor play, that modelling is more inaccurate than you fear, and that it was no coincidence that Edward A. Murphy Jr., known for Murphy's law[1], was an aerospace engineer. But I have also learned that there is a lot of value in perseverance, that a can-do attitude and a bit of effort can turn things around, and that an unexpected and disappointing result is not the same as a bad one, when going through a scientific process. Most importantly, this thesis has re-emphasised the importance of a quality I am very glad to possess: The ability to ask for and accept help. There are people around you who know an incredible amount about everything, and more often than not, they will help you, whether that is academically or otherwise. The next paragraphs are here to thank some of them.

First and foremost, I would like to thank my supervisor, Tomas Sinnige, for his great help and advice over the course of this project, as well as for the opportunity to conduct my wind tunnel experiment. This unique experience has been one of the most gratifying of my time in university, and I am forever grateful for his trust and time. I also want to thank Georg Eitelberg for his great help and wealth of experience, as well as our insightful discussions about aerodynamics and his thoughtful words about my disappointment with some of the results and how he re-emphasised their value regardless.

I would also like to thank everyone who participated in the fortnightly propeller research group meetings, which were inspiring and thought-provoking. Major thanks are reserved for Gabriel Margalida, who has been instrumental in this thesis, as he provided the sweep distribution for XPROP-Λ as well as the code for the lifting-line solver. I want to thank the staff of DEMO and the LST for their help with the preparation and execution of the wind tunnel test.

I want to thank my fellow students and friends from the 6th floor, Jack, Bram and Maarten. Special thanks to my good friend Dorothé for being my go-to support for all things (thesis or otherwise) over the past months. You are the only person who specifically asked to be named in the preface, and I cannot think of anyone else who deserves it more than you. Thank you.

Lastly but crucially, I want to thank my parents, without whom I would not be where I am today. Their unconditional love and support are of great importance to me, and they are the people I look up to more than anyone else in the world. Thank you both so much.

Koen Prud'homme van Reine
Delft, August 2025

[1] Anything that can go wrong, will go wrong

Summary

The first aircraft were powered by propellers, but turbofans have become the more prevalent propulsion method since then. The higher theoretical efficiencies of propellers make them an attractive option as the aviation industry needs to improve its fuel efficiency. One of the possible downsides of propellers is the aeroacoustic noise they produce, as there is no shroud to dampen the noise. This noise can be computed if the aerodynamic forces on the blade are known, which explains why accurate models for this are needed. In this thesis, the effects of sweep on the aerodynamic performance are investigated in both an experimental and computational context, and the applicability of the lifting-line method on swept propellers is evaluated.

For this wind tunnel experiment, a new set of blades has been designed, produced and tested. These blades are called XPROP-Λ, as they are based on the existing XPROP propeller but have a spanwise sweep angle distribution. The experiment was conducted in the Low Speed, Low Turbulence Tunnel at the Delft University of Technology. The experimental data used have been obtained at a freestream Mach number of up to $M = 0.12$.

The experimental results show that the non-optimised sweep distribution of XPROP-Λ does not result in significantly different aerodynamic performance characteristics, at the investigated operating conditions. Some small changes occur, such as a shift in blade loading to the outboard of the blades, and an increase in slipstream width for the swept blade. The slipstream contraction has a magnitude of about 5% of the propeller diameter, and the slipstream contraction of XPROP-Λ is found to be approximately 20% less than that of XPROP.

For the computational work of this thesis, two different lifting-line methods and two sets of 2D airfoil polar reference data have been used. The first lifting-line method is called the lift-based method, also known as the Γ-method. This method iterates the value of lift to obtain a converged solution to the lifting-line problem. The second method, called the flow-tangency-based method, applies a boundary condition that enforces local flow tangency and iterates the angle of attack to incorporate viscous effects. This method is sometimes referred to as the α-method. The first set of airfoil data, based on the NACA 4-series, is obtained at the right Reynolds numbers, but has different airfoil shapes than the propellers used. These polars were calculated using XFOIL, a 2D panel method which can compute some viscous effects. The polars also showed non-physical behaviour at the lowest Reynolds numbers investigated, further reducing their reliability. The second set of airfoil polars was computed with the exact airfoils in the examined blades and based on RANS simulations, but at Reynolds numbers which are about 30 times those seen in the wind tunnel. Thus, this source of airfoil data is also unreliable.

The main conclusion of this work is that none of the combinations of the lifting-line method and 2D airfoil polar data is definitely the best at replicating the results of the wind tunnel experiment. The flow-tangency-based method generally is better at predicting the effect of adding blade sweep, whereas the lift-based method is better at replicating the performance parameters measured in the wind tunnel.

When analysing the effect of the added blade sweep of XPROP-Λ on the lifting-line simulations in terms of the integrated performance, and comparing it with the experimental results, it is found that this effect is generally overestimated by the lifting-line methods. The lifting-line methods generally predict a larger change due to sweep in the thrust and power coefficients than in the propulsor efficiency. The lifting-line methods also fail to accurately estimate the change of the spanwise loading distribution, with the lift-based method overestimating this change and the flow-tangency-based method underestimating it.

Overall, this thesis project has provided the Delft University of Technology with new datasets on swept propellers and, most importantly, a new propeller geometry that can be used for future wind tunnel testing and model validation. It has been shown that the lifting-line tools need further work before they are accurate at the operating conditions seen in the wind tunnel. One of the main recommendations of this thesis is to change the airfoil data used to better estimate the viscous and compressibility effects.

Contents

Nomenclature

Abbreviations

Abbreviation	Definition
ADT	Actuator Disk Theory
BEM	Blade Element Momentum
CAD	Computer-Aided Design
CNC	Computer Numerical Control
CPR	Counts Per Minute
LLM	Lifting-Line Method
LTT	Low Turbulence Tunnel
RPM	Rotations per Minute
RPS	Rotations per Second
RSB	Rotating Shaft Balance
TE	Trailing Edge
VLM	Vortex Lattice Method

Symbols

Symbol	Definition	SI-Unit
c	Chord	[m]
C_d	Drag coefficient	[-]
C_l	Lift coefficient	[-]
C_P	Power coefficient	[-]
C_{P_t}	Total pressure coefficient	[-]
C_Q	Torque coefficient	[-]
C_T	Thrust coefficient	[-]
D	Propeller diameter	[m]
E_k	Kinetic energy	[kg m^2 s^{-2}]
J	Advance ratio	[-]
M	Mach number	[-]
$\dot{m}$	Mass flow rate	[kg s^{-1}]
n	Rotational velocity	[s^{-1}]
p	Momentum	[kg m s^{-1}]
P	Power	[kg m^2 s^{-3}]
Q	Torque	[kg m^2 s^{-2}]
r	Local propeller radius	[m]
R	Total propeller radius	[m]
Re	Reynolds number	[-]
T	Thrust	[kg m s^{-2}]
T_c	Thrust coefficient	[-]
V	Velocity	[m s^{-1}]
V_∞	Freestream velocity	[m s^{-1}]
u	Propeller induced axial component of velocity	[m s^{-1}]
U	Axial component of velocity	[m s^{-1}]
x	Axial position in the wind tunnel	[m]
y	Spanwise position in the wind tunnel	[m]

Symbol	Definition	SI-Unit
z	Vertical position in the wind tunnel	[m]
α	Angle of attack	[rad]
β	Pitch angle	[rad]
Γ	Circulation	[m^2 s^{-1}]
ε_{sb}	Solid blockage coefficient	[-]
ε_{ss}	Slipstream blockage coefficient	[-]
η	Efficiency	[-]
ρ	Density	[kg m^{-3}]
ϕ	Inflow angle	[rad]
Ω	Angular velocity	[rad s^{-1}]

Part I

Background

1

Introduction

Propellers have been around for over a century, as they were the original mode of powering aircraft. Since then, turbofans and jets have taken over as the primary propulsion method, but over the last years, a renewed interest in propellers has resurfaced. The primary driver behind this renewed interest is the propulsive efficiency that propellers can achieve, which is higher than turbofan engines [1, 2].

One of the downsides of propellers is the aerodynamic noise they produce whilst in operation. Modern research focuses on various ways to reduce this noise. Adding sweep to the propeller blade is one of the ways to do so [3]. Sweeping the blade causes phase lag to the acoustic signals that are emitted by different parts of the blades, thus lowering the overall noise level [4].

The TU Delft has done research into this domain using computational methods, and has also combined low-level aerodynamic tools with acoustical and structural tools [3, 5, 6]. To accurately predict the noise emissions of a propeller blade, an accurate blade loading must be computed. It is currently unclear what level of aerodynamic modelling fidelity is required to capture the effect of blade sweep on the loading accurately. Highly detailed aerodynamic calculations are computationally expensive and too time-consuming to be convenient when trying multiple propeller designs. The simplest models are not refined enough to include the effect of blade sweep, and thus, a middle ground needs to be found. The lifting-line model is one such low-level model, which has been worked on extensively within the Delft University of Technology over the past years [7].

The objective of this thesis is to expand upon this work by investigating the accuracy of the lifting-line method by comparing computational results with a wind tunnel experiment. This wind tunnel test was conducted at low Mach numbers, with the maximum evaluated freestream Mach number being 0.12. The tip Mach number did not exceed 0.5. The diameter of the propeller blade is 0.4064 metres. The experiment was conducted at lower Reynolds and Mach number conditions than those seen on real propellers, and thus, these results cannot directly be applied to real-world conditions.

In this test, the aerodynamic performance and flowfield of a swept blade will be compared with those of a similar, but unswept, propeller. The aim is to investigate if the lifting-line tools currently available can accurately determine the effect of sweep on propellers, both for overall performance characteristics as well as local loading effects. This is relevant, among other things, for noise analysis.

This thesis is centred around the following question: ”What are the effects of sweep on the aerodynamic performance of propellers, and is the lifting-line method an appropriate tool for computing these effects?” This is a broad question, which will be split up into the following sub-questions:

- What is the difference between XPROP and XPROP-Λ in terms of aerodynamic performance, based on the wind tunnel experiment?
- What is the effect of the sweep of XPROP-Λ on the flowfield around the propeller, in the wind tunnel?

- Is the lifting-line methodology used an accurate predictor of the aerodynamic performance parameters measured?
- Do the lifting-line methods investigated accurately predict the effect of blade sweep on the aerodynamics of the propellers, as seen in the experimental data?

The lifting-line tool used in this thesis is based on the work by Dr. G. Margalida [7, 8]. The hypothesis to the main research question is that this lifting-line method is an appropriate and accurate tool for determining the propeller performance of both swept and unswept blades.

This thesis has the following structure: Chapter 2 provides background information required for comprehending the remainder of the thesis, based on pre-existing literature. Chapters 3 to 5 make up the methodology section of this work, expanding on the propeller geometries examined, as well as the experimental and computational techniques used. The results are presented in chapters 6 and 7, with the conclusions in chapter 8 and recommendations for future works in chapter 9.

2

Literature Review & Background

This chapter provides the necessary background information for the remainder of this thesis. A theoretical explanation of the potential efficiency benefit of propellers is provided, followed by information about the fundamentals of propeller aerodynamics. This is followed by a note on acoustics, as this is one of the main motivators behind the inclusion of sweep into propellers. Afterwards, the effect of sweep on aerodynamic performance is discussed. The chapter concludes with background information and a motivation for the use of computational and experimental methods.

2.1. The Potential Efficiency Benefit of Propellers

With any propeller, the thrust produced can be defined as the rate of change in momentum over time. If it is assumed that the propulsor does not add any mass to the flow, and thus that the mass flow stays constant, this change in momentum can be written as follows:

$$T = \frac{\mathrm{d}p}{\mathrm{d}t} = \dot{m}\left(V_{\mathsf{out}} - V_{\mathsf{in}}\right) \tag{2.1}$$

Thus, to increase the thrust of a general propulsor, one can either increase the velocity differential between the in- and outflow or one can increase the mass flow. A second important performance parameter is the propulsive efficiency. This is the ratio between the propulsive power or the rate of useful work, and the power that is added to the flow. This can be expressed as follows:

$$\eta = \frac{P_{\mathsf{out}}}{P_{\mathsf{add}}} = \frac{TV_\infty}{\Delta \dot{E_{kin}}} = \frac{2}{1 + \frac{V_{\mathsf{out}}}{V_\infty}} \tag{2.2}$$

Therefore, to achieve a high propulsive efficiency, a small velocity increment is key. Thus, it can be concluded that to have an efficient propulsor with high thrust, it should be a system that has a large mass flow and a low velocity differential. Increasing the mass flow can be done by increasing the overall size of the propulsor. However, increasing the size of a ducted propulsor, such as a turbofan, increases the drag of the shroud as well, effectively limiting the size and therefore efficiency of the propulsor [9, 10]. Additionally, the weight of the shroud also increases when increasing the size of a turbofan engine, further reducing the overall efficiency of the aircraft utilising the propulsor. Propellers are not limited by these factors and can therefore reach higher theoretical propulsive efficiencies.

It is important to note that the propulsive efficiency is not the only definition of efficiency. Another efficiency to evaluate is the propulsor/fan efficiency, which is described in equation (2.11). Propulsive efficiency only accounts for the losses due to axial acceleration behind the propeller, but not the rotor losses, such as swirl and blade drag [11].

2.2. Propeller Aerodynamics Fundamentals

Figure 2.1 shows the velocity diagram of the cross-section of a propeller blade. One can see that this is not dissimilar to that of a conventional aircraft wing. A wing-like element generates a single resultant

force, which for wings is often separated into the lift and drag components. For propellers, it is conventional to separate said force into thrust and torque instead. The decomposition of the aerodynamic force on a 2D slice of a propeller into lift and drag, as well as thrust and torque, is shown in figure 2.1. Figure 2.1 shows that the torque produced by the propellers acts in the opposite direction to the blade rotation. Thus, this torque needs to be overcome by the engine.

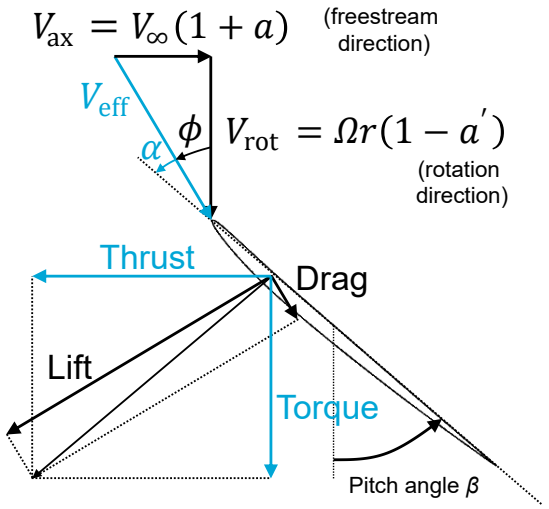

Figure 2.1: Propeller velocity diagram, adapted from Sinnige [11].

It is important to note that the axial and rotational velocities experienced by 2D slices of the blade are not purely related to the freestream and angular velocities of the blade, but that both are impacted by velocities induced by the propeller itself. These induced velocities are represented in figure 2.1 by the local induction factors a and a'. There is also no loading generated right at the propeller tips. Finally, the flow does not move in isolated radial positions, but has a radial component as well, which changes the performance due to a change in airfoil shapes interacted with by the flow.

When defining aerodynamic performance, it is customary to use non-dimensional quantities, which allows for scalability. Thus, the major performance quantities, i.e. the thrust and power, need to be put in coefficient form. The equations for these coefficients are given below, starting with the thrust coefficient (C_T):

$$C_T = \frac{T}{\rho n^2 D^4} \tag{2.3}$$

Another way of non-dimensionalising the thrust of a propeller is per the following equation:

$$T_C = \frac{T}{\rho V_\infty^2 D^2} \tag{2.4}$$

The difference between the two coefficients is that T_C is normalised using the freestream velocity, whereas C_T uses the propeller rotational velocity. Thus, two propellers of equal blade span, operating at the same thrust at the same freestream conditions, will have the same T_C, but not necessarily the same C_T. The relation between the two power coefficients is the following:

$$T_C = C_T \cdot J^2 \tag{2.5}$$

The power required to drive the propeller is represented by the power coefficient (C_P):

$$C_P = \frac{P}{\rho n^3 D^5} \tag{2.6}$$

As previously alluded to, there is a direct relation between the blade torque and the required shaft power.

$$P = \Omega Q = 2\pi n Q \tag{2.7}$$

Torque can also be non-dimensionalised, using the following equation:

$$C_Q = \frac{Q}{\rho n^2 D^5} \tag{2.8}$$

Or alternatively,

$$C_Q = \frac{C_P}{2\pi} \tag{2.9}$$

Therefore, it is shown that it is not needed to discuss both the power and torque coefficients, as the only difference between them is multiplication by a constant. To follow standard conventions, it is chosen to focus on the power coefficient C_P in this thesis.

Another key parameter for the performance of propellers is the advance ratio, J. It describes the ratio between the forward distance travelled in a single revolution of the propeller and the propeller diameter. It is equal to the freestream velocity divided by the blade tip speed, as shown in equation (2.10).

$$J = \frac{V_\infty}{nD} \tag{2.10}$$

In this equation, V_∞ is the freestream velocity, n is the rotational velocity in rotations per second, and D is the diameter of the propeller.

The propulsor efficiency of a propeller can be written as a function of the advance ratio, thrust and power coefficients:

$$\eta = J\frac{C_T}{C_P} \tag{2.11}$$

To understand a propeller, it is important to not only look at the propeller, but also at the flow surrounding it. A low-level method for obtaining information about the slipstream/streamtube of a propeller is by modelling it as an exchanger of momentum with the flow. This technique is called the actuator disk theory (ADT) or classical momentum theory, and it is a 1D model. The assumptions underlying this method are incompressible, inviscid, steady flow with no rotation (swirl) in the flow and constant disk loading. The flow velocity is assumed to be constant in the radial direction. A drawing of a streamtube with accompanying pressure and velocity distributions is shown in figure 2.2.

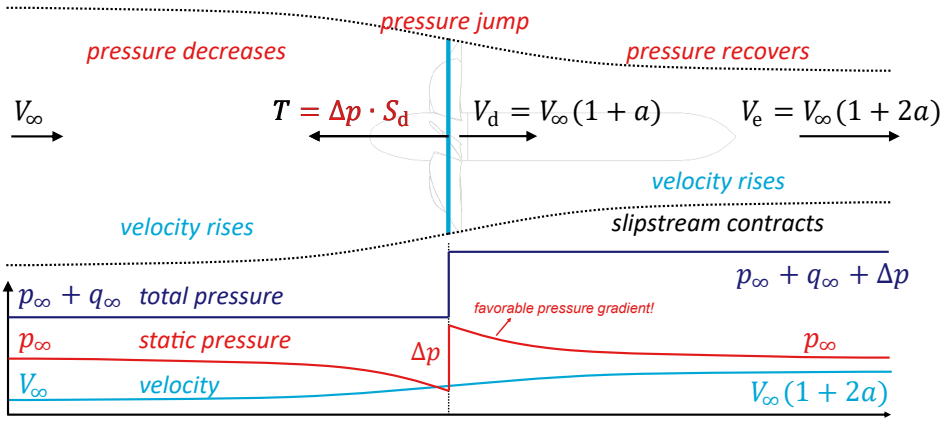

Figure 2.2: Propeller streamtube with distribution of pressures and velocity, from Sinnige [11].

Bernoulli's equation can be used to compute the pressures and velocities. A fundamental assumption is that the flow is at freestream static pressure infinitely far upstream and downstream of the actuator disk. As the propeller adds momentum to the flow, this must therefore come from an instantaneous pressure jump at the actuator disk. To satisfy the constant mass flow within the streamtube, it can be seen that the cross-sectional area of the streamtube reduces as the flow velocity increases. An important observation from figure 2.2 is that the highest velocities in a propeller streamtube do not occur right at or close behind the propeller, but further downstream when the full slipstream contraction has taken place.

2.3. Propeller Aeroacoustics

The potential noise reductions achieved by adding blade sweep are one of the motivators for the modern interest in swept propellers. This section provides background information on the aeroacoustic noise generated by propellers. Propeller noise can be separated into two parts: broadband noise and tonal noise.

Broadband noise is random and stems from turbulent flows on the propeller blades [12]. In the case of turbulent inflow, some broadband noise is generated by the flow at the leading edge. The boundary layer will be turbulent in most cases once the flow reaches the trailing edge, regardless of inflow conditions. This turbulent flow at the trailing edge is the second source of broadband noise. It has been found that for full-scale propellers, broadband noise is relatively unimportant for the overall noise of the propeller [12]. Thus, broadband noise will not be considered in the remainder of this thesis.

Tonal noise refers to the part of propeller noise that is periodic. This noise is generated by the spinning of the propeller at a constant frequency. Tonal noise can be separated into steady and instead components [12]:

- Steady sources include thickness noise and steady-loading noise. Thickness noise stems from the displacement caused by the volume inhabited by the propeller geometry. It depends on the blade volume, shape of the blade cross-section and rotational speed. Loading noise comes from the pressure disturbances caused by the aerodynamic loads of the propeller blades.
- Unsteady noise sources include unsteady-loading noise. An example of this would be if the propeller is operated at an angle of attack with respect to the inflow. This angle would result in a non-constant loading on the propeller, varying periodically as the blade rotates, resulting in tonal noise. Unsteady-loading noise can either add to or subtract from the steady-loading noise. Transonic flow, which primarily occurs near the tips of high-speed propellers, will also result in unsteady noise due to the shock waves.

Various blade design parameters influence the noise level of a propeller: Hubbard [12] mentions blade sweep, thickness, count and shape, as well as propeller diameter and the airfoil profiles used. The next part will elaborate on the effect of sweep on propeller noise.

Applying sweep to a propeller blade has two distinct benefits [13]:

- The Mach number effects are reduced, similarly to the effect of sweep on conventional wings. Noise from transonic flow is reduced.
- The noise signals originating from different spanwise locations are ”dephased”. This dephasing behaviour leads to interference, as shown in figure 2.3.

Thielen [5] and van Dijk [3] both show that applying sweep can result in significant far-field noise reductions. Both works modify the original XPROP design [14], operating at $M_\infty < 0.2$. Thielen showed that sweep not only impacts noise but also the elastic behaviour of a propeller, resulting in a noise reduction of 2.5 dB. Van Dijk found a 12.4 dB reduction in Effective Perceived Noise Level (EPNL) for a 1% power penalty. The EPNL is a metric for aircraft noise, based on noise frequency, duration and human sensitivity to the noise.

2.4. The Effect of Sweep on Propeller Aerodynamics

The first introduction of sweep to conventional aircraft wings was in 1935 [15], to reduce the drag of wings operating at transonic conditions. Sweep reduces the velocity of the flow normal to the leading edge and therefore the effective Mach number, leading to a reduction in compressibility effects and drag. Less than two decades later, swept propellers were investigated for the same reason.

One of these early works is by Evans et al. [16], in which a swept and two unswept blades were compared in an experiment, with freestream Mach numbers up to 0.65 and tip Mach numbers up to 1.15. They concluded that the swept propeller did not have an increased efficiency for these operating conditions. However, the tip Mach number at which negative effects of compressibility were witnessed was 6% higher for the swept blade than the unswept blade, which is significantly less than the 30%

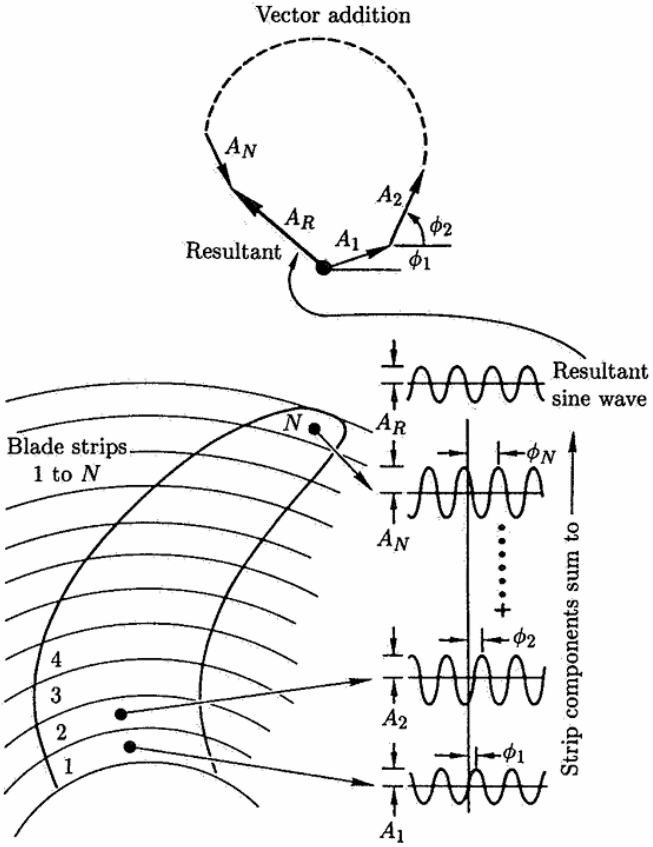

Figure 2.3: The concept of the benefit of sweep: Indication of phase lag and interference spanwise, from Hanson [13].

increase in tip Mach number that was predicted. Additionally, an inboard shift in the spanwise loading distribution was witnessed.

Computational investigations using a vortex lattice method were conducted by Sullivan [17]. He concluded that whilst C_P is reduced by the application of blade sweep, efficiency stays about constant or even marginally increased. The power loading was reduced locally where the sweep was introduced. The planforms investigated by Sullivan [17] can be seen in figure 2.4

Interestingly, Melpignano [18] noticed an outboard shift of the loading distribution when adding sweep to a propeller blade, the opposite result of Evans et al. [16]. Melpignano [18] uses a freestream Mach number less than 0.12, significantly less than Evans et al. [16].

Burger [6] also investigated the effect of sweep, and did a direct comparison with XPROP (for more about XPROP, see chapter 3). He found that sweep can have a substantial effect on both noise and efficiency, as shown in figure 2.5. Similar results were obtained by Thielen [5] at comparable operating conditions, who also highlighted that sweep can result in an outboard shift in the spanwise loading distribution, and that it often increases the local angle of attack. This was also witnessed by van Dijk [3].

Overall, it can be concluded that sweep may have a substantial effect on the performance of a propeller, but it is not possible to make a blanket statement about what these effects will be, as this is strongly dependent on the specifics of the propeller blade investigated. Studies at operating conditions similar to those used in this thesis tend to predict an outboard shift in the spanwise loading distribution.

2.5. Computational Methods for Propellers

When working with propellers, it is crucial to obtain as much information about them as possible before producing a working prototype. Computations allow for comparing and optimising designs without incurring the costs of producing multiple working prototypes. There are many different ways to try and

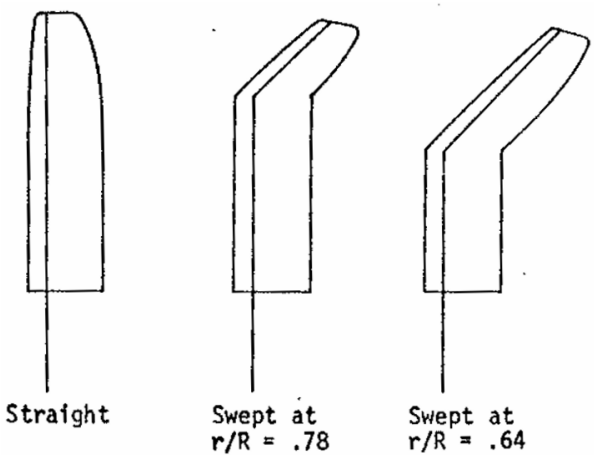

Figure 2.4: Sweep planforms investigated by Sullivan [17].

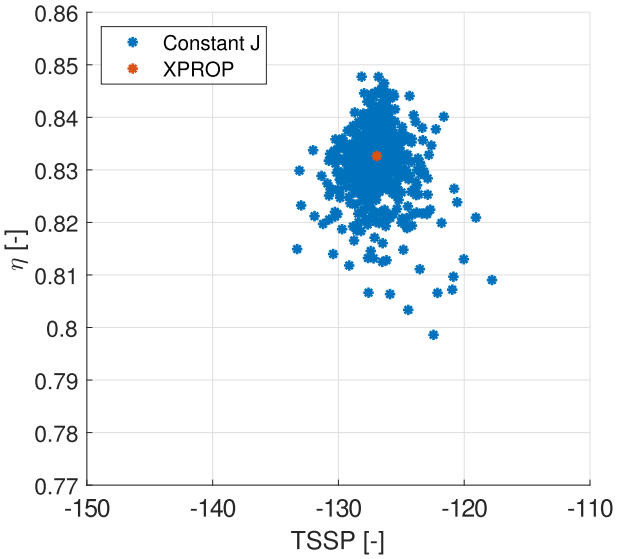

Figure 2.5: Possible effects of sweep on noise and efficiency, by Burger [6].

model the way a propeller works, the most important of which are discussed in this section.

The actuator disk theory (ADT) model is one such model, based on the streamtube shown in figure 2.2. With this model, a propeller is represented purely by a pressure jump over a surface. However, when a propeller is modelled purely upon the overall pressure jump, no sweep can be applied to said model, as geometric details are not taken into account. This makes the actuator disk an insufficient modelling tool on its own for this thesis. However, it is still a useful tool for developing preliminary propeller characteristics, which can act as initial conditions for other modelling techniques, or when explaining propeller aerodynamics for the first time.

On the other end of the spectrum, one could use a full CFD solver for the Navier-Stokes equations, as done by van Arnhem [19] and Stokkermans [20]. Doing full simulations in this way is too time-consuming for general design and optimisation methods. Thus, alternative ways of determining the aerodynamic characteristics of propeller blades need to be used.

There are three well-known low-fidelity aerodynamic modelling techniques for computing propeller performance, which take into account the propeller blade geometry and are therefore theoretically suited for incorporating propeller blade sweep, among other factors: The blade element momentum (BEM) technique, the vortex lattice method (VLM), and the lifting-line method (LLM). Of these methods, the

lifting-line method has seen a lot of work at the Delft University of Technology recently [7]. It was therefore chosen to use the wind tunnel test as a chance to validate this model and investigate its effectiveness.

2.6. Experimental Background

It is crucial to be aware of the limitations of any simulation method, whether it is computational or experimental. Computational methods are more convenient to execute, as the geometry and operating conditions can be changed quickly. However, most computational methods are based on assumptions to simplify the physics to allow for rapid computations. These assumptions often have a small impact, but without experimental data, it is impossible to accurately quantify their effect. Within an experimental environment, no assumptions about the quality of the flow are made, as one is dealing with real flows. Therefore, experimental simulations are an integral part of modern research, even with the current advances in computing power and computational methods.

Comparisons between computational and experimental results are a common practice when validating the computational results. Examples of this can be seen in various master's theses [5, 6, 18], as well as PhD dissertations [19, 20]. These works all use the XPROP propeller [14] as a reference propeller, which has unswept blades. This thesis is the first time that a swept version of XPROP will be used for a comparison between experimental and computational simulations at the Delft University of Technology.

Scale models are often used when simulating propellers in a wind tunnel. This is done because of the size limitations of most wind tunnels, which often are not sized to hold full-size propellers. Secondly, the freestream velocities are often lower than those seen on real aircraft, both due to the limitations of the wind tunnel and due to the limitations of evaluated propeller setups. This scaling reduces the Mach and Reynolds numbers that are achieved during testing, and makes it challenging to extrapolate results from wind tunnel testing to freestream conditions. In general, the rule is that the Reynolds number in the wind tunnel should be above 500,000 to be representative of full-scale performance [21]. During the experiments for this thesis, most Reynolds numbers were between 100,000 and 200,000, and therefore cannot be directly extrapolated. The tip Mach numbers of the investigated propellers were also lower than those seen on aircraft, with the highest tip Mach numbers being 0.5, instead of the transonic Mach numbers seen on aircraft. However, the effect of the blade sweep on the induction along the propeller can still be investigated at the investigated Reynolds and Mach numbers.

One of the main limitations of experimental work in wind tunnels is the effect of the walls of the test section. When using an isolated propeller setup, two of these effects are present, which are the effect of solid blockage as well as slipstream blockage. Solid blockage can be explained as the effect of the volume in the test section, inhabited by the testing geometry. When dealing with a closed-section, such as for this work, this effect stipulates that any geometry in the test-section reduces the overall area of the cross-section, and thus locally accelerates the flow. This can easily be explained by looking at the continuity equation, see equation (2.12).

$$\rho_1 V_1 A_1 = \rho_2 V_2 A_2 \tag{2.12}$$

When assuming incompressible flow, equation (2.12) can be used to show that the flow velocity must increase to account for the reduction in local area. It is important to note that this velocity increase is not equal throughout the cross-section, but is primarily focused near the walls of the section. This can be explained with figure 2.6. It can be seen that the streamlines in figure 2.6a are broadly similar to those in figure 2.6b near the cylinder itself. The main difference occurs near the tunnel walls, where the streamlines are forced to follow the tunnel walls when these are present, but can freely move away from the cylinder in the freestream flow.

From literature, such as Barlow et al. [22], a way of correcting for blockage effects can be found. This method is based on the body shape factor of the geometries present within the test section, as well as their volumes compared to the test section area. The correction factors found for solid blockage are combined with those for other effects (such as slipstream blockage, see next part) to obtain overall correction factors.

The second effect of the wind tunnel walls, slipstream blockage, is similar to solid blockage, but with an opposite effect on the freestream velocity. The test was purely of an isolated propeller without an angle

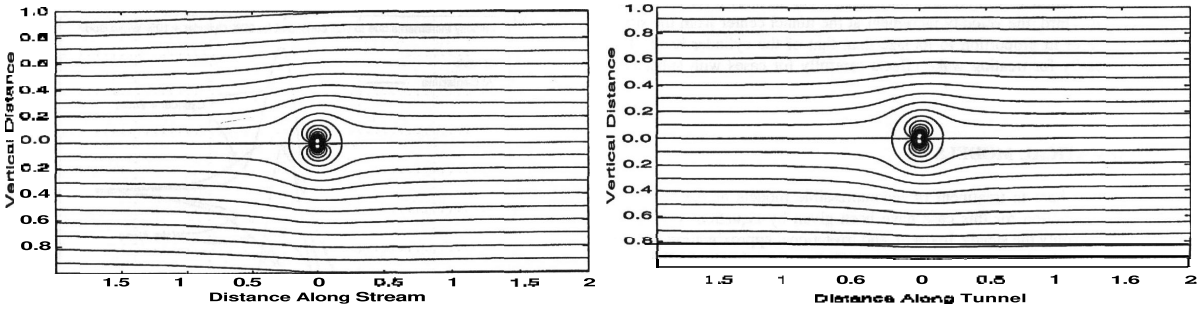

(a) Streamlines around a cylinder in freestream flow.

(b) Streamlines around a cylinder in closed-section wind tunnel flow.

Figure 2.6: Comparison of streamlines around a cylinder for freestream and wind tunnel flows, from Barlow et al. [22, p. 334].

of attack, using a closed test section. Thus, the situation is akin to figure 2.7. The slipstream behind a propeller has an increased velocity compared to the freestream velocity, due to the added momentum in this flow. To maintain continuity in the test section with respect to the flow upstream of the propeller, it can be concluded that the flow outside the slipstream has a reduced velocity.

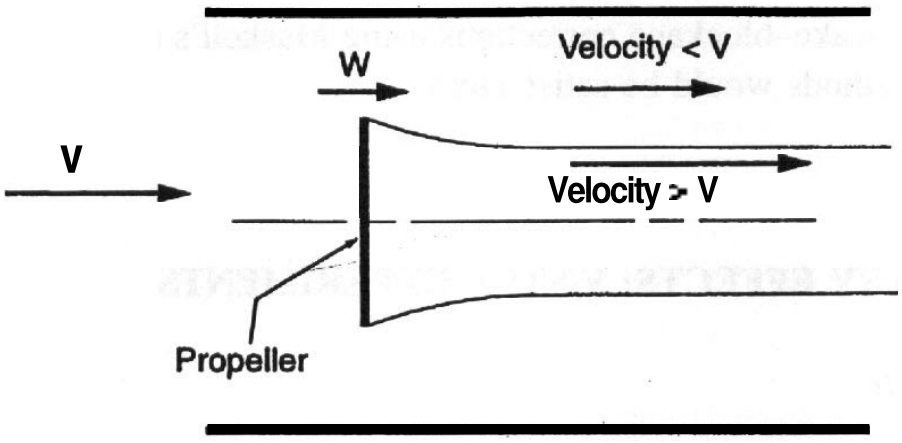

Figure 2.7: Effect of a slipstream on the velocity in a wind tunnel with a closed test-section, from Barlow et al. [22, p. 434].

The flow outside the slipstream, if the propeller were to be operating, should still flow at the freestream velocity V_∞. Thus, this reduced velocity is an effect of the wind tunnel. This reduced velocity causes an increase in the static pressure, which also increases the static pressure in the wake, and therefore causes an increased thrust component [22]. Alternatively, it can be said that the achieved thrust in the wind tunnel would be achieved at a lower speed in a flow without boundaries.

The increase in freestream velocity due to the wind tunnel walls and the increased momentum in the propeller slipstream needs to be accounted for. The correction factor for this can be found by the following equation, which has various formulations (Barlow et al. [22], Eitelberg [23], Sinnige [24]), but comes down to the following:

$$\varepsilon_{\text{ss}} = -\frac{T_c^*}{2\sqrt{1+2T_c^*}}\frac{S_p}{S_{wt}} \tag{2.13}$$

In this equation, the thrust coefficient used is not the one described by C_T, but instead is given by T_c^*, shown in equation (2.14). Please note that $T_C^* \neq T_C$. Additionally, S_P is the area of the propeller, see equation (2.15), and S_{wt} the area of the tunnel cross-section. ε_{ss} is the slipstream blockage coefficient, which, together with the coefficient of solid blockage, will be used to correct the freestream velocity and therefore advance ratio, as shown in equation (4.1).

$$T_c^* = \frac{T}{\rho_\infty V_\infty^2 S_P} \tag{2.14}$$

$$S_P = \frac{\pi}{4} D_P^2 \tag{2.15}$$

The correction factors for the slipstream blockage and solid blockage can be superimposed and used to obtain the value for the equivalent freestream velocity. As the advance ratio J scales directly with V_∞, this means that the boundary corrections can directly be applied to J.

Part II

Methodology

3

Propeller Geometry

To evaluate the effect of sweep on a propeller while keeping all other factors the same, two propellers were used, both during the wind tunnel test and the computational analysis. Geometric details, as well as information about the design and production process, are provided in this chapter.

The XPROP propeller will be used as the reference propeller for the experiment, as this propeller is the reference propeller of the Delft University of Technology [14]. It has been used extensively in both applied and isolated configurations, for example, by van Arnhem et al. [25] and Stokkermans [20]. XPROP is a 6-blade, unswept propeller. Geometric details such as the thickness, chord and pitch distributions as well as the airfoils used, can be found in figure 3.1 and Stokkermans [20].

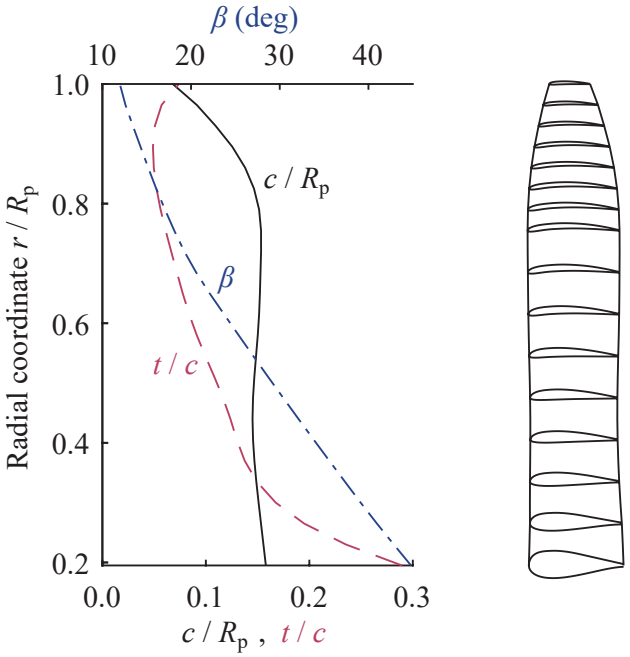

Figure 3.1: XPROP geometry details, from Stokkermans [20].

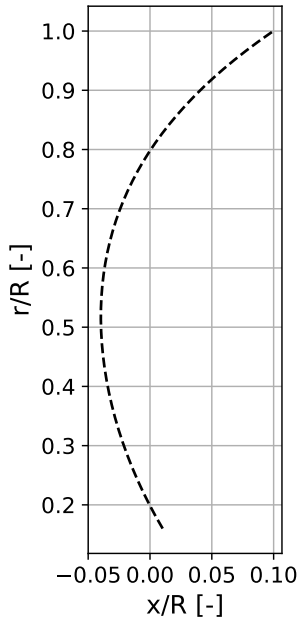

Figure 3.2: Displacements of quarter chord line of XPROP-Λ to incorporate sweep distribution, in normalised coordinates.

The XPROP propeller has no sweep, and therefore, a second blade was required to allow for comparisons. Due to the timeline of the thesis, and the practical constraints of wind tunnel availability, it was decided to not try and design an optimal sweep distribution for XPROP, but to apply a sensible distribution of a pre-existing shape, as was developed by Dr. G. Margalida, using a version of the tools presented in Margalida et al. [7]. This sweep distribution is visualised in figure 3.2. This swept version

of XPROP was afterwards coined XPROP-Λ, which will be used from hereon in this thesis as well. A comparison between the CAD models for XPROP and XPROP-Λ is shown in figure 3.3. Applying the sweep was done by transforming the airfoils in the direction of the tangent of the azimuth. The airfoils move purely within the propeller plane when the blade is placed at zero pitch. This transformation is illustrated in figure 3.4.

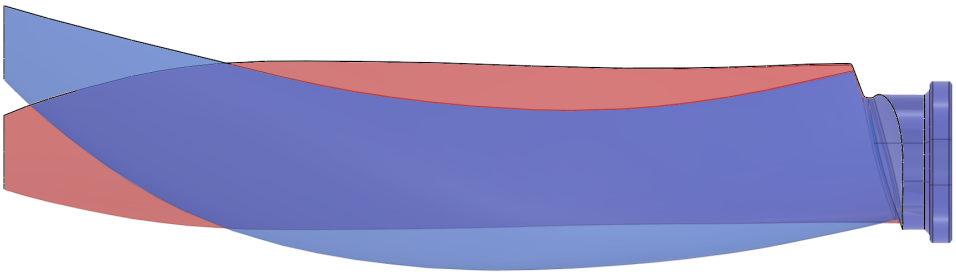

Figure 3.3: CAD comparison between XPROP (red) and XPROP-Λ (blue).

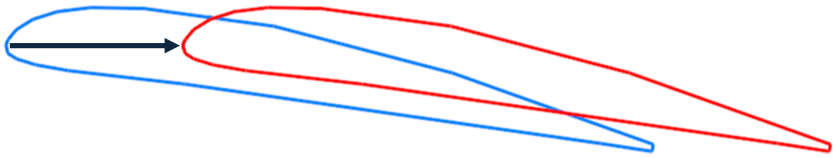

Figure 3.4: Example of transformation applied to add sweep angle from XPROP (red) to XPROP-Λ (blue). The black arrow indicates the transformation direction.

The material chosen for XPROP-Λ was stainless steel[1]. A CAD (computer-aided design) model of XPROP was modified to create XPROP-Λ. A 5-axis CNC (Computer Numerical Control) mill was used to produce XPROP-Λ. The combination of production method and material meant that the thickness of the trailing edge (TE) could not be less than 0.2 mm. The airfoils used for XPROP were not designed to account for this, and therefore, airfoils with short chord lengths had trailing edges that were too thin. This occurred outboard of $r/R = 0.755$. The airfoil adjustments used for the geometry of XPROP-Λ were obtained using XFOIL [26]. The change in trailing edge thickness also requires adjustments in the shape of other parts of the airfoil. The chordwise starting position of these adjustments can be chosen. This distance, called the blending distance, was selected to be at the chordwise position of maximum thickness. An example of the change in airfoil geometry can be found in appendix A. The adjustments in the airfoil geometries were found to have a negligible effect on the airfoil performance, as shown in appendix A. XPROP-Λ was produced sixfold. Finally, the various blades were weighed and modified to balance them along the axis of rotation. Figure 3.5 shows the difference between XPROP and XPROP-Λ in the wind tunnel. General information about both propellers can be found in table 3.1.

Table 3.1: Propeller Specifications

Parameter	Value
Number of blades	6
Propeller diameter	406.4 mm
Spinner diameter	80.4 mm

[1] RVS 430F / AISI 430F / 1.4104 / X14CrMoS17 are various ways the specific alloy used is called.

(a) XPROP **(b)** XPROP-Λ

Figure 3.5: Side-by-side comparison of XPROP and XPROP-Λ in the wind tunnel.

4

Experimental Methodology

The experimental campaign is a major part of the research conducted for this thesis. The test contained two different types of measurements. First of all, there are the performance measurements, which are force and torque measurements used to determine performance characteristics such as the thrust and power coefficient, as well as the propulsor efficiency. Secondly, there are the flowfield measurements, which are used to obtain new information about the aerodynamic effects of the propellers on the airflow behind the propeller. This chapter provides information about the facility used, the test setup, as well as data processing techniques and the experimental procedure used.

4.1. Wind Tunnel Facility

The experiment took place in the Low-speed, Low Turbulence Tunnel (LTT) at the Delft University of Technology. This tunnel is a closed-return, closed test section tunnel. Whilst freestream velocities of 120 m/s can be achieved, this was not the aim of the experiment presented here. The highest velocities achieved during the experiment were close to 60 m/s. The tunnel has a low free-stream turbulence level, between 0.02% and 0.03% for the operating conditions examined for this thesis [27].

The test section is octagonal, and is 1.80 m wide and 1.25 m high, as shown in figure 4.1. The test section has a cross-sectional area of 2.07 m^2. The isolated propeller setup is mounted from the roof of the section and attaches to a 6-component balance. This balance can be used to set the angle of sideslip for the propeller, and was used to set the propeller test setup at zero angle of attack for this experiment. It also functions as a backup for the force measurements done by the rotating shaft balance (RSB). A schematic drawing of the LTT is available in appendix B.

In addition to the propeller, a microphone was positioned in the test section to obtain acoustic measurements. This data was not used for this thesis, but is available for future work. Furthermore, a pitot-static tube was placed near the front of the test section to measure the freestream static and total pressures. The LTT has been used for similar experiments in the past, for example, by Nederlof et al. [28].

4.2. Isolated Propeller Setup

The propeller models for XPROP and XPROP-Λ, as described in chapter 3, were both evaluated as stand-alone models, using the isolated propeller setup. A technical drawing of the setup is shown in figure 4.1. The setup is mounted in the centre of the test-section, with the propeller itself upstream of the attachment sting. This sting has a fairing (a symmetric airfoil) to reduce its aerodynamic effects even further. The fairing is attached to the roof of the test section and is not in direct contact with the sting, and thus prevents the aerodynamic loads on the sting from being included in the external balance measurements. Both the nacelle and the fairing were fitted with carborundum grit to trip the boundary layers and increase consistency between measurements.

The nacelle contains components that are crucial for the operation of the setup. Among these parts are the drivetrain, cooling tubes and an array of sensors. One of these components is the rotating

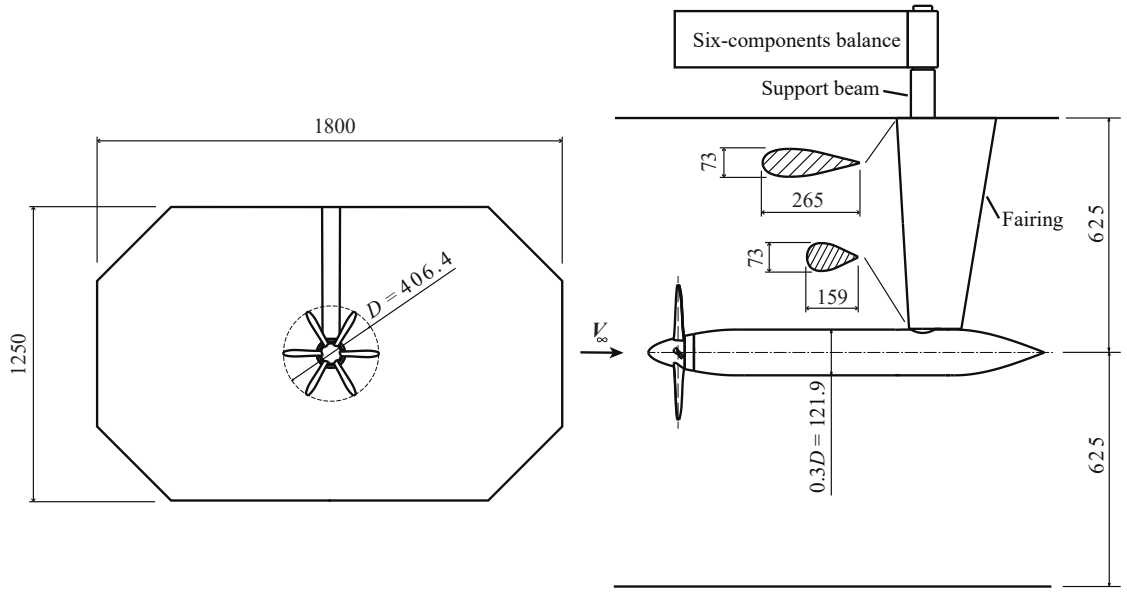

a) Front view **b) Lateral view**

Figure 4.1: Technical drawing of the isolated propeller setup, dimensions in millimetres. Image credit Biagio Della Corte; obtained from Sinnige [29, private communication].

shaft balance (RSB). The RSB is used to measure the forces acting on the propeller and is the primary source of performance measurements used in this thesis. It measures at a frequency of 51.2 kHz, for a duration of 7.1 seconds. The processing of the RSB data is discussed in section 4.4. In addition to the RSB, there is a secondary source of force measurements, which is the six-component external balance, as shown in figure 4.1. The measurements from this balance were used as a backup in case issues arose with the RSB. They have not been used for obtaining any of the results seen in this thesis.

Other parts of the internals are the motor, sensors, and the cooling system. The propeller rotational speed is measured with an optical encoder with 1024 counts per revolution (CPR). The rotational speed is controlled by an external control loop, which takes the reading from the encoder as input. The cooling system consists of an external cooler placed outside of the test section, and cooling tubes running through the internals to cool the motor. All other cables and tubing also go through the sting. A side view of the setup is shown in figure 4.2.

The main challenge when working with this setup is the thermal management, because the internal temperature can increase quickly when operating at high power. The time when operating at peak power should therefore be limited as much as possible to prevent overheating. Unfortunately, the internal temperature sensors were faulty during the entire experimental campaign. Based on previous experiences, it was deemed safe to quickly sample at the most extreme operating condition (J = 0.8 at 40 m/s, i.e. about 7400 rpm), and return to less loaded conditions swiftly to limit the time at max power. Additionally, the flowfield measurement plan was adjusted, which is detailed in section 4.3.

Setting the pitch angle of the individual blades is a manual process, where each blade has to be put in the correct position individually. The pitch angle of the blades is set and measured at $r/R = 0.7$, based on the leading edge position and angle obtained from CAD. The accuracy of setting the pitch angle this way is 0.1°. This effect is described in more detail in section 4.4.2.

The propellers were operated at several different advance ratios, which are detailed in table 4.5. Increasing the advance ratio reduces the thrust setting. It is important to ensure that the highest advance ratios are at positive thrust settings to prevent damage to the setup. The lowest advance ratios were chosen such that peak efficiency was in the range of advance ratios investigated. For 45°, the advance ratios were sampled at intervals of 0.1, whereas for 30°, additional samples were taken at intervals of 0.05 to obtain a higher resolution for the integrated performance measurements, as the overall width of the advance ratio range for this pitch setting was narrower.

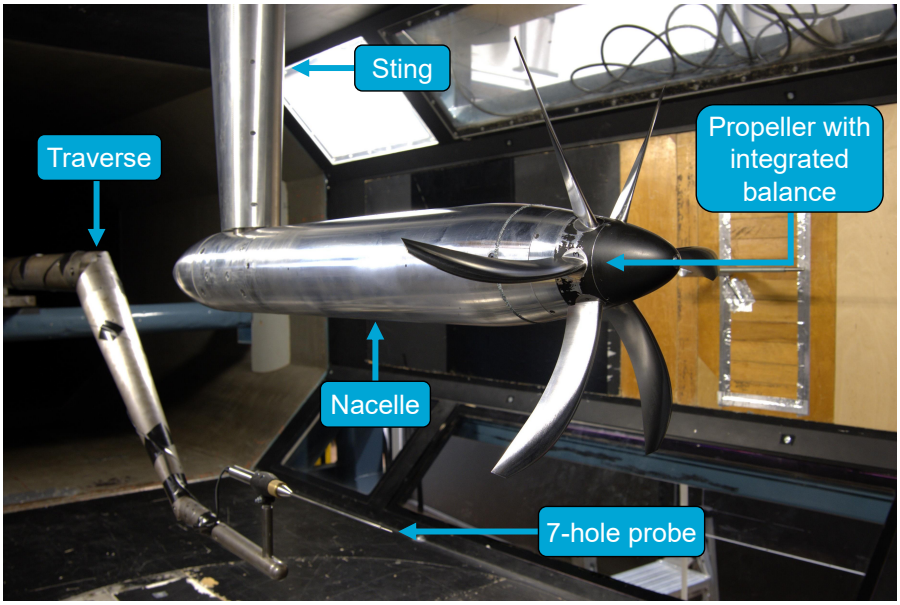

Figure 4.2: Annotated image of the experimental setup with XPROP-Λ mounted. Image credit; Tomas Sinnige

4.3. 7-hole Probe and Traverse System

The experiment aimed not just to obtain information about the aerodynamic performance of the two propellers tested, but also to learn about the flowfield, and most importantly, the slipstream of the propellers. To acquire information about the flowfield behind the propeller, a 7-hole probe was used [30]. A drawing of the probe is shown in figure 4.3. This probe measures pressures at seven locations on the tip of the probe, which are afterwards used to obtain the three components of velocity.

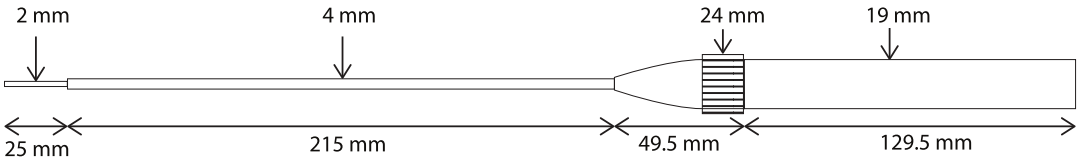

Figure 4.3: Technical drawing of the 7-hole pressure probe, adapted from Duivenvoorden [10].

There are various ways to traverse the probe through the flow in a systematic manner. Both horizontal and vertical patterns have been used during the experiments in the wind tunnel. These patterns are shown in figures 4.4 and 4.5 respectively. The coordinates in figures 4.4 and 4.5 have been normalised with the propeller radius R. In the coordinate system used, $x = 0$ is at the propeller plane of rotation, aligned with the mid chord of the blades. The y and z axes are aligned with the propeller shaft. For this thesis, only the horizontal paths have been further analysed.

Several decisions needed to be made to determine the paths for the 7-hole probe. First of all, the velocity of the probe had to be set. For the experiments, this velocity was set at 7.5 mm/s. Secondly, the sampling frequency of the probe had to be determined and was set to 250 Hz. These values were chosen based on earlier experiments conducted in the same tunnel with the same equipment [10, 31]. After the tests were concluded and a detailed analysis was conducted of the data, it was found that for some of the data, the probe moved at a 50% higher velocity, namely 11.25 mm/s. The difference in probe velocity was corrected for when averaging the measurements onto a fixed grid, which is described in more detail in section 4.5. The velocity of the probe is more than three orders of magnitude lower than the velocity of the flow, and thus it is not necessary to subtract the probe velocity from the flow velocities obtained from the probe measurements.

The setup used for the flowfield measurements, including both the traverse and the specific 7-hole probe, has been used before in the LTT. Examples of this can be found in Duivenvoorden [10] and van Luijk et al. [31]. These also show excellent examples of probe paths.

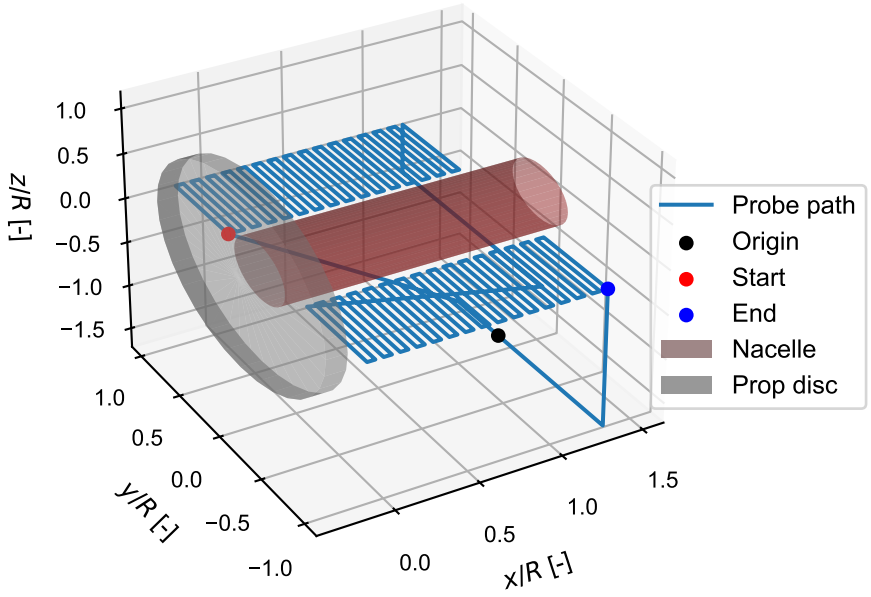

Figure 4.4: Path of the 7-hole probe for horizontal measurements. Dimensions have been normalised by the propeller radius, with the origin at the propeller axis and the mid chord of the propeller blade root.

Both patterns used to take measurements of the flowfield are based on taking measurements in the Y direction, which, in the case of the horizontal measurements, is also the radial direction. An important consideration when determining the path of the probe is the distance between these lines. Putting the lines closer together results in higher data resolution. Lowering the traverse velocity will increase the measurement accuracy, as the number of samples for each grid point after processing increases. The processing method is described in section 4.5. Both of these adjustments will result in a longer overall testing time. To account for this, it was chosen to space the lines about 10 mm apart, as this was the maximum distance between lines that would still provide results of sufficient resolution[1].

Selecting the other parameters of the flowfield planes to measure was more straightforward, as this was mostly constrained by the measurement equipment. For the horizontal sheets, it was chosen to start the measurements as close as possible to the blades, which was 32.5 mm behind the unswept mid chord of the propeller. The mid chord is also the axis around which the propeller is rotated to adjust the blade pitch. The wake sheet had a length of 287 mm, limited by the traverse movement. The innermost measurement point was chosen to be at y = 94 mm, which is 33 mm from the nacelle. Any closer would result in clashes between the traverse and the nacelle. As the outboard limit, it was chosen to go 25 mm beyond the width of the propeller, to ensure that the full extent of the tip vortex was measured. Overall, this resulted in a path that took 24 minutes to complete. For the vertical measurements, it was chosen to measure the maximum extent of the vertical range, limited by the traverse. This resulted in measuring from 212.25 mm below the propeller plane up to 12.75 mm above it. Taking these measurements took 20 minutes.

It was not possible to take probe measurements at a wide range of propeller configurations and operating conditions, due to time limitations. During the experiment, initially, some performance measurements were taken. From these initial measurements, estimations were made of the advance ratio at which the propeller was operating at peak efficiency. It was chosen to take the flowfield measurements at these operating conditions, which can be found in table 4.1.

Thermal management played an important part in determining the probe paths, as alluded to in section 4.2. The loading at the 30° case resulted in concerns regarding overheating when left to run for a prolonged period. It was therefore chosen to separate the measurements into separate sheets, where

[1] Based on discussions with supervisor

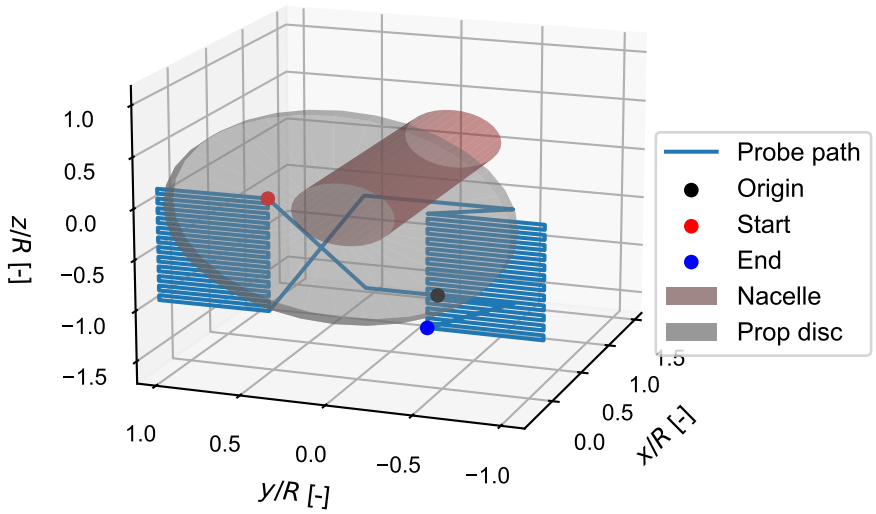

Figure 4.5: Path of the 7-hole probe for vertical measurements. Dimensions have been normalised by the propeller radius, with the origin at the propeller axis and the mid chord of the propeller blade root.

Table 4.1: Operating conditions for flowfield measurements.

Pitch [°]	J [-]
30	1.05
45	1.8

the tunnel was shut down between taking the measurements on the left- and right-hand sides. This resulted in halving the time that the tunnel had to run continuously, at the expense of an increase in total wind tunnel occupation time.

During the setup of the traverse system, it was observed that the probe would move in the vertical (Z) direction when traversing either in the streamwise or radial direction. There was no time available to re-install the traverse system, and thus it was chosen to apply corrections to account for the observed movements. To apply these corrections, measurements were taken of the out-of-plane displacements at the extremes of the movement range of the traverse system, and a linear fit of these measured displacements was used to correct the traverse inputs. The out-of-plane displacements were all less than 1% of the in-plane movements.

4.4. Performance Processing

The data recorded by the RSB needs to be processed to obtain performance parameters, such as the thrust coefficient C_T, power coefficient C_P and the propulsor efficiency η (as defined in equation (2.11)). To do this, boundary corrections need to be applied, and afterwards the individual datapoints are used to obtain curves for the performance characteristics of the propellers.

4.4.1. Boundary Corrections

Two types of boundary correction need to be applied to correct for the effect of the walls of the wind tunnel test section on the freestream flow velocity. These are the solid and slipstream blockage effects. Two solid blockage coefficients are used, one for the nacelle and one for the fairing of the sting. These coefficients are constant and are shown in table 4.2. The values used are based on previously conducted similar experiments. For future work, it is suggested to re-evaluate these values. The solid blockage coefficients are combined to obtain the overall solid blockage coefficient ε_{sb}.

Table 4.2: Solid blockage correction coefficients for nacelle and sting support fairing.

Coefficient	Value
$\varepsilon_{\text{sb, nacelle}}$	0.0018
$\varepsilon_{\text{sb, sting}}$	0.0014
ε_{sb}	0.0032

The slipstream blockage coefficient ε_{ss} is not a constant value, but depends on the thrust coefficient T_C^*, which is shown in equation (2.13). Thus, the correction coefficient has to be computed at each measured point. The range of values for the slipstream correction is presented in table 4.3.

Table 4.3: Extreme values of the slipstream blockage coefficients within the operating conditions evaluated during the experiment.

Pitch angle	Min ε_{ss}	Max ε_{ss}
$\beta = 30°$	-0.0120	-0.0013
$\beta = 45°$	-0.0059	-0.0001

As can be seen in table 4.3, the sign of ε_{ss} is opposite that of ε_{sb}. When comparing the range of values for the slipstream blockage coefficient, it can be seen that they can be smaller or larger than the solid blockage coefficient. This shows that the boundary corrections can result in either an increase or a decrease in the freestream velocity.

When applying correction factors, it is important to keep in mind that only the parameters that take freestream velocity as an input are altered. Hence, the thrust coefficient C_T and power coefficient C_P do not change, but the advance ratio J does. To apply the correction to J, the equation (4.1) is used:

$$J_{\text{cor}} = J_{\text{uncor}}(1 + \varepsilon) \tag{4.1}$$

$$\varepsilon = \varepsilon_{\text{sb}} + \varepsilon_{\text{ss}} \tag{4.2}$$

Where ε is the combined correction coefficient, obtained by adding the slipstream blockage and solid blockage coefficients, as shown in equation (4.2). It was found that the changes in the advance ratio due to the boundary corrections are less than 1%. Further details can be found in appendix C.

During the experiment, freestream flow conditions and advance ratios were set based on uncorrected parameters. The corrections described above were applied after the experiment was concluded, during the processing of the experimental data.

4.4.2. Performance Measurement Data Processing

The individual data points are measured over a set timespan of 7.1 seconds. Each measurement needs to be processed by averaging the loads over the sampling time, obtaining a set of averaged values. Due to the nature of the sampling, these points are concentrated at the chosen advance ratios investigated, which have been highlighted in table 4.5. The data points were then corrected based on the wind tunnel wall corrections as described in the section above. Subsequently, a response model is derived from a linear regression through the corrected data points. For this, a 3$^{\text{rd}}$-degree polynomial is used. Additional terms did not have a significant impact on the quality of the fit. The polynomial fit was afterwards used to obtain the upper and lower bounds of the 95% confidence interval, which allows for comparison between different datasets to see if any observed offsets are statistically significant. It is important to note that the interpolations done are only valid for the range of advance ratios investigated and should not be used for extrapolations. An example of the fitted performance curves can be found in figure 4.6, which shows good agreement between the data points and the resulting curves. For the remainder of this thesis, no individual data points are shown to make the graphs more easily readable.

The setting of the pitch angle for the propeller is a manual process, in which human error can cause inaccuracies. To investigate the effect of this, the XPROP blade has been measured at 44.9° and 45.0° of pitch. The resulting graphs, including the 95% confidence intervals and the difference between the two pitch settings, are shown in figure 4.7.

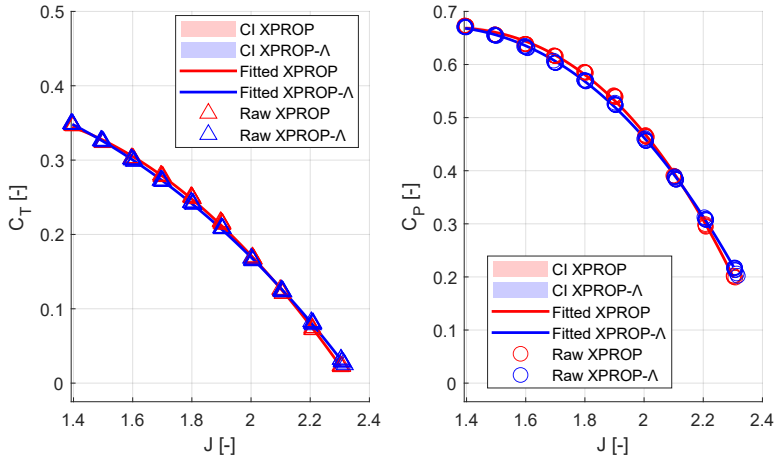

Figure 4.6: Result of fitting the regression model through the measured data points. $\beta = 45°$.

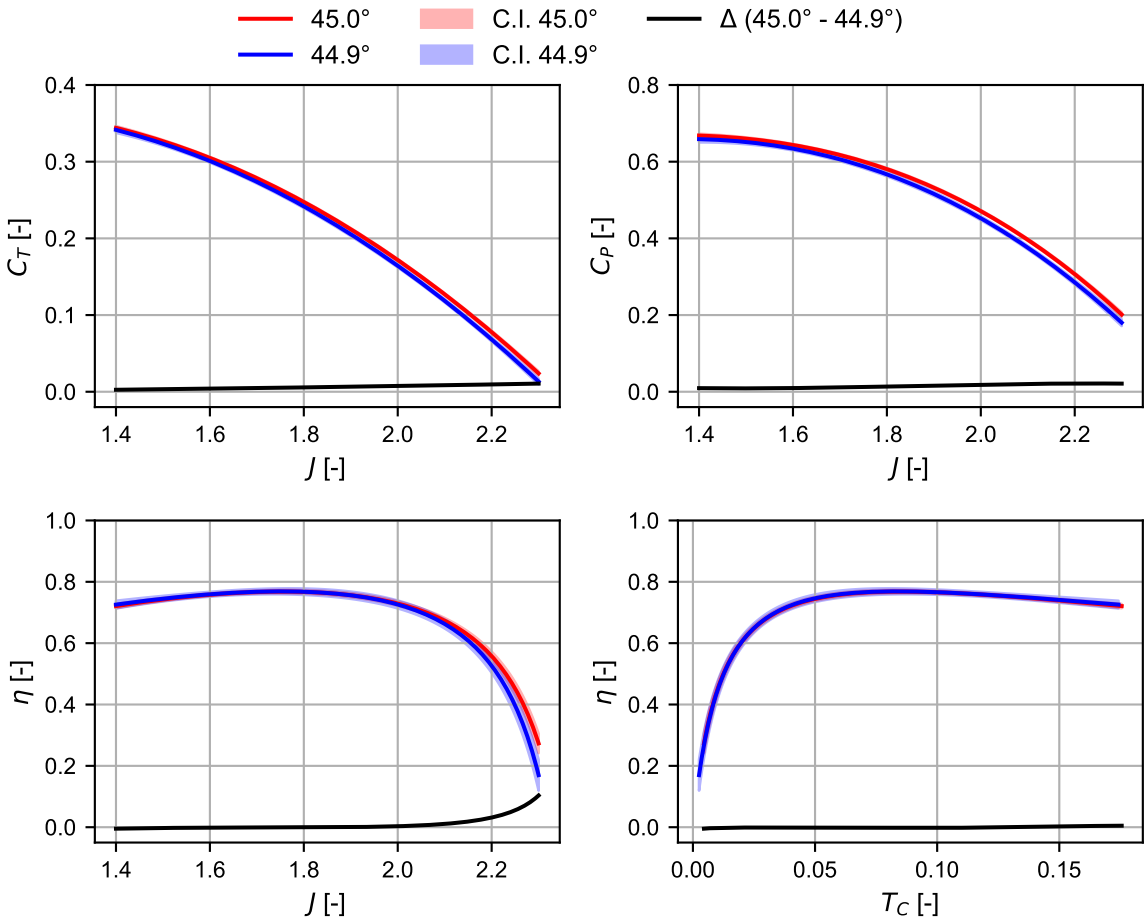

Figure 4.7: Comparison between 44.9° and 45.0° pitch on XPROP. Includes the 95% confidence intervals and the difference between the two pitch settings.

From figure 4.7, it can be seen that a small offset in set pitch angle has a small but measurable effect on the performance results. As expected, a lower pitch angle results in reduced C_T and C_P. These differences increase slightly when changing the advance ratio J. A small change in efficiency can also be observed when showing the efficiency with respect to the advance ratio, but the error becomes near

zero when evaluating the efficiencies of the two blades at the same thrust coefficient T_C.

This effect of pitch uncertainty is used to enhance the analysis of the integrated performance. As stated before, setting the pitch angle can be done to within 0.1°, which is the same as the offset shown in figure 4.7. For further analysis, these measured offsets have been multiplied by 0.5 (as the accuracy of 0.1° leaves a margin of 0.05° in either direction) and afterwards added on top of the 95% confidence intervals. In the case of $\beta = 45°$, these errors can be applied directly, including the variation in error for different advance ratios/thrust settings. When $\beta = 30°$, the mean of the measured errors was used, as no separate sensitivity study was done for this pitch setting.

4.5. Flowfield Data Processing

When processing the flowfield data, it is important to consider the physical differences in the two geometries tested. When evaluating the locations of the tip vortex, a major part of the offset will be caused by the fact that the tip of XPROP-Λ is positioned 20.32 mm further rearwards than the tip of XPROP, which is 10% of the span of the propeller. Where relevant, corrections for this difference will be applied, which will be highlighted in the remainder of this chapter.

The first step when working with the flowfield measurements is turning the raw data into a discretised dataset that can be used for various analysis and visualisation techniques. This processing is done based on pre-existing codes written by Duivenvoorden [10, 32], based on Shaw-Ward et al. [33]. This processing step results in point-averaged data and also determines velocity components based on the various pressures measured. For this averaging, the resolution used was chosen to be 1 mm, meaning that the processed data would be spaced along the measured lines at 1 mm intervals. This value was chosen based on the work by Duivenvoorden [10, 32]. The traverse velocity and sampling rate are required to obtain the required number of samples to concentrate at each required averaged measurement point. During the experiment, some of the measurements were accidentally done at the wrong traverse velocity setting. This was accounted for in the processing, as traverse velocity is a direct input for the determination of the averaged grid resolution.

Once the datasets have been averaged on the grid as described above, they can further be processed. Two processing techniques have been used for most analyses: Firstly, interpolation onto a regular grid to allow for comparing various sets of data. Secondly, applying an offset to the data to compensate for the change in propeller tip position between XPROP and XPROP-Λ.

The effect of the propeller on the flow is the primary interest of this research. To isolate these effects, measurements have been taken where the blades were removed and dummy feet were fitted to the nacelle, in order to have a smooth outer geometry of the hub. Afterwards, these results were subtracted from datasets with either of the propellers mounted, to allow for isolation of their effects.

One of the factors of interest from the experimental data is the overall width of the slipstream. The position of the tip vortex can be used in order to determine this, as this vortex sits on the edge of the slipstream. As detailed in section 4.3, the flowfield has been measured in several spanwise sweeps with the 7-hole probe. For determining the path of the tip vortex, only the horizontal slices are required. To find the core of the tip vortex, each of the individual radial passages of the probe has to be analysed to find the radial position of the vortex on the axial line.

To find the tip vortex core on an individual radial line, the velocity distribution can be used. A typical velocity distribution measured behind a propeller has an increase in the axial velocity (U), with a reduction in U outside the slipstream (see the section around figure 2.7 for more details). Thus, a steep drop in velocity is expected at the boundary of the slipstream. It is assumed that the steepest part of this gradient is at the boundary of the slipstream, and thus at the core of the tip vortex. U is differentiated with respect to the spanwise position y, and the minimum value of the result of this numerical differentiation is at the position of the tip vortex. Due to the nature of the experimental data, there were steep gradients at the extremities of some of the spanwise data. Boundaries were therefore set to exclude these extremities, as it is not expected that the tip vortex passes through either boundary of the flowfield measured. An example of an evaluated velocity profile, including boundaries, can be seen in figure 4.8.

It can be seen from figure 4.8 that the data is somewhat noisy, and that the minimum of dU/dy is at

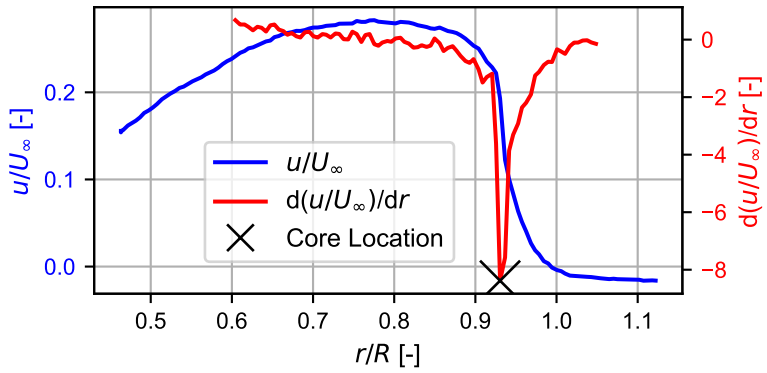

Figure 4.8: Example of tip vortex positioning method, determined using the minimum of the derivative of the induced velocity. Note that there are two different y-axis scales shown. Results shown at $x/R = 1.475$.

a single extreme data point. This can cause some inaccuracies in the determination of the location of the vortex core, and thus, a different method was considered. To increase the accuracy of the determination of local extremes, a Gaussian sub-grid interpolation can be used. With this method, a Gaussian function, as shown in equation (4.3), is used to interpolate the points surrounding the local extremum, to achieve an estimation of the distribution in this region at a higher accuracy. Afterwards, the location of the minimum of this function is used to determine the new, refined vortex core location. An example of this is shown in figure 4.9. The effect of the Gaussian fit on the R^2 values of the determined tip vortex paths, as defined in equation (4.7), is shown in table 4.4.

$$f(x) = \phi_0 e^{-\frac{(x-x_0)^2}{\sigma^2}} \tag{4.3}$$

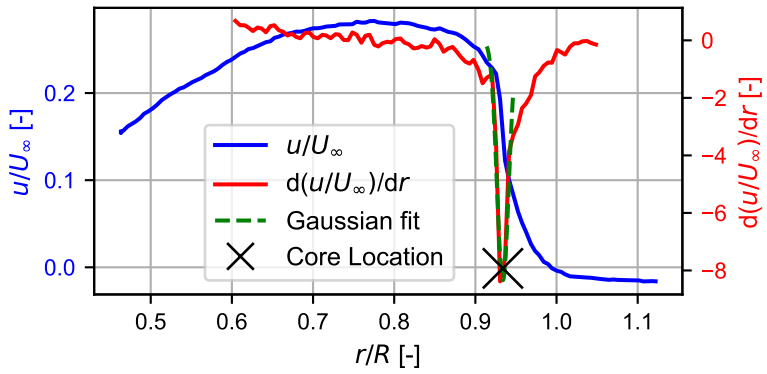

Figure 4.9: Example of tip vortex positioning method, determined using the Gaussian fit. Note that there are two different y-axis scales shown. Results shown at $x/R = 1.475$.

The final step in obtaining the path of the vortex from the individual locations obtained with the method described above. To do this, these individual locations have to be interpolated in order to obtain a function that describes the slipstream boundary shape. The slipstream is expected to contract behind the propeller, as shown in figure 2.2. Based on this shape, it was chosen to use an exponential interpolation to obtain the path of the tip vortex. The exponential function used is shown in equation (4.4).

$$f(x) = a \cdot e^{b(x-x_0)} + y_0 \tag{4.4}$$

To find the best fit for the exponential curve, the parameters a, b, x_0 and y_0 are optimised to reduce the coefficient of determination between the exponential fit and the input data. This coefficient, often called

the R-squared or R^2 value, is computed with equations (4.5) to (4.7).

$$SS_{\text{res}} = \sum \left(r_{\text{measured}} - r_{\text{fitted}}\right)^2 \quad \text{Residual sum of squares} \tag{4.5}$$

$$SS_{\text{tot}} = \sum \left(r_{\text{measured}} - \overline{r}_{\text{measured}}\right)^2 \quad \text{Total sum of squares} \tag{4.6}$$

$$R^2 = 1 - \frac{SS_{\text{res}}}{SS_{\text{tot}}} \quad \text{Coefficient of determination} \tag{4.7}$$

Equation (4.5) shows how to compute the sum of the squares of the residuals. The total sum of the squares is computed with equation (4.6). Finally, the R^2 value is computed using these two sums, as shown in equation (4.7). If the fit of the model is exactly equal to the measured data, SS_{res} is equal to zero, resulting in R^2 being equal to 1. Higher R^2 values indicate a better fit of the model.

The difference of slipstream width between XPROP and XPROP-Λ is a result of interest, and thus this difference was computed by subtracting them. It is important to note that, because this methodology concerns the tip vortex, a coordinate shift was applied to the XPROP-Λ results to artificially shift them forward by the tip offset, as mentioned in the first paragraph of section 4.5.

Table 4.4: Comparison of R^2 values for both the Gaussian and non-Gaussian-based exponential curve fitting.

Propeller	Pitch	Side	Non-Gaussian R^2	Gaussian R^2	ΔR^2
XPROP	$30°$	Workshop	0.9374	0.9727	+0.0353
		Control room	0.9826	0.9928	+0.0102
	$45°$	Workshop	0.6392	0.7141	+0.0749
		Control room	0.9447	0.9481	+0.0034
XPROP-Λ	$30°$	Workshop	0.9386	0.9676	+0.0290
		Control room	0.9719	0.9919	+0.0200
	$45°$	Workshop	0.4255	0.7727	+0.3472
		Control room	0.9187	0.9460	+0.0273

To validate the method outlined above, the computed path of the tip vortex was plotted on top of a velocity field to investigate if the tip vortex path accurately followed the slipstream contraction. An example of this is shown in figure 4.10

A Note on the Flowfield Measurements

Whilst processing the measurements, a noteworthy offset was found. When visualising any of the flowfields, a low degree of asymmetry is expected. However, in the nacelle-only runs, it was observed that the pressure values did not reflect that behaviour. This is shown in figure 4.11a.

In a wind tunnel test section without a propeller present, little variation in the measured pressure is expected. However, it can be seen that there is a clear gradient observed in the gauge pressure. It is important to note that the values of the gauge pressure are taken with respect to a reference pressure measured in the control room of the wind tunnel facility. The raw measured data is shown in figure 4.12. In this figure, the raw pressure data measured by the 7-hole probe is plotted. For these measurements, the path as shown in figure 4.4 was used. The measurement index on the X-axis indicates the number of the specific measurement, and is roughly equivalent to a progression in time. What is shown in figure 4.12 is that all measured pressures for the nacelle-only measurement started at values that were higher than expected, and reduced as the measurement progressed. By the time the probe switched sides between the workshop and control room sides, the pressure had mostly stabilised. This can be used to explain the asymmetry seen in figure 4.11a.

Whilst this asymmetry impacts any plot that directly visualises a quantity related to pressure, it does not have an impact on the velocity plots, because the reference pressure is taken out of that equation. Thus, the velocity results on both sides, shown in figure 4.11b, are assumed to be valid. The assumption is, therefore, that the pressure gradient seen in the plots above is caused by a suspected problem with the measured reference pressure. Upon closer inspection of the other datasets, it seemed like this problem was isolated to the nacelle-only datasets. Even so, it was chosen to focus the analysis on the streamwise velocity, as this data was reliable and sufficient for this thesis.

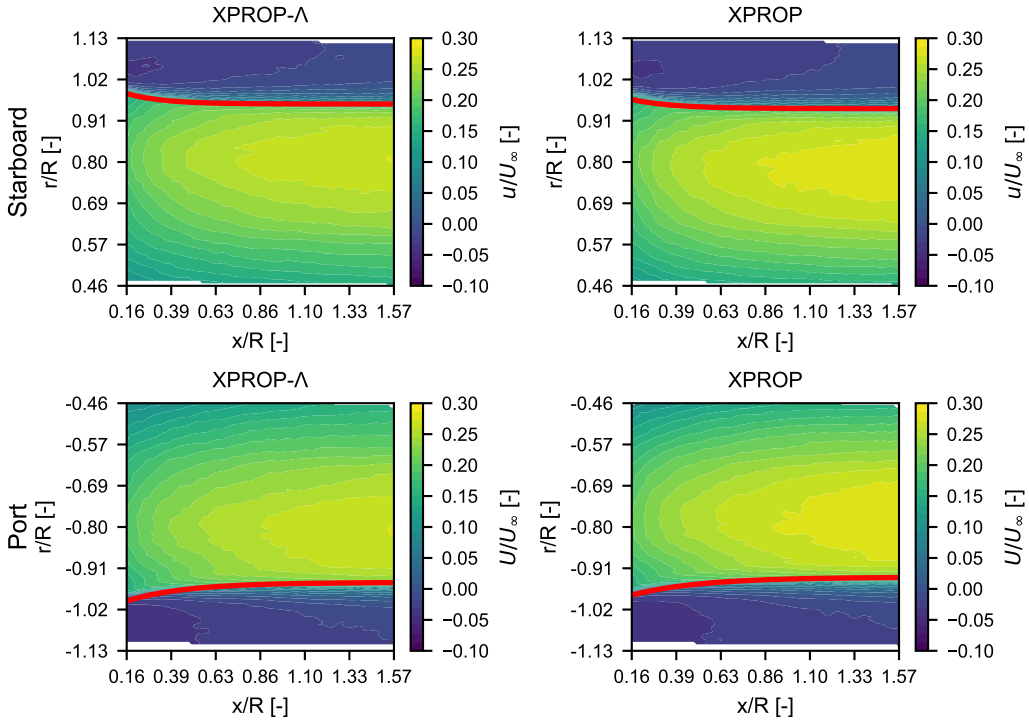

Figure 4.10: Induced velocity fields at $\beta = 30°$ with computed slipstream boundaries

4.6. Testing Procedure

The measurements were done over four days, from 11-03-2025 to 14-03-2025. The two weeks prior have been used for setting up the experiment. As stated before, the measurements can be separated in two distinct categories: Performance measurements, in which various advance ratios are used and measurements for the computation of C_T and C_P are taken, and flowfield measurements, in which the 7-hole probe is moved through the flow to obtain information about the slipstream of the propeller.

- Tuesday 11-03-2025: Most of this day was used to work on the setup, but the first performance measurements were also obtained, all for XPROP-Λ at $\beta = 45°$.
- Wednesday 12-03-2025: The first part of the day was used for finalising the setup. In the afternoon, multiple performance measurements were conducted on XPROP-Λ at $\beta = 45°$, and the horizontal flowfield measurements were also conducted. Some minor problems with the setup were identified and alleviated.
- Thursday 13-03-2025: The final performance measurements on XPROP-Λ at $\beta = 45°$ were conducted in the morning. The flowfield measurements had to be redone after the positioning problem highlighted in section 4.3 was identified and accounted for. The measurements without propeller were afterwards taken, followed by XPROP measurements at $\beta = 44.9°$ and $\beta = 45°$. Finally, the flowfield was measured for $\beta = 45°$.
- Friday 14-03-2025: The program for XPROP at $\beta = 45°$ was finalised. Afterwards, XPROP-Λ was mounted again, this time at $\beta = 30°$. Performance sweeps as well as flowfield were done at the end of the morning and early afternoon, with a final propeller change around 15:00. XPROP was mounted at $\beta = 30°$, and the remainder of the time was used to measure the flowfield, as well as performance sweeps.

The performance measurements have been done in a number of different ways. The advance ratio is the primary variable that was changed during each set of performance measurements. As shown in equation (2.10), the advance ratio depends on the freestream velocity, as well as the propeller rpm. Thus, either of these can be altered to obtain a set of performance data.

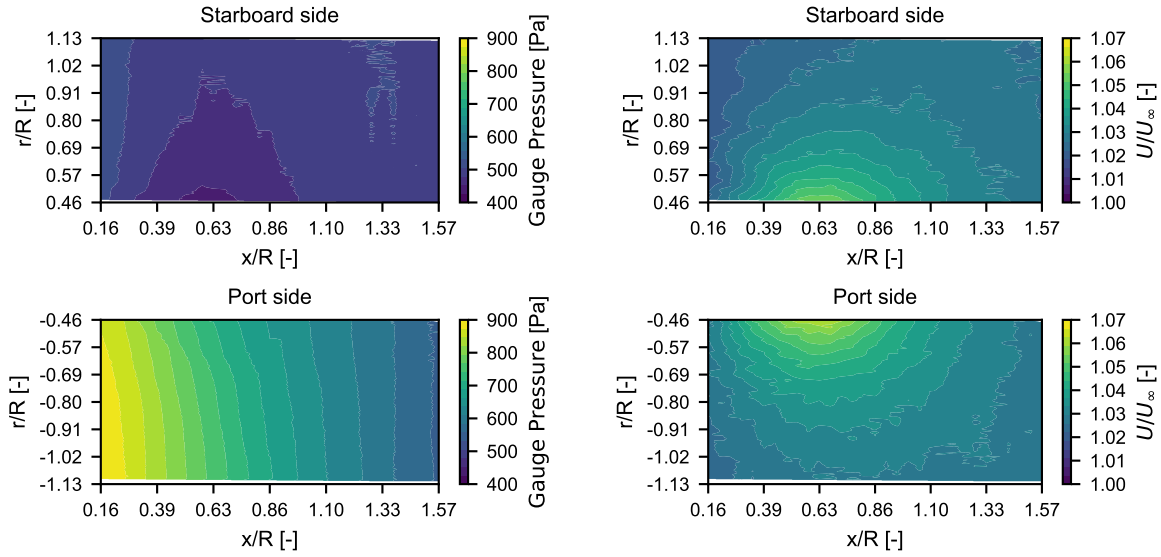

(a) Gauge static pressure fields without a propeller present. Visualised on a normalised grid.

(b) Normalised axial velocity fields without a propeller present. Visualised on a normalised grid.

Figure 4.11: Comparison of gauge static pressure and normalised axial velocity with nacelle only.

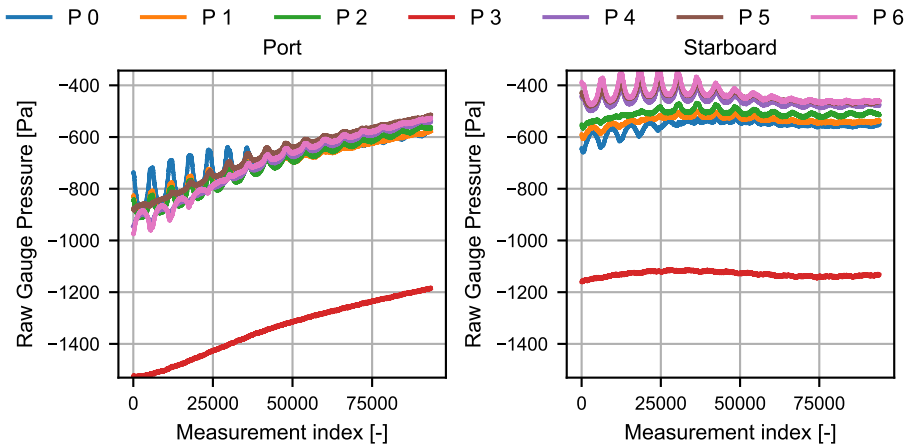

Figure 4.12: Pressure measurements without a propeller mounted.

The procedure for obtaining a set of performance measurements is as follows: Firstly, the tunnel is brought up to a velocity close to the desired Mach number. Whilst the tunnel fan is spinning up, the propeller is turned on, where the thrust must be positive at all times. Once the tunnel and propeller are close to the desired starting condition, control loops are activated. The first control loop controls the wind tunnel and aims to keep it at a steady Mach number. The second loop controls the propeller RPM and attempts to keep this at a constant value. This propeller RPM target can be set based on the desired advance ratio. As the propeller also adds momentum to the flow, it is important to allow the two control loops to balance each other before starting a measurement. The examined advance ratios are shown in table 4.5. When varying the advance ratio by changing the RPM, the only input that needs to be changed is the desired advance ratio for the propeller, resulting in a change in RPM. When doing an advance ratio sweep at constant propeller RPM and varying wind tunnel velocity, no changes are required for the inputs to the propeller, as the controller is set to keep it at a constant RPM. Instead, the wind tunnel fan speed is changed to obtain an advance ratio close to the targets set in table 4.5. Unfortunately, time did not allow for measurements to be taken at all velocities and techniques desired. An overview of the number of runs and type of measurement used for each is shown in table 4.6.

Table 4.5: Examined advance ratio for both pitch settings

Pitch Setting [°]	Advance Ratio [-]
30	0.8, 0.9, 0.95, 1.0, 1.05, 1.1, 1.15, 1.2, 1.3
45	1.4, 1.5, 1.6, 1.7, 1.8, 1.9, 2.0, 2.1, 2.2, 2.3

Table 4.6: Overview of performance measurement methods utilised. For the variable freestream conditions, the number of measurements at each propeller frequency is given.

Propeller	Pitch	Velocity Setup	Number of Measurements
XPROP	30°	M = 0.120	7
	45°	M = 0.090	4
		M = 0.120	5
		Variable	8 (2 at 40 Hz, 4 at 50 Hz, 2 at 60 Hz)
XPROP-Λ	30°	M = 0.090	5
		M = 0.120	7
		Variable	4 (all at 90 Hz)
	45°	M = 0.090	9
		M = 0.120	8
		Variable	8 (2 at 40 Hz, 4 at 50 Hz, 2 at 60 Hz)

Thermal management was a major concern during the performance runs. For all performance measurements, a range of advance ratios was examined, as shown in table 4.5. To ensure minimal operating time required at the highest propeller RPM, these variations in advance ratio were always done from high to low and then back to high, skipping intermediate advance ratios. So, for example, one would go from an advance ratio of 2.2 to 2.0, 1.8, 1.6, 1.4, 1.5, 1.7, 1.9, 2.1 and finish at 2.3.

The fluctuations in the flow velocity due to the two control loops, for Mach number and propeller RPM, do not cause problems for the load measurements, as these are averaged over time. When taking the flowfield measurements, variations in the flow should be kept to a minimum because each location in the flowfield is only measured for a short time. Thus, the control loops cannot be used. Instead, the propeller RPM is set to a constant value, and a different control loop is used for the wind tunnel velocity, which has a velocity target instead of a Mach number target. This combination reduces the fluctuations in the wind tunnel freestream sufficiently to be satisfactory for taking flowfield measurements using the 7-hole probe.

Table 4.6 shows the number of measurements for each of the set of operating conditions. For the experimental data, all the measurements have been used, which is shown in section 6.1. For the comparisons with the lifting-line methods, it was chosen to only use the $M = 0.12$ data. This decision was made in part because the lifting-line tool was designed to operate at varying propeller RPM for a constant freestream velocity, thus disqualifying the variable velocity/Mach number runs. Additionally, the 2D airfoil polar data is less reliable at low Reynolds numbers. Thus, it was chosen to evaluate the lifting-line models only at $M = 0.12$ and not at $M = 0.09$. More information about the lifting-line method can be found in the next chapter.

5

Modelling Methodology

This chapter describes the method used for computing the aerodynamic performance of propellers. The computational framework used is a lifting-line method. Development on the lifting-line method focuses on conventional wings, but as noted by the Wright brothers [34], "screw-propellers are simply wings traveling in a spiral course". Thus, modern lifting-line methods can be used for computing the aerodynamic characteristics of propellers, in addition to conventional wings. In this chapter, background information about the lifting-line methodology is provided, as well as details on the specifics of the lifting-line tool used in this thesis.

5.1. Lifting-Line Methods

The lifting-line method is one of the older methods available for the computation of wing lift. This analytical method was developed both by Lanchester and Prandtl in the early 20th century [15, Section 5.7]. In this method, a finite wing is replaced by a bound vortex. However, as described by Helmholtz's vortex theorems (a vortex filament has a constant strength and cannot end in a fluid), there must be trailing vortices downstream from the wingtips as well. Due to their shape, this is also referred to as a horseshoe vortex. The trailing vortices induce downwash onto the bound vortex. However, modelling a wing as having a constant circulation is not an accurate reflection of reality. Instead, the wing can be modelled by several superimposed horseshoe vortices, see figure 5.1. The bound vortices are applied along a single line, which is called the lifting-line. The resulting system can be solved analytically. A more detailed explanation can be found in Anderson, Jr. [15, Chapter 5].

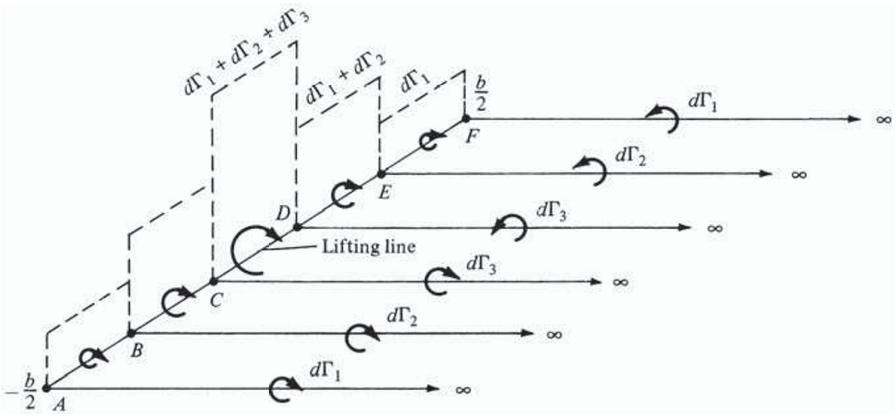

Figure 5.1: Distributed horseshoe vortices, from Anderson, Jr. [15, p. 438].

The original lifting-line methodology was developed for straight wings, with the assumption of thin airfoils, thus having a C_l-α slope $\left(\frac{\mathrm{d}C_l}{\mathrm{d}\alpha}\right)$ of 2π. Both of these limitations were areas of development in the

20th century, with Weissinger [35] extending the theory to work for wings with swept quarter-chord $\left(\frac{c}{4}\right)$ lines. With his method, each section is forced to satisfy Pistolesi's boundary condition, which stipulates that there is flow tangency at the $\frac{3c}{4}$ chord point. Additionally, Sivells et al. [36] published a method to include non-linear airfoil polar data, thus removing the assumption of the 2π value for $\frac{\mathrm{d}C_l}{\mathrm{d}\alpha}$. Both advances made the results of lifting-line methods more generally applicable but also more complex to solve, which is one of the reasons that numerical methods for solving the lifting-line problem have been developed.

The lifting-line method can be solved using various numerical approaches. Though these techniques rely on the classic theory from Prandtl and Lanchester, they replace the analytical solutions with computational ones. One of the earliest such numerical schemes for solving a lifting-line problem was published by Anderson, Jr. et al. [37] in 1980, with multiple methods being published since then. Solving the lifting-line problem has since been done in two distinct ways, based either on Weissinger [35] or Phillips et al. [38]. These methods will be discussed further in the subsequent paragraphs. It is important to note that for both lifting-line methods discussed, the vortices are not superimposed such as shown in figure 5.1, but instead are placed side by side, as shown in figure 5.2.

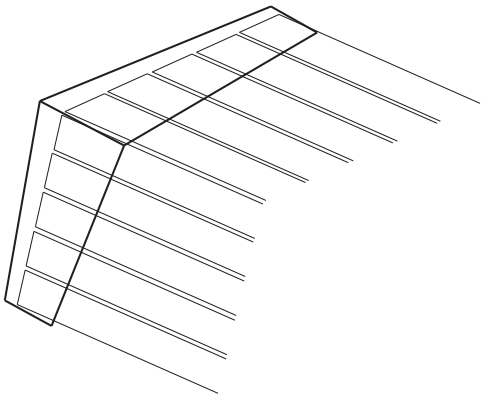

Figure 5.2: Side-by-side horseshoe vortices, form Hunsaker [39].

There are a number of assumptions behind the lifting-line methods, which apply to the classical formulation from Prandtl as well as the more modern numerically solved formulations. These assumptions are the following:

- Inviscid flow: The boundary layer and turbulent effects are not accounted for. The viscous terms are removed from the Navier-Stokes equations. It is important to note that some of the viscous effects are still present in the 2D airfoil polar data, but this is not the same as accurately modelling the boundary layer behaviour and turbulent structures in the flow.
- Potential/irrotational flow: The vorticity in the flow is ignored.
- Incompressible flow: No compressibility effects are present in the flow. Similar to the viscous effects, some of these effects are reintroduced by the airfoil polars.

The assumptions above enable the formulation of the lifting-line method, but introduce inaccuracies as well. The viscous and compressibility effects are exclusively represented in the 2D airfoil data, which leads to inaccuracies in flows with strong 3D phenomena. A more detailed explanation of 2D airfoil polars and their significance is provided in section 5.3. The next sections will discuss the lifting-line methods used for the remainder of this thesis.

Naming Convention for the Lifting-Line Methods

Within this thesis, two computational methods for solving the lifting-line problem are used. Traditionally, these are referred to as the Γ-method and α-method [7, 40, 41]. These names are used as it is posed that the circulation Γ and the effective angle of attack α are the quantities that are iterated to obtain a solution. However, these names are not necessarily accurate. As will be shown in section 5.1.1, it is not the circulation that is used to iterate, but instead the lift force. Thus, this method will be referred to as the lift-based method. For the α-method, it should be noticed that the effective angle of attack is

only used to incorporate the viscous effects on the $\frac{\mathrm{d}C_l}{\mathrm{d}\alpha}$-slope. Thus, in the case of inviscid flows, this name would be incorrect, and thus a different name is required. The lifting-line problem is closed by applying the Pistolesi boundary condition, which enforces flow-tangency. Therefore, this method will be referred to as the flow-tangency-based method from hereon.

5.1.1. The Lift-Based Method

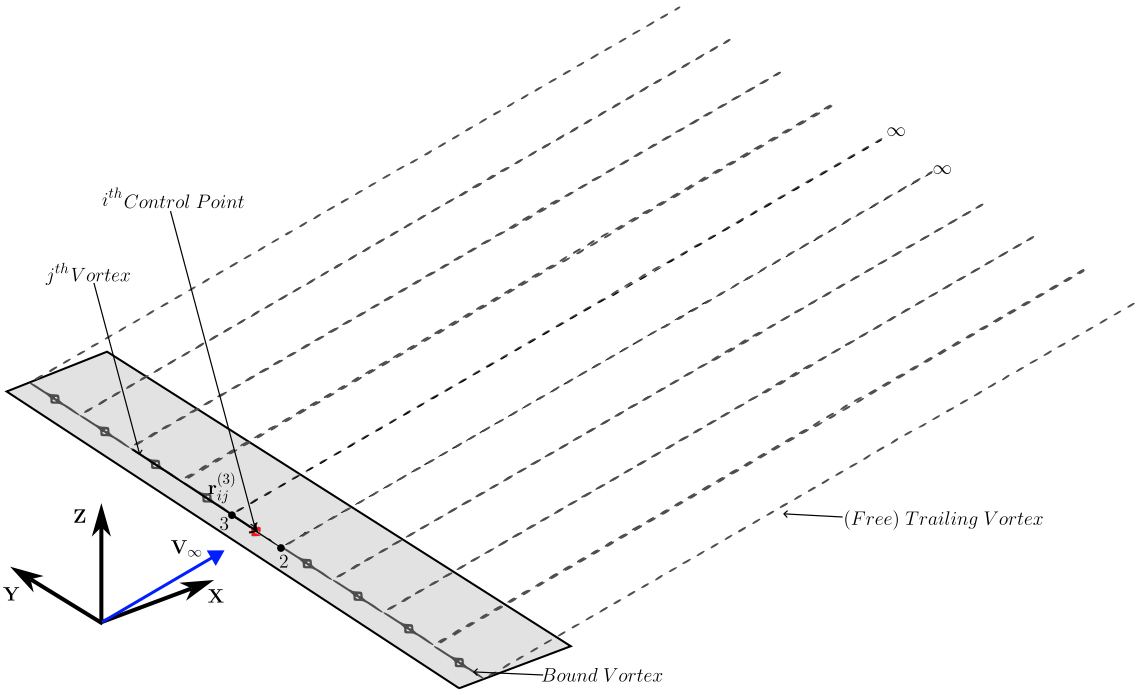

Figure 5.3: The lift-based method, based on Phillips et al. [38]. Image from Chreim et al. [41].

The first method to discuss is the lift-based method. This method solves the non-linear system of equations that makes up a numerical formulation of the lifting-line method through iteratively determining the lift force in two different ways and comparing these. The basis of the modern lift-based method was published by Phillips et al. [38]. In the lift-based method, a wing is discretised using a distribution of horseshoe vortices, a set of lifting-lines [42]. Both the bound vortices and the control points are placed at the quarter-chord, as shown in figure 5.3. The aerodynamic force on any section can now be expressed in two ways, either based on the section lift coefficient, equation (5.1), or from the vortex lifting law, equation (5.2). The formulations below are adapted from Chreim et al. [41]:

$$\left|\vec{F_j}\right| = \frac{1}{2}\rho U_\infty^2 C_l(\alpha_{\text{eff},j})\mathrm{d}A_j \tag{5.1}$$

$$\vec{F_j} = \rho\Gamma_j\vec{U_j} \times l_j \tag{5.2}$$

In equation (5.2), $\vec{U_j}$ is the local velocity, which is a combination of the freestream velocity and the induced velocities from the vortex system. Equations (5.1) and (5.2) are then combined, which is the basis for an iterative solver that iterates until both lift-forces are equal to within the convergence criterion. More details on the underlying mathematics can be found in Phillips et al. [38] and Chreim et al. [41].

5.1.2. The Flow-Tangency-Based Method

The flow-tangency-based method is based on the earlier mentioned work by Weissinger [35]. The system of equations is closed by enforcing Pistolesi's boundary condition at the control point, which enforces flow tangency at the control point. It uses the effective angle of attack α_{eff} to determine the loads on a blade, as well as the local circulation. Compared to the lift-based method, the control points are no longer on the bound vortices, but instead at approximately $0.75c$, as shown in figure 5.4.

The flow-tangency-based method enforces Pistolesi's boundary condition. Initially, this condition is applied at $0.75c$. This initial guess is required to allow for a first calculation of the local loads, and is

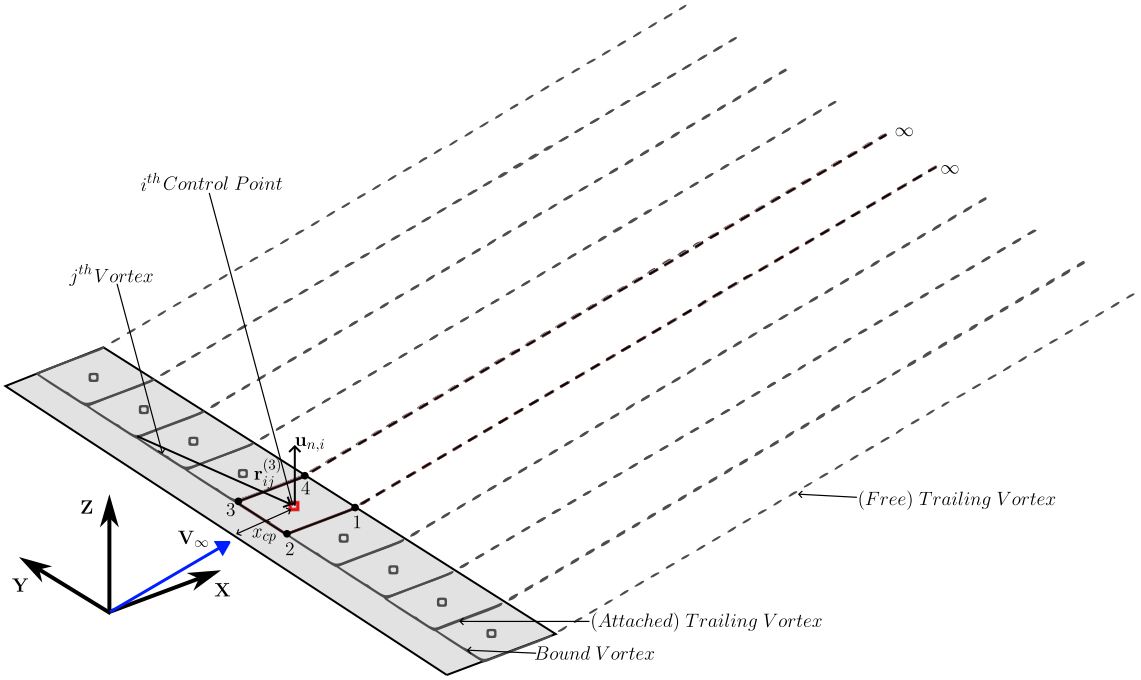

Figure 5.4: flow-tangency-based method, based on Weissinger [35], image from Chreim et al. [41].

based on an assumed value for $\frac{\mathrm{d}C_l}{\mathrm{d}\alpha}$ of 2π. To implement the viscous effects, the following steps are iterated over until a converged solution is found [41]:

1. Obtain the local lift coefficient at iteration n, $C_{l,i}$.
2. Calculate the local angle of attack at station i for iteration n, $\alpha^n_{\text{eff},i}$. This is done based on the $\frac{\mathrm{d}C_l}{\mathrm{d}\alpha}$ of iteration n
3. The viscous lift curve slope is determined from 2D airfoil polars, corresponding to α_{eff}.
4. The computed lift curve slope is compared to the slope extracted from the airfoil polar database
5. A residual is computed based on the difference between the two slopes. This residual R_i is used to correct the computed lift curve slope. This new estimate is calculated using the following:

$$\left(\frac{\mathrm{d}C_l}{\mathrm{d}\alpha}\right)_i^{n+1} = \left(\frac{\mathrm{d}C_l}{\mathrm{d}\alpha}\right)_i^{n} + \Omega R_i \tag{5.3}$$

   In this equation, Ω is a relaxation factor.
6. A new location for the control point is calculated using equation (5.4):

$$x_i = \left(\frac{1}{2}\frac{(\mathrm{d}C_l/\mathrm{d}\alpha)_i}{2\pi} + \frac{1}{2}\right) c_i \tag{5.4}$$

   In this equation, c_i is the local chord length.
7. The local velocity and the circulation Γ_i^{n+1} are calculated.
8. Repeat until the residual vector R_i satisfies the convergence criteria.

The location of these control points is changed to iterate towards the α_{eff}. A more detailed description of the flow-tangency-based method is provided in Chreim et al. [40] and Chreim et al. [41].

The main difference between the lift-based method and the flow-tangency-based method is the variable that is iterated to obtain a solution, as is highlighted above. Another way of explaining the difference between the two lifting-line methods is to evaluate the method in which the Kutta condition is applied. A case could be made that enforcing flow tangency at approximately $0.75c$ effectively moves the Kutta condition away from the trailing edge and to this control point. This is an important difference between

the two methods, as only the flow-tangency-based method uses Pistolesi's boundary condition, as the control point location is modified to account for the viscous effects on the airfoil polars.

Chreim et al. [41] showed that for swept wings, the lift-based method converged poorly whereas the flow-tangency-based method did not. They also concluded that the flow-tangency-based method was generally superior for any implementation, regardless of the geometry investigated, when comparing the results with experimental data. They suggest that the flow-tangency-based method is therefore the better suited of the two to extend the lifting-line method onto more complex geometries, which propellers are.

5.2. Application of Lifting-Line Methods to Propellers

As described in the introduction of this chapter, one must remember that the explanations in section 5.1 are all written for applications of aircraft wings, which are different from propellers. Even though, as noted before, a propeller is a rotating wing, some adjustments need to be made in order for the lifting-line method to work for a propeller.

It must be taken into account that the propellers themselves are not stationary, but instead rotate around an axis. The wake can therefore no longer be represented by a straight line behind the trailing edge, but instead has a helicoidal shape. This shape consists of multiple elements, all of which are individually straight lines. Figure 5.5 shows an example of these individual straight elements. It is assumed that all blades are identical, which simplifies the calculation, as only one wake needs to be initially computed and subsequently repeated for the number of blades.

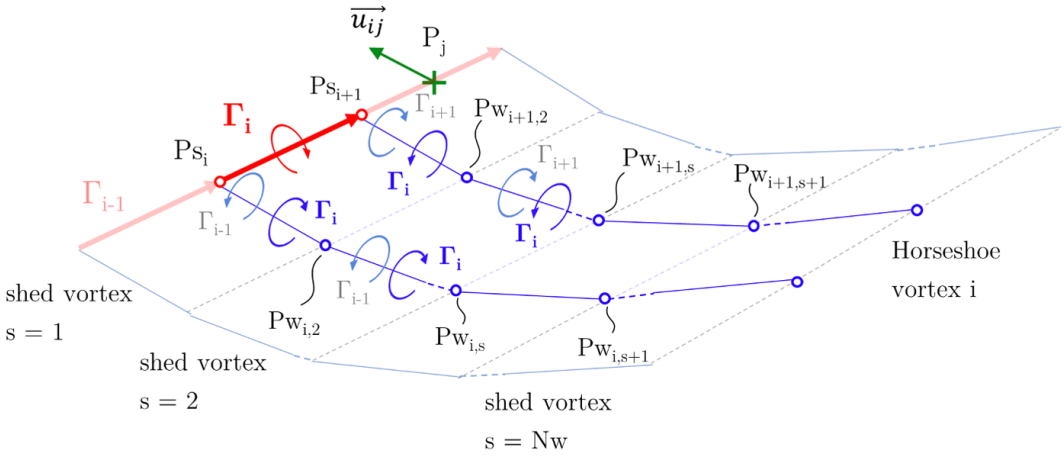

Figure 5.5: Wake structure example with multiple elements, obtained form Margalida [8, private communication].

Within the tool used, the wake[1] can be modelled in three different ways, as a frozen, semi-free or a free wake [5]. A frozen wake is a wake which is not updated based on the circulation of the propeller, but instead is computed exclusively on an initial input provided by the user. The acceleration and shape of a semi-free wake are computed based on the results of each lifting-line iteration. A free wake has a time step built in, which is used to calculate each new wake panel. In this thesis, the semi-free wake application is used. This is computationally cheaper than the free wake, reducing overall time, whilst still taking propeller performance into account.

5.3. Airfoil Database Sourcing

An important part of the numerical modelling of a lifting-line is the source of airfoil polar data. An airfoil polar provides to the relation between angle of attack α, the lift coefficient C_l and the drag coefficient C_d. Having accurate information about the aerodynamic characteristics of the airfoils used is key to having accurate lifting-line results.

[1]Technically, a propeller has a slipstream, but it was chosen to stick with the term wake in this section to be consistent with the code and sources used.

Two options are available for sourcing the airfoil data for the lifting-line methods used for this thesis, both with different benefits and drawbacks. The first method is based on CFD simulations of the XPROP airfoils. The CFD simulations were conducted using Ansys Fluent [43], but were not conducted at settings that are directly applicable to the wind tunnel experiment. The CFD cases were conducted at a Reynolds number of 6.5 million, resulting in Reynolds numbers that are approximately 20 to 30 times higher than those seen in the wind tunnel. An increase in Reynolds number means that the viscous effects are less significant on the flow, resulting in lower values for the drag coefficient. Additionally, the maximum lift of an airfoil, $C_{l_{\max}}$, is increased for flow with higher Reynolds numbers. These effects are shown in figure 5.6. Thus, these airfoil polars do not accurately reflect the performance of the blades used in the wind tunnel, despite their geometric similarities.

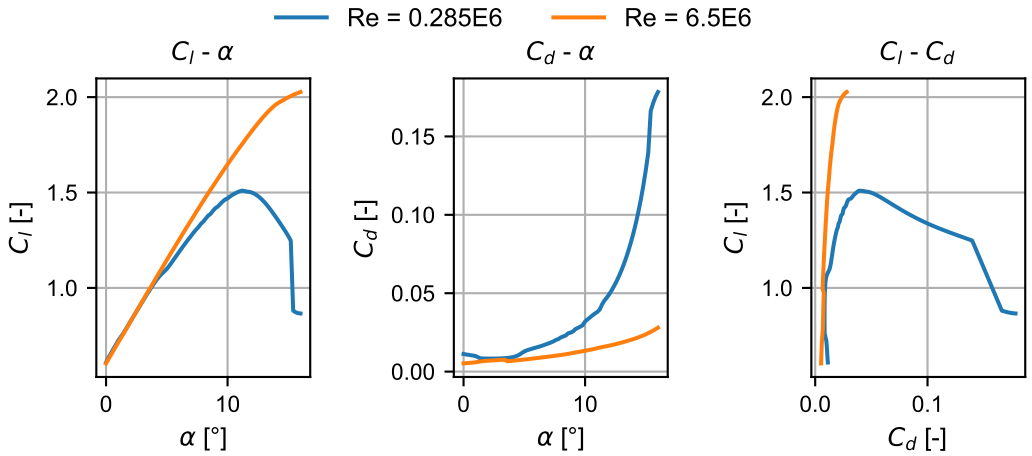

Figure 5.6: Comparison of airfoil polars of the XPROP airfoil at $r/R = 0.825$ at Reynolds numbers of $0.285 \cdot 10^6$ and $6.50 \cdot 10^6$. Results obtained using XFOIL [26].

The second method of obtaining 2D airfoil polars is based on the NACA 4-series. These airfoils, developed in the 1930s by NASA's predecessor, the National Advisory Committee for Aeronautics, which is where their name originates [44]. The 4 series is named as such because four numbers are used to describe the airfoil by indicating the position and magnitude of maximum camber, as well as the maximum thickness. From these four numbers, using the equations shown in [45], airfoil coordinates can be computed. There are, however, limitations to this approach, as not all airfoil shapes can accurately be approximated by the NACA 4-series.

To analyse a propeller with custom airfoils, such as the ones used by XPROP and XPROP-Λ, the closest 4-series airfoil must be found to approximate the polar of the custom airfoil. This approximation is done by splitting the airfoil into an upper and lower half, and afterwards comparing the custom airfoil with all possible NACA 4-series airfoils, and picking the airfoil with the lowest combined root-mean-square error between the two airfoils. Splitting the airfoil into an upper and lower half is required to ensure that there are not multiple values present at a single X-coordinate. However, as mentioned before, this often is not a perfect approximation, as shown in figure 5.7. This figure shows that the best NACA 4-series approximation of one of the XPROP airfoils is close but notably different, with a sharper leading edge than the custom airfoil and less forward camber. These differences, although they seem small, will have a significant impact on the polars, as shown in figure 5.8. When close to stall, it can be seen that the calculated polars for the XPROP airfoil show different behaviour than the NACA5506 airfoil. This figure is also a good example of one of the limitations of XFOIL, which is the tool used for the computation of the 2D polar data.

The XFOIL tool, see Drela et al. [26], is a panel-based solver for 2D subsonic airfoils. It is able to compute viscous effects as well as inviscid flows, and can be used to quickly obtain polars for a wide range of airfoils. A free transition model is used, based on the e^N method, using the default $N_{\text{crit}} = 9$ [46]. Contrary to the XPROP polars, which were built using CFD, all NACA 4-series polars were computed using XFOIL. The viscous model of XFOIL does not converge for fully separated flows, which means

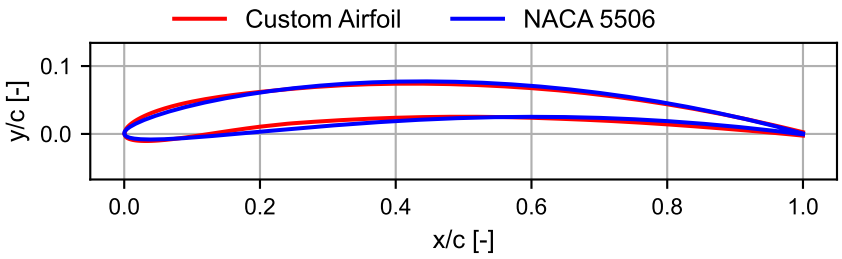

Figure 5.7: Comparison between the airfoil of XPROP at $r/R = 0.825$ with its closest NACA 4-series match.

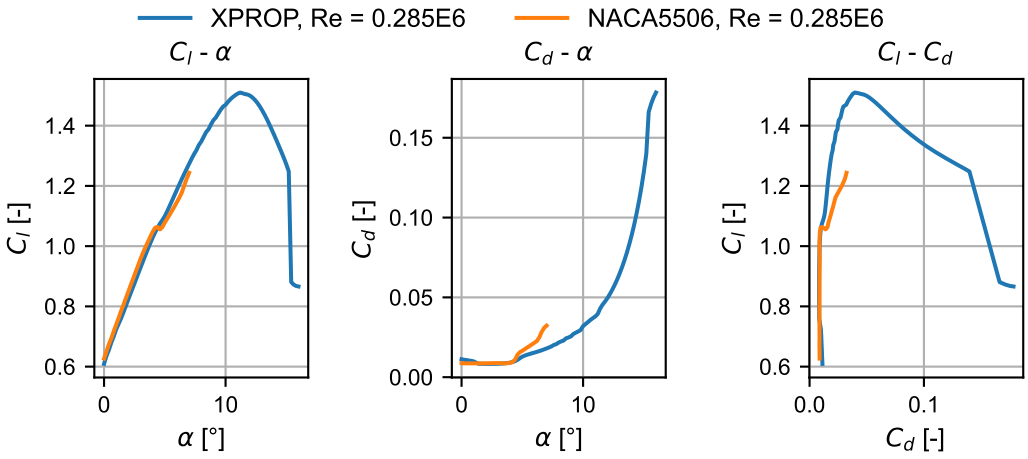

Figure 5.8: Comparison between the XPROP airfoil at $r/R = 0.825$ and closest NACA 4-series equivalent. Results obtained using XFOIL [26].

that airfoil polars based on XFOIL are limited in terms of angle of attack range. This is shown by the NACA5506 results in figure 5.8. This figure also shows that the relatively small geometric change, as shown in figure 5.7, results in notably different stall behaviours as predicted by XFOIL.

XFOIL also computed non-physical results at the lowest Reynolds numbers investigated. Figure 5.9 provides an example of the behaviour seen in these polars. It can be seen that the polar for Re = 25,000 has a reflex in the $C_l - \alpha$ curve around $\alpha = 0°$, which is not expected. Additionally, the relation between C_l and C_d also shows unexpected behaviour, with an increase in C_l resulting in a decrease in C_d at Reynolds numbers up to 175,000 for the case shown in figure 5.9. Further investigation into the XFOIL data did not explain this behaviour. All of this is to show that there are two problems with the NACA 4-series-based method: Firstly, the deviation in airfoil shape results in different airfoil polars, primarily in the stall characteristics. Secondly, the polars at low Reynolds numbers are inaccurate due to the nature of XFOIL, which is not suitable for computing polars at these conditions.

Both the XPROP-airfoil and the NACA 4-series based method have benefits and drawbacks. The XPROP-based method underestimates the drag coefficient and overestimates the lift at high angles of attack, due to the high Reynolds number. The NACA 4-series based method does not predict the stall of thin airfoils well, because XFOIL is not suited for conditions where the flow is mostly separated. It also predicts non-physical behaviour at low Reynolds numbers. In chapter 7, the two different sources for the polar data are used and compared.

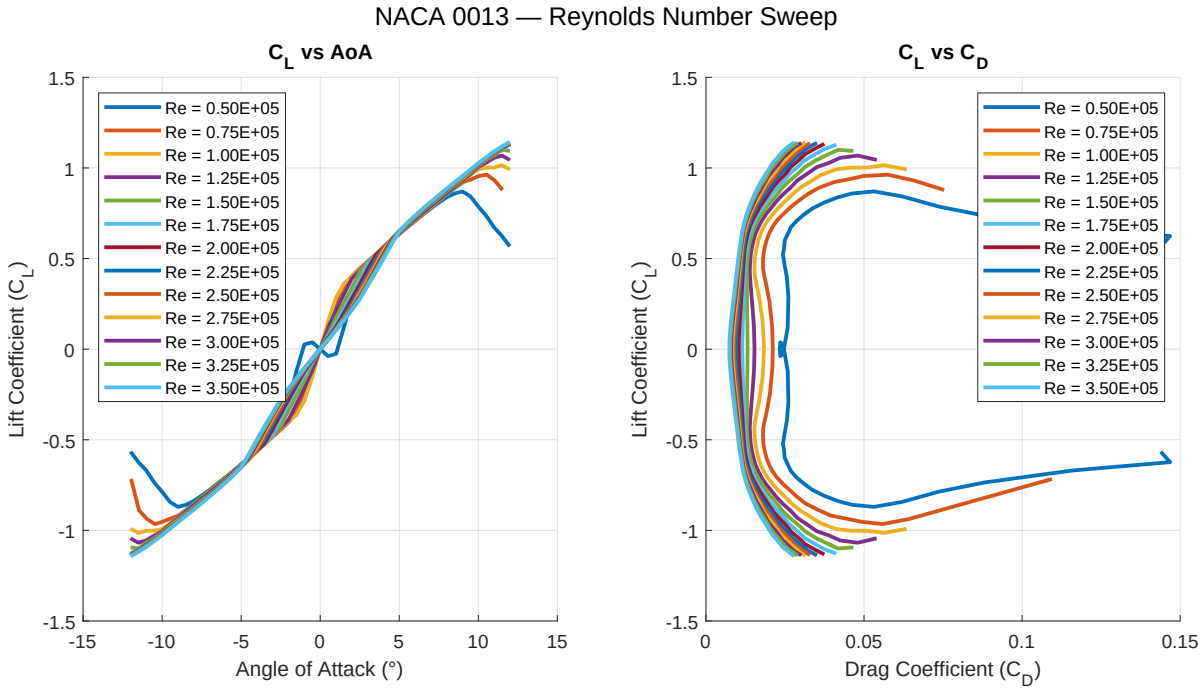

Figure 5.9: Lift and drag polars for a NACA 0013 airfoil over a range of Reynolds numbers, computed using XFOIL [26].

Part III

Results

6

Experimental Results

This chapter presents the results of the experimental campaign, which is described in chapter 4. First, the measurements of the integrated performance parameters are discussed, which include comparisons between XPROP and XPROP-Λ as well as a note on the sensitivity of setting the correct pitch angle. Afterwards, the results of the flowfield measurements are shown.

6.1. Performance Measurements

The figures in this section show the thrust and power coefficients of XPROP and XPROP-Λ at two pitch settings, as well as the achieved propulsor efficiencies of these setups. The efficiency is shown in two ways, once as a function of the advance ratio J and once compared to the thrust coefficient T_C. Evaluating the efficiency at equal T_C means that the disk loading is the same between the blades, thus evaluating the efficiency at an equivalent thrust setting. The curves shown are the output of response models based on a 3rd degree linear regression through the measured data. Please note that these fits should not be used for any extrapolation, but exclusively for analysing results over the range of advance ratios measured. Additionally, the 95% confidence intervals associated with the regressions are shown. The confidence intervals presented are rather narrow, which can be attributed to the high number of measurement points examined. The confidence intervals do not include systematic errors that can be present. One such systematic error is the inaccuracy due to the manual setting of the blade pitch angle. The effects of this uncertainty, as discussed in section 4.5, are shown in figure 6.1 by dotted lines.

Figure 6.1 shows the performance parameters measured for the two propeller configurations at a freestream Mach number of 0.12, at both pitch angles investigated. What can be seen from these graphs is that the differences between XPROP and XPROP-Λ are quite small, and all within the pitch uncertainty margin. It can be seen that the sweep distribution of XPROP-Λ results in a slight reduction in the thrust and power coefficients, and a small increase in propulsive efficiency. It is important to note that this is all within the pitch uncertainty margin. This is an important detail, as it shows that the difference between XPROP and XPROP-Λ at the investigated operating conditions is small and within the uncertainty margin.

As shown in section 4.6, experimental measurements were taken at various operating conditions. To investigate the effect of changing the Reynolds and Mach numbers, one can compare these datasets. The first of these comparisons is shown in figure 6.2. In this figure, the difference between the 0.12 and 0.09 Mach number cases is shown. The integrated performance parameters for $M_\infty = 0.09$ are shown in figure D.1. Please note that, as highlighted in table 4.6, no data is available for XPROP at 30 degrees of pitch for operating conditions other than $M_\infty = 0.12$. Figure 6.2 shows that the thrust and power coefficients are larger for the higher freestream velocity case, and that the difference increases with advance ratio, where these differences are larger than the pitch uncertainty. It is hypothesised that the change in Reynolds number is of a larger effect than the change in Mach number, as the freestream Mach numbers, as well as the tip Mach numbers, are predominantly below 0.3 and thus, the effect of

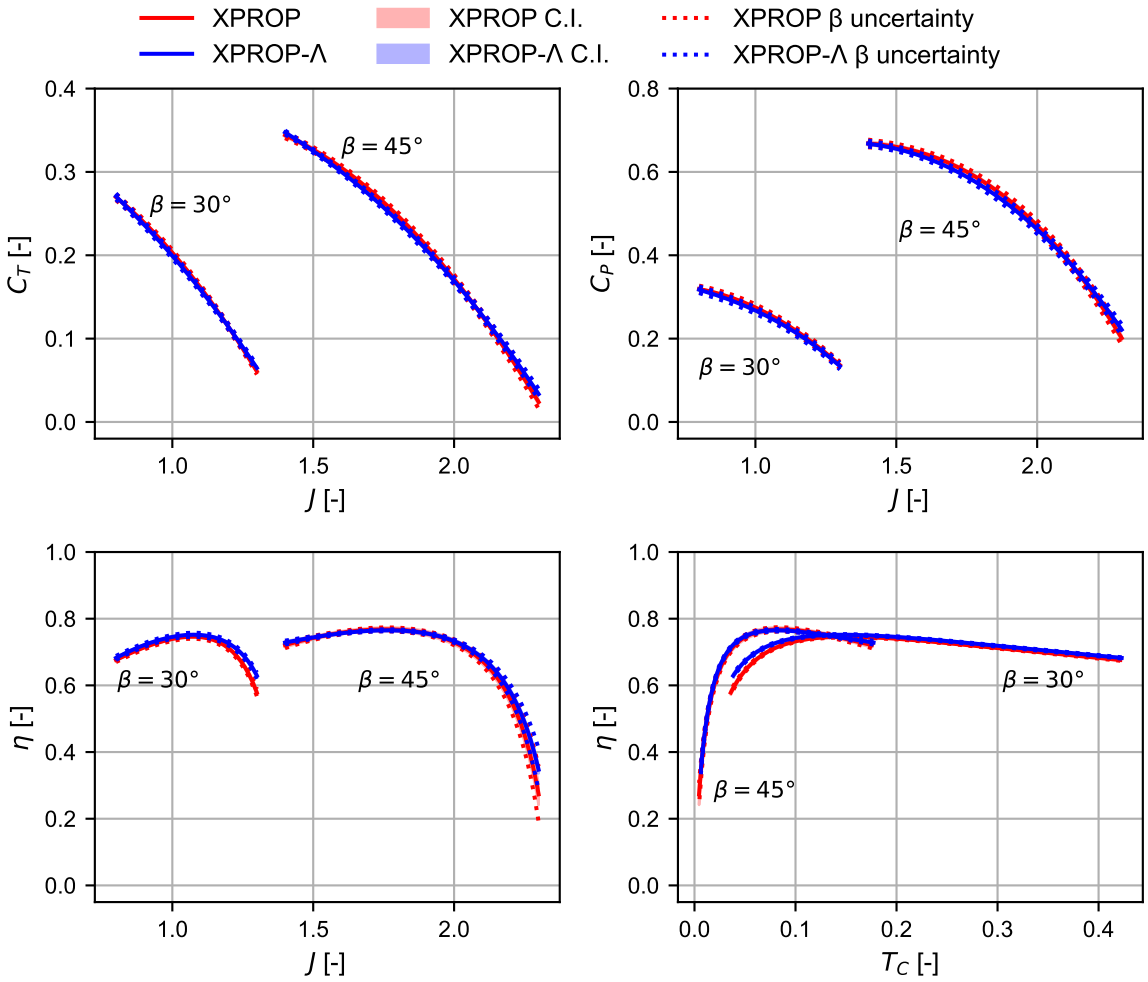

Figure 6.1: Performance curves from wind tunnel measurements at $M_\infty = 0.12$, for $\beta = 30°$ and $\beta = 45°$. Includes 95% confidence intervals as well as the effect of pitch angle uncertainty.

compressibility is small. The increase in the thrust and power coefficients for an increased freestream velocity suggests that the section lift of the propeller is increased with an increase in Reynolds number. This may be explained with the following reasoning: The boundary layer of an airfoil changes the effective camber of an airfoil, effectively reducing it and therefore reducing the section lift. An increase in Reynolds number reduces the boundary layer thickness, increasing the local lift and therefore C_T and C_P. A second explanation could be that the state of the boundary layer changes due to the change in Reynolds number, possibly removing a region of laminar separation at the lower Reynolds number case. Another known phenomenon is that the contribution of viscous forces to the section drag is reduced when the Reynolds number increases. The drag coefficient is predominantly influential to the power coefficient, and such a reduction in C_d will result in a reduction in C_P as well. This explains why C_P has a smaller relative increase than C_T for an increase in Reynolds number, and thus why the efficiency increases as well, as seen in figure 6.2.

It is notable that the effect of the freestream velocity on XPROP and XPROP-Λ is similar, and that the 95% confidence intervals of the differences for both propellers overlap for most of the investigated range. This shows that whilst the effect of changing the freestream conditions between $M_\infty = 0.12$ and $M_\infty = 0.09$ is significant, most of the difference between the two blades is within the 95% confidence intervals, except for the region where J is between 2.0 and 2.2. It is also notable that the effects of the change in freestream velocity on the performance characteristics shown in figure 6.2 are the largest at high advance ratio/low thrust setting conditions. When operating the wind tunnel at a constant freestream velocity, changing the advance ratio is done by changing the propeller RPM. Hence, the

Reynolds number reduces when increasing the advance ratio, resulting in a larger relative difference in Reynolds number between the $M = 0.12$ and $M = 0.09$ cases at these operating conditions.

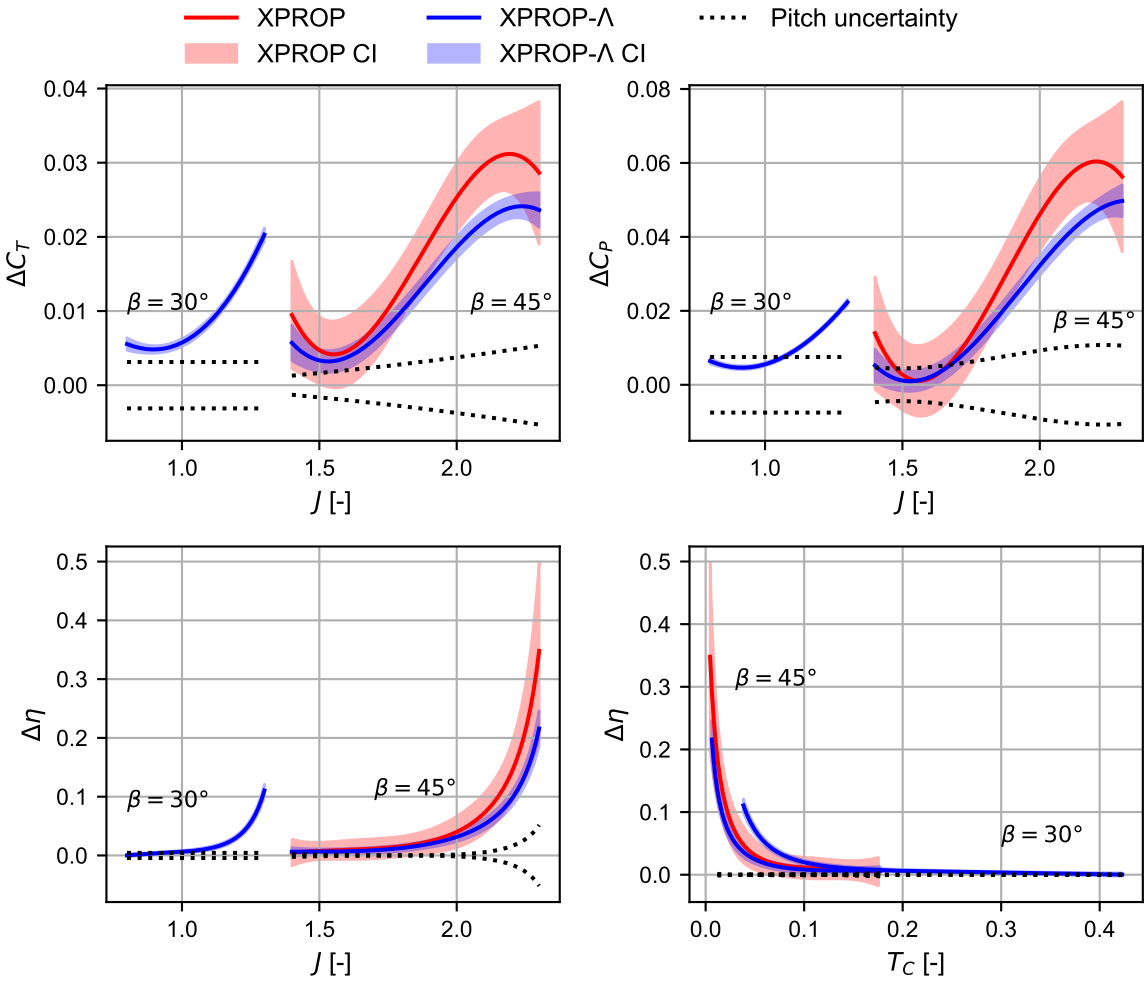

Figure 6.2: Difference between $M = 0.12$ and $M = 0.09$ measurements (Difference shown is $M = 0.12$ minus $M = 0.09$).

Another way of changing the advance ratio is by keeping the propeller RPM constant and changing the freestream velocity instead, where an increase in freestream velocity results in an increase in advance ratio. Using this method results in a different relation between the advance ratio and Reynolds number. With this method, a higher advance ratio results in a higher Reynolds number, which is the opposite of the constant freestream method. The results for this method of measuring are shown in figure 6.3, combined with the constant freestream condition cases for XPROP at 45 degrees of pitch. The measurements with variable freestream velocity have been taken at three different propeller frequencies, which are shown separately. A similar figure for XPROP-Λ is available in appendix D, in figure D.2.

A number of observations can be made based on figure 6.3. In these figures, no pitch uncertainty margins are provided, as all these measurements were done for a single instance of pitch setting. Thus, whilst there still is an effect due to the manual pitch setting process, this will be the same for all measurements shown, and thus does not need to be accounted for. It can be seen that the 95% uncertainty margin is wider for the variable freestream velocity cases, especially at 40 Hz. This can be explained twofold: Firstly, only two sets of measurement data are available for this case, instead of the four to nine for other operating conditions. Secondly, at 40 Hz, the loads on the propeller are the lowest of all operating conditions investigated, leading to a larger inaccuracy in the measurements, because the relative effect of the sensitivity of the RSB is larger. However, even taking these results into account, some general trends can be observed. A higher propeller frequency leads to higher thrust

and power coefficients, as well as efficiencies. This can again be explained by an increase in Reynolds number, similar to the results discussed when analysing figure 6.2. The difference between the 40 and 50 Hz measurements is smaller than that between 50 and 60 Hz. When comparing two cases at higher propeller frequencies, the relative difference in Reynolds number is smaller, explaining the reduced change.

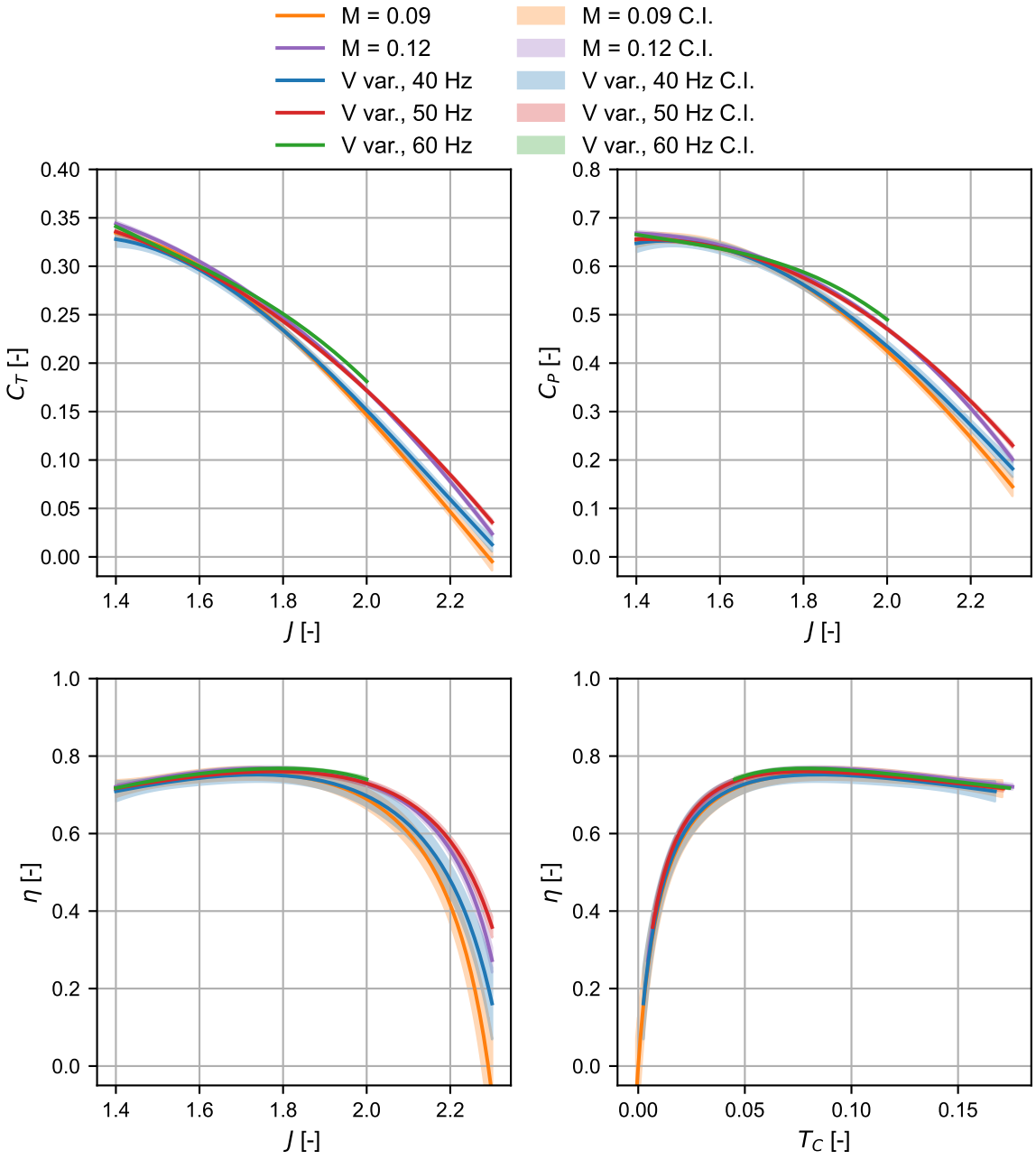

Figure 6.3: Overview of experimental results for XPROP at $\beta = 45°$, for the five different measurement conditions.

Another observation is that gradients $\mathrm{d}C_T/\mathrm{d}J$ and $\mathrm{d}C_P/\mathrm{d}J$ are smaller for the variable freestream velocity cases. This can be explained by the previously stated difference between these two in the relation between the advance ratio and the Reynolds number. As shown in figure 6.2, an increase in Reynolds number increases the thrust and power coefficients. At the same time, increasing the advance ratio reduces the values of these coefficients. The previously described increase in the Reynolds number for variable freestream velocity operating conditions with an increased advance ratio causes the observed reduction in the $\mathrm{d}C_T/\mathrm{d}J$ and $\mathrm{d}C_P/\mathrm{d}J$ gradients.

The analysis of the experimental results for integrated performance measurements has shown that there is a clear effect of the changing operating conditions and Reynolds number on the measured values, but that the effect of the sweep distribution of XPROP-Λ seems to be consistent between them and rather small. In addition to investigating the integrated performance of the propellers, flowfield measurements were taken. The next section discusses those.

6.2. Flowfield Measurements

Whilst the aerodynamic performance shows only small differences between XPROP and XPROP-Λ, this does not necessarily mean that there are no other differences that can be observed. The loading distribution on the blade could be one such parameter, as it is known that the loading distribution has an effect on the propeller noise emissions. To investigate this, as well as other notable effects inside the flowfield, a more detailed study into the measurements was conducted with the 7-hole probe. In this section, firstly, visualisations of the investigated velocity fields are shown. Secondly, some results used to indicate the spanwise loading of the propellers are shown. Finally, the tip vortex location is looked at in more detail in an effort to obtain more information about the slipstream width. Additional figures based on the flowfield measurements can be found in appendix D.

6.2.1. Full Flowfield

Figure 6.4a shows the normalised induced velocity u/U_∞ throughout the measured section of the flowfield. Only the effect of the propeller is included in these figures, as the nacelle-only results have been subtracted from the flowfields shown. The third row of the figure shows the difference between the induced velocities of XPROP-Λ and XPROP. Please note that, as with most flow visualisations, the flow goes from left to right.

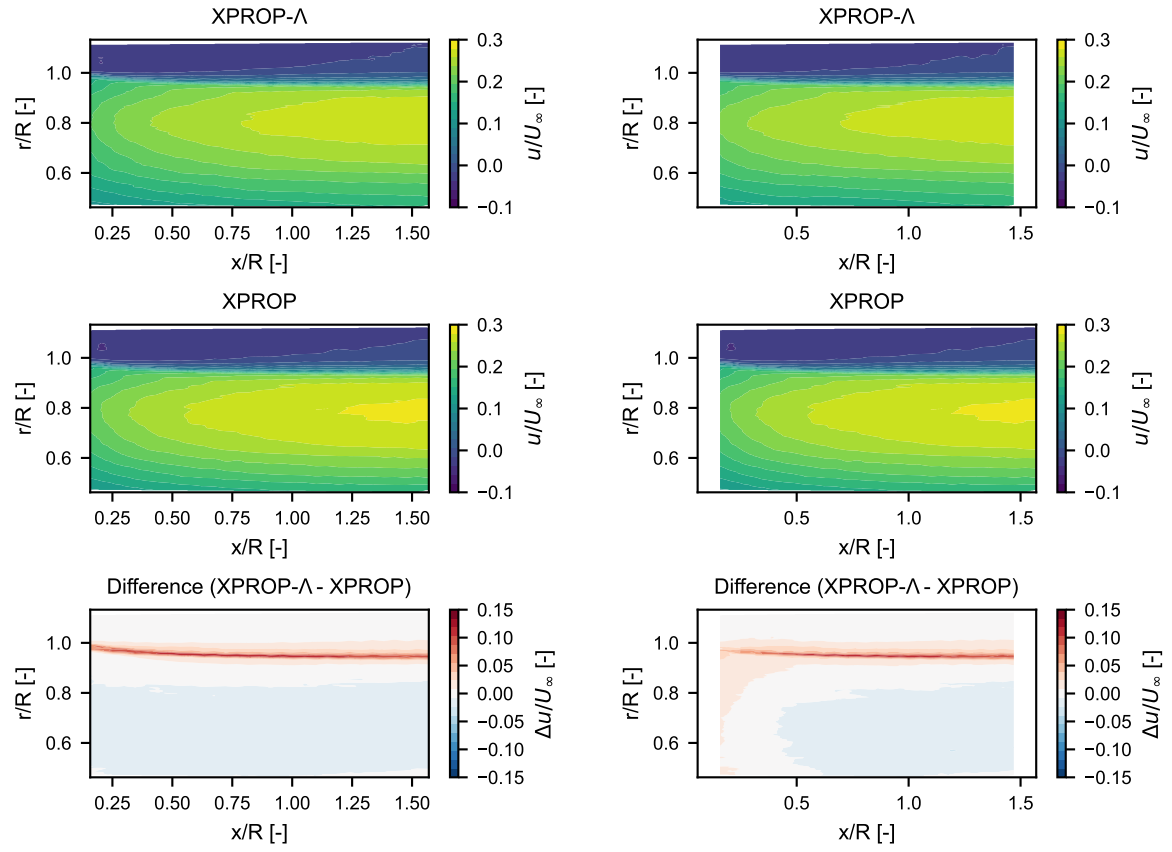

(a) No grid transformation applied

(b) XPROP-Λ data transposed forward by 20.32 mm

Figure 6.4: Normalised propeller induced axial velocity u/U_∞, at $\beta = 30°$. Axial positions from the mid chord of the propeller.

From figure 6.4a, it can be seen that, as expected, the slipstream contracts as one moves downstream from the propeller. Whilst this is the case for both propellers, some differences can also be observed: Firstly, it seems that the slipstream for XPROP-Λ has a lower mean velocity, indicated by the blue region in the delta plot. Secondly, it seems as though the slipstream for XPROP-Λ is wider, indicated by the red region on the outboard of the slipstream, showing higher velocities in this region.

Both these results indicate that there is a difference between the two slipstreams, both in terms of the velocity in the slipstream as well as the contraction. To further evaluate the contraction, it is relevant to investigate the path of the slipstream boundary. The tips of the two propellers are not in the same location, as stated before in chapter 3 and section 4.5. Whilst the contraction difference is likely an effect of the overall propeller loading, it should be ruled out that this tip location offset is the primary reason for the difference in induced velocity as shown in figure 6.4a. To isolate the tip offset effect, an offset is applied to the datasets of XPROP-Λ, resulting in figures 6.4b and D.3b. In these figures, it can be seen that the tip vortex still is positioned further outboard for XPROP-Λ. This shows that the change in the position of the tip vortex cannot only be attributed to the location of the propeller tip, but is an effect of the aerodynamics at play. To further investigate this, the spanwise loading distribution of the propeller and the path of the tip vortex were investigated further, as detailed in the next sections.

6.2.2. Spanwise Induced Velocities

Figures 6.5 and D.4 show the induced velocities from the propeller blades only, as for these figures, the nacelle-only measurements have been subtracted. From these figures, a number of things can be learned. Firstly, it can be seen that both sides of the wind tunnel show broadly similar velocity distributions for the two propellers, with and without the correction for the nacelle without a spinner. This indicates a low amount of asymmetry in the wind tunnel.

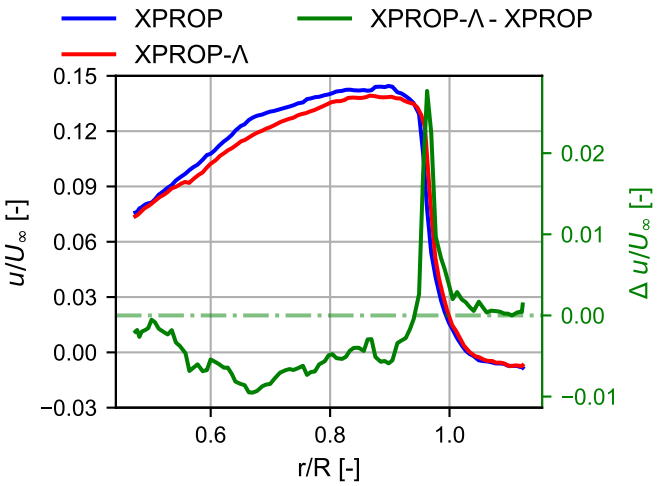

Figure 6.5: Spanwise distribution of propeller-induced axial velocity behind the propeller at $\beta = 45°$. Note that there are two different y-axis scales shown. Slice at an axial position of $x/R = 1.41$.

The other conclusions are primarily based on the differences between XPROP and XPROP-Λ, indicated with the green lines. Up to about $r/R = 0.98$, it can be seen that the induced velocities in the slipstream of XPROP-Λ are lower than for XPROP. Right at the boundary of the slipstream, there is a spike in the difference between the two, with afterwards a near-negligible difference outside the slipstream, where the flow is close to the freestream condition. This indicates that there is a shift in the outboard loading, likely caused by an increase in local angle of attack. Similarly, the inboard loading is reduced. This may also be related to the change in angle of attack due to the added blade sweep. This is explored further in section 7.2.

6.2.3. Slipstream Boundary Determination

Further details of the tracked vortex paths are shown in figures 6.6 and D.5. In these figures, the core paths on both sides of the workshop are shown, with the paths of XPROP-Λ shifted to account for their

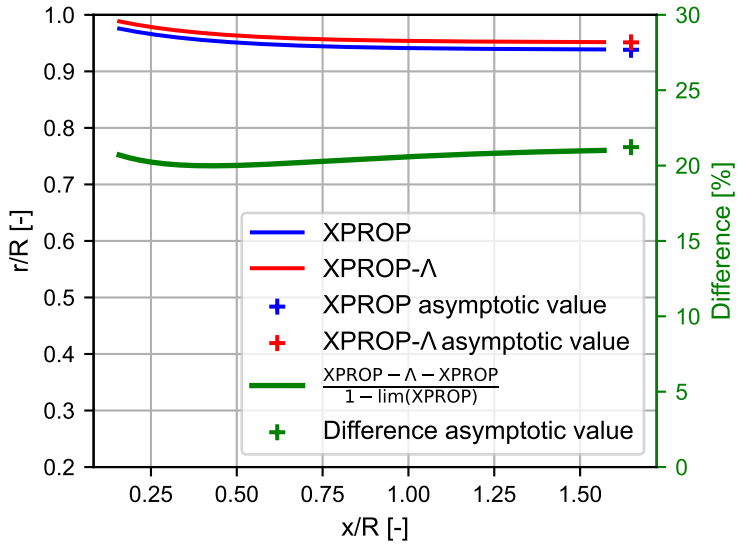

Figure 6.6: Comparison of tip vortex locations for $\beta = 30°$. With propeller-off data subtracted and with normalised axes.

tip positioning. In addition, the difference between the two is shown. This difference is normalised using the following equation:

$$\%\ \text{slipstream width difference} = \left(\frac{\text{XPROP-}\Lambda - \text{XPROP}}{1 - \lim_{\text{XPROP}}} \right) \cdot 100\% \tag{6.1}$$

Where all values on the right-hand side of the equation refer to the slipstream width of the two propellers, and $\lim_{\text{XPROP}}$ to the asymptotic value calculated for the slipstream width of XPROP. Thus, the difference between the slipstream width of the two propellers is expressed as a percentage of the contraction of XPROP. The R^2 values for the exponential fits are shown in table 4.4.

Figures 6.6 and D.5 show that there is a consistent offset in the location of the tip vortices shed between the unswept and swept blades, observed on both sides of the wind tunnel. The slipstreams are also close to converged to a constant width near the end of the measured flowfield. The computed offsets between XPROP and XPROP-Λ are presented in table 6.1. This shows that the slipstream contraction of XPROP-Λ is approximately 20% less than for XPROP.

Table 6.1: Difference in converged slipstream widths, expressed in percentages as per equation (6.1). Both measured maximum values and asymptotically determined values are presented.

Pitch [°]	Measured [%]	Asymptotic [%]
30	20.80	21.29
45	20.12	20.15

An actuator disk theory model was used to investigate the difference between the contraction ratios of the two propellers. This method is based solely on the thrust measured under the operating conditions for the flowfield measurements, and does not take the geometric differences into account. From this method, only a 1 to 2 % change in slipstream contraction is expected, significantly less than those measured. This shows that the change in thrust is not the main reason for the difference in slipstream shape between the two propellers, and that other factors, such as the spanwise loading distribution, are likely contributors as well.

7

Modelling Results

In this chapter, the experimental results shown in chapter 6 are compared with computational results computed using the methods described in chapter 5. The integral performance parameters are discussed in section 7.1, both in terms of replicating the measured values in the wind tunnel, and in terms of the effect of sweep. Afterwards, the spanwise distributions of circulation and angle of attack are discussed in section 7.2.

7.1. Integral Performance of Lifting-Line Methods

To investigate whether the various lifting-line methods (LLMs) can accurately replicate the wind tunnel results, both in terms of the effect of blade sweep and in terms of matching the measured performance, comparisons need to be made. Before such a comparison is made, it is useful to look at an example of a set of lifting-line results to obtain a reference for the relative differences. This can be found in figure 7.1.

Figure 7.1 shows both experimental results and lifting-line results, using the lift-based method and the NACA 4-series-based airfoil data. A non-linearity is visible in the lifting-line results, which can be attributed to non-linear airfoil data. It is noteworthy that the lifting-line results predict a larger difference between XPROP and XPROP-Λ than the experimental results suggest, for both pitch settings. Additionally, the predicted results from the lifting-line method are often outside the uncertainty margins of the experimental results. To investigate these preliminary findings in more detail, figures 7.2 to 7.4 are used.

One of the main questions of this thesis is whether or not the LLM can accurately determine the effect of sweep on a propeller. Figure 7.2 shows the difference between the swept and unswept blades at a pitch angle of 30°, for both lifting-line and experimental results. This figure shows whether the lifting-line results accurately predict the effect of the blade sweep of XPROP-Λ on the integrated performance, when comparing it with the experimental results.

From figure 7.2, interesting observations can be made. When looking at the thrust coefficient C_T, it is noticed that for the experimental data, XPROP-Λ has a lower C_T than XPROP for most of the advance ratio range, whereas the LLMs predict a higher thrust for XPROP-Λ than XPROP, except for the flow-tangency-based method with XPROP-based airfoil data. This combination of lifting-line parameters is also the only one that is almost within the uncertainty margin due to the manual pitch setting, indicating that this simulation most accurately determines the difference between XPROP and XPROP-Λ in terms of C_T. Furthermore, it is notable that the flow-tangency-based method shows a smaller change in C_T due to sweep than the lift-based method, and that XPROP-based airfoil data results in a smaller sweep effect than the NACA 4-series-based one. Finally, the lifting-line results all show a smaller effect of sweep at higher advance ratios, which in this case is the same as a low thrust setting.

Similar results can be drawn from the graph showing the $C_P$in figure 7.2. The combination of XPROP-based airfoil polars and the flow-tangency-based method predicts the smallest effect of sweep of the

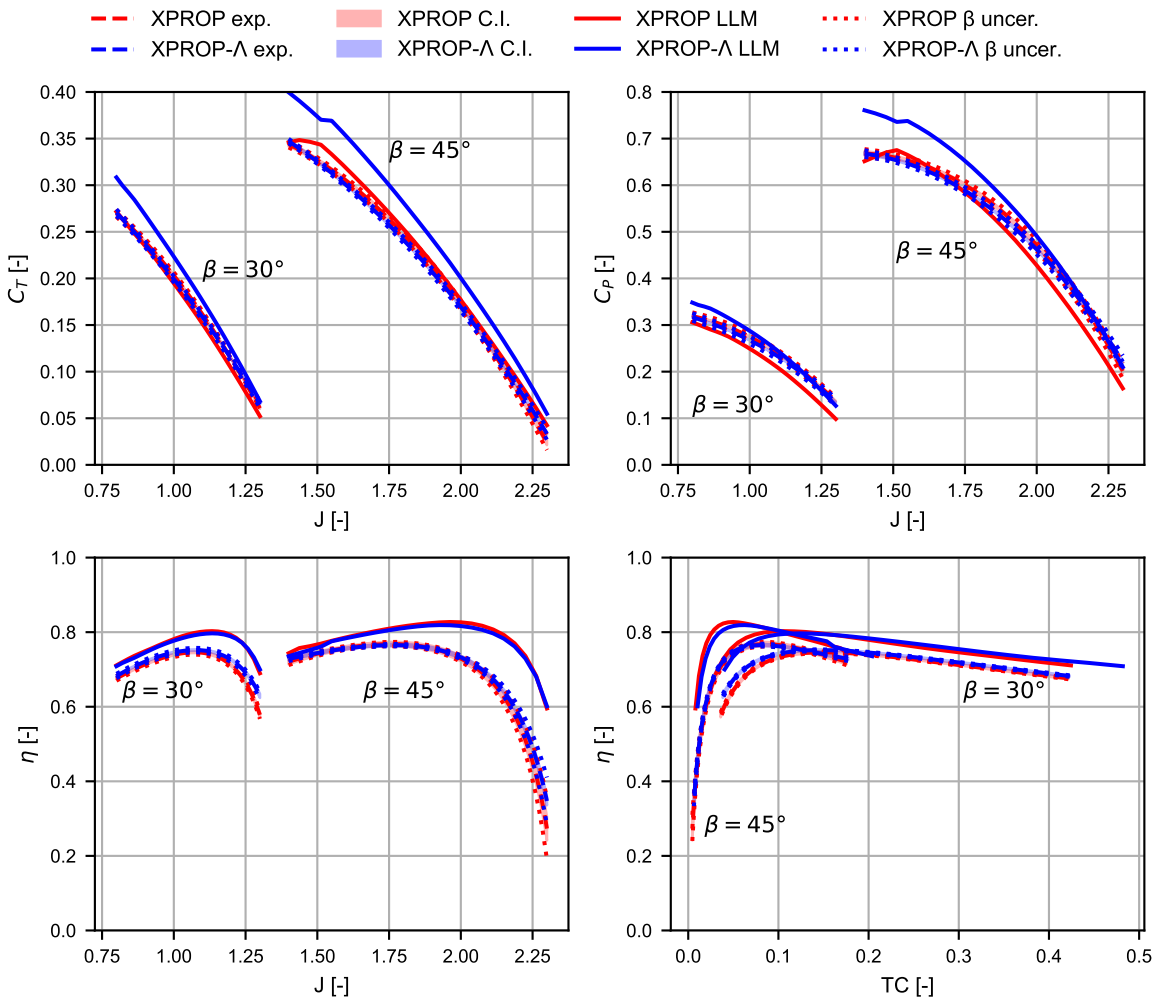

Figure 7.1: Performance parameters for experimental work and a lifting-line simulation. The lifting-line method used is the lift-based method, and the 2D airfoil polar source is NACA 4-series-based.

lifting-line methods, and is mostly within the uncertainty bands due to the pitch setting. Again, the flow-tangency-based method predicts a smaller effect due to the addition of sweep, and is therefore closer to the experimental results than the lift-based method. The XPROP-based airfoil data results in smaller changes in C_P due to the blade sweep than the NACA 4-series-based airfoil data.

The two efficiency plots show different results. The experimental results show a constant increase in efficiency over most of the tested conditions, with a clear increase in this difference at the highest advance ratios/lowest thrust settings investigated. Of the lifting-line results, only the lift-based method with NACA 4-series-based airfoil data shows similar behaviour, but at a constant offset and outside the uncertainty bands. Generally, the lift-based method with XPROP-based airfoil data is the closest to the experimental data in terms of predicting the effect of the sweep distribution on the efficiency. The lift-based method is generally more accurate in predicting the impact of sweep on the efficiency than the flow-tangency-based method. A similar figure to figure 7.2, but for $\beta = 45°$, is shown in appendix E in figure E.1.

The previous paragraphs discuss the effect of adding a sweep distribution to a propeller for the experimental results and the four lifting-line simulations. This is an important quantity for this thesis, but at least as important is whether the lifting-line predicts the same integrated performance as measured in the wind tunnel. To visualise this, the difference between the experimental data and the four different simulations is shown. This is shown for XPROP at a pitch of 30°in figure 7.3 and for XPROP-Λ at a pitch of 45° in figure 7.4, the other configurations can be found in appendix E. In figures 7.3 and 7.4,

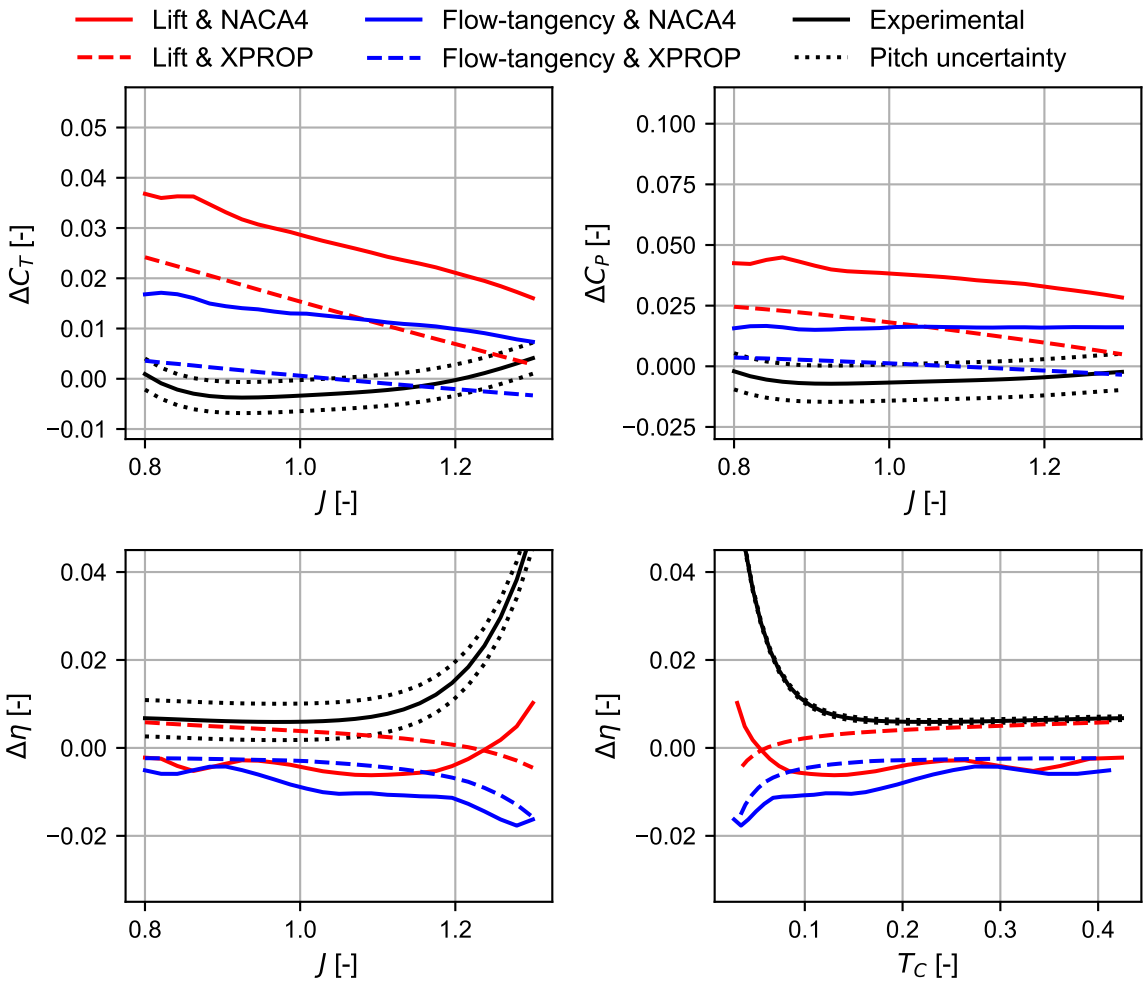

Figure 7.2: Difference between XPROP-Λ and XPROP at $\beta = 30°$, shown in C_T, C_P and η. Lines to indicate the uncertainty in the experimental results due to the manual pitch setting are included.

the uncertainty due to the manual pitch setting is included by showing error margins around the zero line.

From figures 7.3 and 7.4, information about the accuracy of the predicted C_T is obtained. First of all, both figures show that using the NACA 4-series-based airfoil data results in higher C_T values than the XPROP-based airfoil data. For XPROP at $\beta = 30°$, C_T is generally underpredicted by the lifting-line methods, but figure 7.4 shows that the opposite is the case for XPROP-Λ at $\beta = 45°$. Similarly, it is notable that the difference between the lifting-line and the experimental results is more constant when using the NACA 4-series-based airfoil data. It is also noteworthy that using the lift-based method results in higher predicted C_T than those computed using the flow-tangency-based method for both airfoil datasets.

When looking at the power coefficient, the story is much the same. The lift-based method gives higher values for C_P, which results in them being closer to the experimental results as seen in both figures 7.3 and 7.4. The lower C_P values when using the XPROP-based airfoil data can be explained by the lower drag coefficient C_d for these airfoils, due to the high Reynolds numbers used when determining the XPROP-based airfoil polars. The flow-tangency-based method underpredicts the power coefficient for all configurations investigated. The difference between the lift-based method and flow-tangency-based method becomes negligible at the highest advance ratios, which is to be expected as there is little thrust produced at these operating conditions (as shown in figure 6.1), resulting in near-zero power requirements.

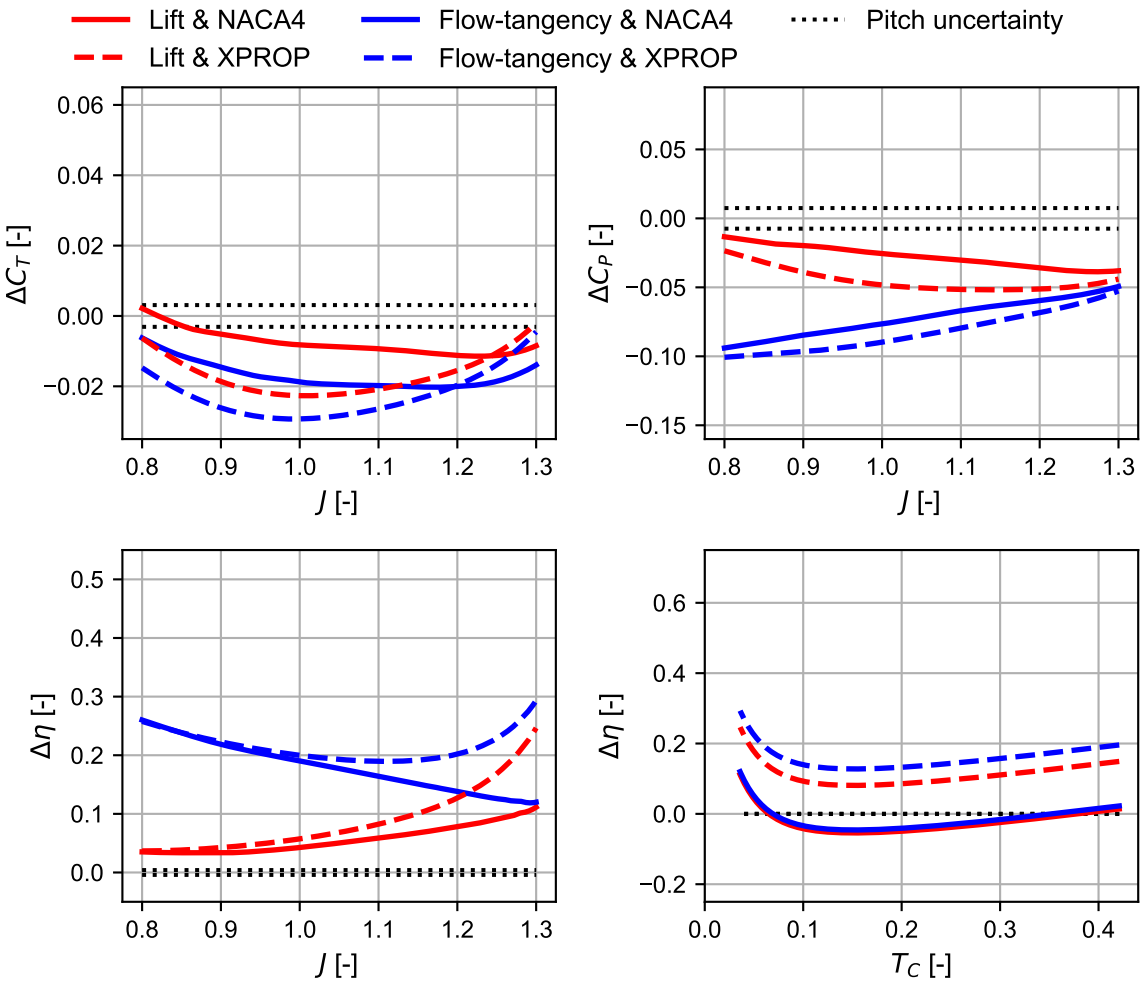

Figure 7.3: Difference between the lifting-line methods and experimental results, shown for XPROP at $\beta = 30°$. Uncertainty margins for the experimental results are included around zero. The difference is expressed as lifting-line − experimental.

Figures 7.3 and 7.4 contain two different ways in which the propulsor efficiency η is shown, from which various observations can be made. When visualising η with respect to the advance ratio, it can be seen that the lifting-line method used is the dominant factor when determining the efficiency, whereas the airfoil database source is much more crucial when evaluating the efficiency at equal thrust settings. The lift-based method is better at predicting the efficiency at equal advance ratio than the flow-tangency-based method. Based on figures 7.3 and 7.4, no such statement can be made when evaluating the efficiency at equal T_C, as the NACA 4-series based airfoil data gives better predictions for efficiency for XPROP at $\beta = 30°$, whereas the XPROP-based data gives better predictions for XPROP-Λ at $\beta = 45°$. Appendix E shows that this difference is an effect of the pitch, not of the propeller geometry.

It has become apparent that the combinations of lifting-line methods and airfoil database sources have different benefits and drawbacks. Using the flow-tangency-based method with the XPROP-based airfoil data reflects the effect of sweep seen in the wind tunnel experiment the best, but it is the worst in terms of replicating the wind tunnel results directly. Thus, it would be incorrect to state that this is an appropriate predictor of the swept and unswept blades, even if it does most accurately predict the difference between them.

Generally, the flow-tangency-based method is better at computing the effect of sweep on C_T and C_P, whereas it is not easily stated which of the two methods is best for determining the effect of sweep on the efficiency of the propeller. The flow-tangency-based method generally underpredicts the integrated loads of the propeller, especially the power coefficient. Using the NACA 4-series-based airfoil data

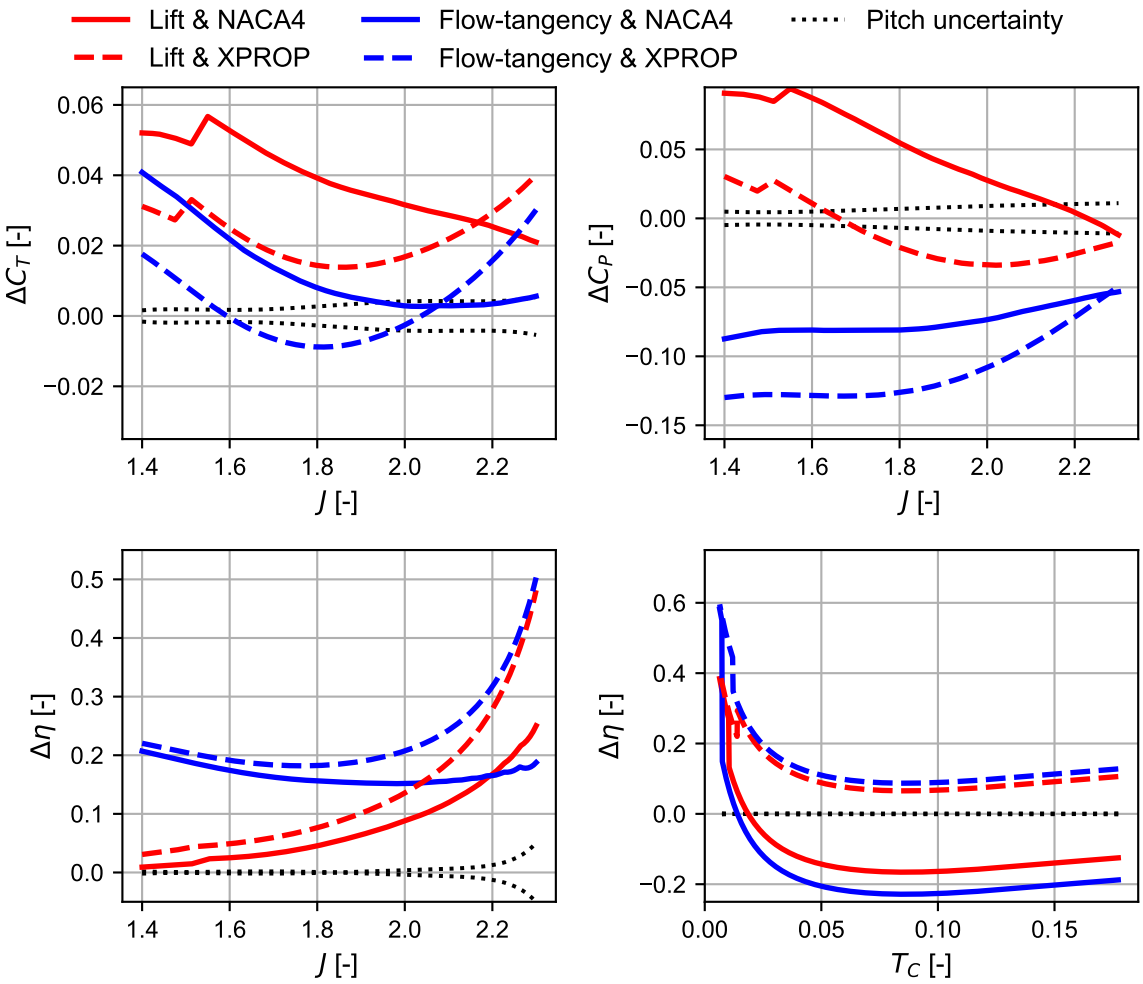

Figure 7.4: Difference between the lifting-line methods and experimental results, shown for XPROP-Λ at $\beta = 45°$. Uncertainty margins for the experimental results are included around zero. The difference is expressed as lifting-line − experimental.

generally results in the best efficiency predictions for constant advance ratio, but this is not necessarily reflected when evaluating the efficiency at constant T_C. The most important observation is that none of the combinations of the lifting-line method and airfoil database source is clearly the best, and that the lifting-line method in its current version is not necessarily well-suited to replicate the results seen in the wind tunnel, based on integrated performance. Another parameter of interest is the effect of sweep on the spanwise loading distribution, which is discussed in the next section.

7.2. Spanwise Distributions

Whilst it has been shown that the lifting-line methods are not suitable to predict the effect of added blade sweep consistently, it is still of interest to investigate if they are accurate in determining the effect on the spanwise loading distribution. The change in spanwise loading is one of the primary aerodynamic effects that adding a sweep angle to a propeller can have, as highlighted in section 2.4. This is further investigated in this section by analysing the spanwise circulation distribution, as computed by the LLM. This information cannot be directly compared to the experimental results, as no circulation distributions are obtainable from the available wind tunnel data. What can be learned from the wind tunnel results is that there is an outboard shift in loading, as discussed in section 6.2.2. An example of the circulation distributions obtained is shown in figure 7.5.

The spanwise circulation distribution is not a direct indication of the spanwise loading distribution, as the spanwise circulations induce velocities upon other parts of the blade, which change the local loads.

However, a local increase in circulation is still a useful indication of a shift in spanwise loading. However, the difference between the spanwise circulation distributions should not be expected to be as local as the change in induced velocity as determined by the wind tunnel experiments, as shown in figure 6.5.

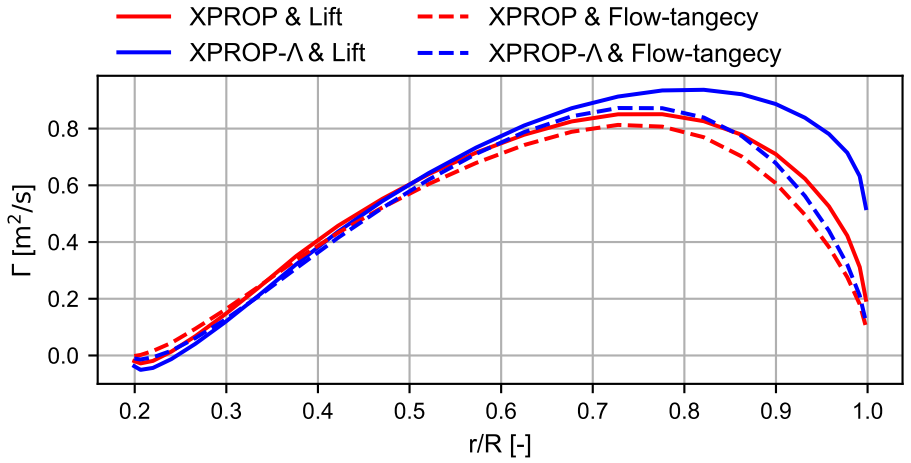

Figure 7.5: Spanwise circulation distribution for both propellers and lifting-line methods, using the NACA 4-series-based airfoil polar data. Results shown for $\beta = 30°$ at $J = 1.05$.

In figure 7.5, it can be seen that all lifting-line methods follow approximately the same trend in terms of circulation distribution up to $r/R = 0.6$, with the maximum circulation occurring between $r/R = 0.75$ and $r/R = 0.8$. When $r/R > 0.7$, the main differences between the methods become more pronounced.

The differences in the computed circulation distributions between XPROP-Λ and XPROP are shown in figure 7.6, as well as the difference in induced velocity as measured during the experiment, to evaluate the effect that sweep has on the spanwise circulation distribution.

Little difference between the models is observed near the blade root, with differences only starting to increase around halfway between the propeller rotation axis and the blade tip. The figure shows that the lift-based method gives a larger increase in outboard loading than the flow-tangency-based method, regardless of the airfoil database source. Using the NACA 4-series-based airfoil data results in a larger change in circulation than the XPROP-based airfoil data.

The lifting-line methods can also be used to determine the angle of attack on the propellers. An example of this is shown in figure 7.7. From this figure, it can be seen that XPROP-Λ has a lower angle of attack than XPROP on the inboard section of the blade, and that the angle of attack is higher on the outboard region. It can also be seen that the flow-tangency-based method results in higher local angles of attack than the lift-based method. Interestingly, these changes in angle of attack do not directly result in changes in the circulation, indicating that the locally induced velocities on the blade are also different. The change in local angle of attack and circulation is in line with the experimental results shown in figure 6.5.

This chapter has shown that the various lifting-line simulations have different strong and weak points, and that none of them individually are able to accurately determine the absolute values of C_T, C_P and η, and compute the difference between XPROP and XPROP-Λ. The differences in the spanwise distributions of circulation and angle of attack are also shown and discussed.

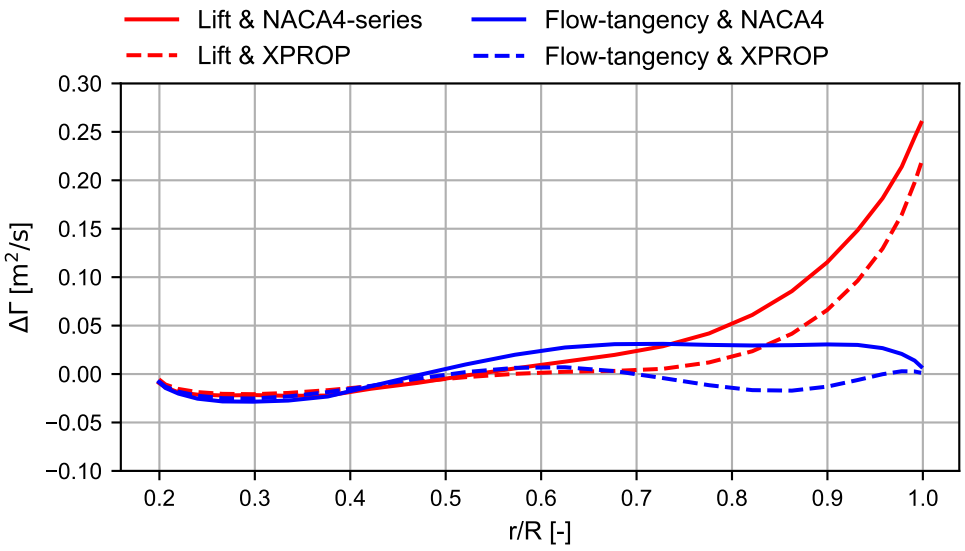

Figure 7.6: Effect of sweep on the spanwise circulation distribution for the different lifting-line simulations at $\beta = 45°$. The difference is defined as XPROP-Λ − XPROP.

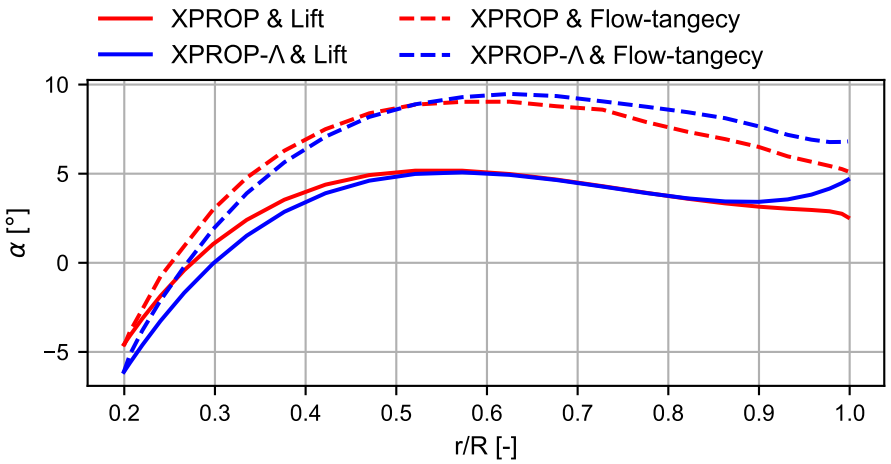

Figure 7.7: Spanwise angle of attack distribution for both propellers and lifting-line methods, using the NACA 4-series-based airfoil polar data. Results shown for $\beta = 30°$ at $J = 1.05$.

Part IV

Conclusion and Recommendations

8

Conclusion

The goal of this thesis was to investigate the effect of sweep on propellers and to learn if the lifting-line method is an appropriate tool for computing these effects. This chapter presents the answers obtained to the research questions posed in chapter 1, as well as other noteworthy findings and conclusions.

From the wind tunnel results, it was found that the difference between XPROP and XPROP-Λ in terms of the integrated performance is small. From the flowfield measurements, it was found that the slipstream contraction is approximately 20% less for XPROP-Λ. From the induced velocities in the slipstream, it can be seen that there is an outboard shift in the spanwise loading distribution due to the added sweep distribution. The induced velocity in the centre of the slipstream is reduced. The differences in slipstream contraction and induced velocity between the blades cannot simply be explained by the difference in overall loading, but are probably linked to the changes in the spanwise induction distribution. Please note that this is only valid for the low Mach number conditions investigated ($M_\infty < 0.12$, $M_{\text{tip}} < 0.5$), which means that compressibility effects are small, but that these results are still representative of the effect of sweep on the induction along the blade.

From the analysis of the experimental and computational results presented in this thesis, it is not possible to say if the lifting-line method is an appropriate tool for computing the effect of sweep on propeller blades. However, it can be stated that the combination of airfoil databases and lifting-line methods used is not accurate in predicting the outcome of the wind tunnel test. It is not possible to make a statement on the validity of the lifting-line tools when used to simulate propellers used on aircraft, due to the different Mach and Reynolds number regimes in these conditions.

The most important conclusion from the lifting-line analyses is the following: The effect of changing the lifting-line method between lift-based method and flow-tangency-based method, or changing the database between NACA 4-series based and XPROP based, has a substantially greater effect on the computational results than the change from XPROP to XPROP-Λ, as the effect of the blade sweep on the integrated performance is only small. Also, the lifting-line methods have different strengths and weaknesses. The lift-based method is better at approximating the measured integral performance values, but the flow-tangency-based method predicts the difference between XPROP and XPROP-Λ more accurately. Using the NACA 4-series-based airfoil data matches the wind tunnel results more closely than the XPROP-based data in terms of integrated performance, but worse at predicting the effect of adding blade sweep. Thus, it cannot be concluded that a single combination of the lifting-line method and airfoil polar data is the most appropriate tool to evaluate swept and unswept blades. The lift-based method also predicted a larger increase in circulation near the outboard of the propeller when blade sweep is added. This indicates a stronger increase in outboard loading for this method, although it is not possible to state if this is an accurate reflection of the wind tunnel data, with the data present.

Other works on lifting-line methods have compared the two formulations used in this thesis for swept wings. Chreim et al. [41] predicted that the flow-tangency-based method would be better-suited than the lift-based method when applied to complex flow cases such as those caused by propellers. From

the results of this thesis, no such conclusion can be drawn, as both methods have different strengths and weaknesses.

Within this thesis, it is shown that the effect of the blade sweep added to XPROP to create XPROP-Λ has nearly no effect on the integrated performance as measured in the wind tunnel. The lifting-line methods generally overestimate the effect of the blade sweep, as well as the propulsor efficiency. The flowfields measured in the wind tunnel showed some differences that are not solely attributable to the changes in loading from the added blade sweep, which opens the door to further research into this specific behaviour. This, and other recommendations, are discussed in the next chapter.

9

Recommendations

This chapter sets out to provide recommendations and advice for any future work in this area of research. These recommendations can be split into two parts: recommendations related to the experimental and the computational work.

A significant amount of the wind tunnel data analysis could not be conducted in the way that was originally planned, due to the problems with the reference data available. This could have been prevented if the processing scripts for the flowfield data had been available during the testing, such that the reference pressures for the flowfield without a propeller could have been visualised directly. Remeasuring the nacelle-only reference data would be beneficial to allow for further processing of the wind tunnel data. During these measurements, it is advised to process the flowfield measurements before finalising the test, to ensure that no problems have occurred.

The experiment conducted for this thesis was done at a combination of low Reynolds and Mach numbers. Therefore, the viscous and compressibility effects as seen in the wind tunnel differ from those seen in real-world applications of propellers. It would be interesting to repeat the experiment at higher Reynolds and Mach numbers to investigate whether the effect of sweep on the experimental results changes. The tip Mach number, which has not been investigated in this thesis, is another parameter of interest, as reducing the effective Mach number and therefore compressibility effects at the blade tips is one of the motivating factors for adding blade sweep. It would also be interesting to investigate the effectiveness of the lifting-line methods at these operating conditions.

The compressibility effects are also not consistently present in the lifting-line code used. There are two ways to implement these effects on the airfoil data: firstly, by applying a correction, such as the Prandtl-Glauert correction, to the incompressible airfoil data; secondly, by using airfoil data that has been computed at different Mach numbers, thus including compressibility effects directly. Currently, the NACA 4-series-based airfoil data is computed without compressibility effects, whereas the XPROP-based data is available at a range of Mach numbers. It would be best to have a consistent method of applying the compressibility effects.

One of the major limitations of the lifting-line method for this thesis is the quality of available 2D airfoil data. The NACA 4-series-based airfoil data is not an exact geometric representation, and the XPROP-based airfoil data does not cover the Reynolds number range that was investigated. Additionally, as outlined in the previous paragraph, the inclusion of compressibility effects is not consistent between the two polar sources. A possible way of improving the lifting-line results is to use a more appropriate set of airfoil data. Ideally, these would be polars based on the XPROP airfoils at the expected Reynolds and Mach numbers.

This thesis only investigates a single type of low-level aerodynamic modelling. A comparison between the lifting-line method and other low-level aerodynamic modelling techniques, such as the blade element method and vortex lattice method, would be a useful study to see if those methods are better at determining the effect of sweep.

Using other types of aerodynamic modelling could also provide further insight into the spanwise loading distribution. This information can be used to learn more about the slipstream contraction behaviour, which is of interest for applied cases of swept propellers, as the interaction between the propeller slipstream and other elements, such as aircraft wings or other rotors, will be different.

References

[1] L. L. M. Veldhuis. “Propeller Wing Aerodynamic Interference”. en. PhD. 2005. URL: https://repository.tudelft.nl/record/uuid:8ffbde9c-b483-40de-90e0-97095202fbe3 (visited on Mar. 26, 2025).

[2] R. Singh, G. Ameyugo, and F. Noppel. “Jet engine design drivers: past, present and future”. en. In: *Innovation in Aeronautics*. Elsevier, 2012, pp. 56–82. ISBN: 978-1-84569-550-7. DOI: 10.1533/9780857096098.1.56. (Visited on Jan. 5, 2025).

[3] G. D. J. van Dijk. “Propeller Blade Optimisation for Minimised Perceived Noise”. en. MSc thesis. Delft University of Technology, 2025. URL: https://repository.tudelft.nl/record/uuid:c0127e1b-6081-45a4-82fc-606c6eef2717 (visited on May 26, 2025).

[4] B. Magliozzi, D. Hanson, and R. Amiet. “Propeller and Propfan Noise”. In: *Aeroacoustics of Flight Vehicles: Theory and Practice* 1 (July 1991), pp. 1–64.

[5] J. Thielen. “Effects of Elasticity on Aeroacoustic Performance of Low-Noise Swept Propellers”. en. MSc thesis. Delft University of Technology, 2024. URL: https://repository.tudelft.nl/record/uuid:a29100e0-6234-480f-844d-2d9afce565c3 (visited on Jan. 5, 2025).

[6] S. Burger. “Multi-Fidelity Aerodynamic and Aeroacoustic Sensitivity Study of Isolated Propellers”. en. MSc thesis. Delft University of Technology, 2020. URL: https://repository.tudelft.nl/record/uuid:7abef8ee-c15c-4e36-ade6-33daa3262386 (visited on Jan. 5, 2025).

[7] G. Margalida, B. della Corte, T. Sinnige, K. Knepper, B. Soemarwoto, and R. Nahuis. “Low Fidelity Multidisciplinary Methodology for Efficient and Quiet Propeller Design: Numerical Investigation and Experimental Validation”. English. In: *30th AIAA/CEAS Aeroacoustics Conference (2024)*. 30th AIAA/CEAS Aeroacoustics Conference, 2024. 2024. DOI: 10.2514/6.2024-3317.

[8] G. Margalida. Private communication via email. Correspondence between December 2024 and July 2025.

[9] A. H. Epstein. “Aeropropulsion for commercial aviation in the twenty-first century and research directions needed”. In: *AIAA Journal* 52.5 (2014). Type: Article, pp. 901–911. DOI: 10.2514/1.J052713.

[10] R. R. Duivenvoorden. “Aerodynamic Phenomena of Propeller-Wing-Flap Interaction”. en. PhD. Delft: Delft University of Technology, 2025. URL: https://repository.tudelft.nl/record/uuid:1a705c0a-b0aa-4ddd-a350-8c663cf2fdb0 (visited on June 4, 2025).

[11] T. Sinnige. *Propeller Propulsion Aerodynamics - AE4130 Aircraft Aerodynamics Lecture 14*. English. Lecture Slides. Delft, Jan. 2024.

[12] H. H. Hubbard. *Aeroacoustics of flight vehicles : theory and practice. Vol. 1, Noise sources*. English. NASA reference publication; 1258; 90-3052. Section: 592 blz. ; .. cm. Woodbury: American Institute of Physics, 1995. ISBN: 1-56396-404-X.

[13] D. B. Hanson. “Influence of Propeller Design Parameters on Far-Field Harmonic Noise in Forward Flight”. In: *AIAA Journal* 18.11 (1980), pp. 1313–1319. DOI: 10.2514/3.50887.

[14] Delft University of Technology. *Propeller models*. URL: https://www.tudelft.nl/en/ae/organisation/departments/flow-physics-and-technology/flight-performance-propulsion/flight-performance/propeller-aerodynamics/facilities/propeller-models (visited on Jan. 9, 2025).

[15] J. D. Anderson, Jr. *Fundamentals of Aerodynamics*. 6th ed. Columbus, OH: McGraw-Hill Education, 2017. ISBN: 978-1-259-25134-4.

[16] A. J. Evans and G. Liner. *A Wind-tunnel Investigation of the Aerodynamic Characteristics of a Full-scale Sweptback Propeller and Two Related Straight Propellers*. NTRS Author Affiliations: NTRS Report/Patent Number: NACA-RM-L50J05 NTRS Document ID: 19930090397 NTRS Research Center: Legacy CDMS (CDMS). Jan. 1951. URL: https://ntrs.nasa.gov/citations/19930090397 (visited on Apr. 14, 2025).

[17] J. P. Sullivan. "The Effect of Blade Sweep on Propeller Performance". In: June 1977.

[18] D. Melpignano. "Effects of the Unsteady Blade Loading on the Aero-Acoustic Performance of a Boundary Layer Ingesting Propeller". en. MSc thesis. Delft University of Technology, 2024. URL: https://repository.tudelft.nl/record/uuid:2cc7b9f7-b995-49e4-8781-8a95045862d3 (visited on Jan. 16, 2025).

[19] N. van Arnhem. "Unconventional Propeller−Airframe Integration for Transport Aircraft Configurations". en. ISBN: 978-94-6384-305-8. PhD. Delft University of Technology, 2022. URL: https://doi.org/10.4233/uuid:4d47b0db-1e6a-4f38-af95-aafd33c29402 (visited on Jan. 5, 2025).

[20] T. Stokkermans. "Aerodynamics of Propellers in Interaction Dominated Flowfields". en. ISBN: 978-94-6366-332-8. PhD Thesis. Delft University of Technology, 2020. URL: https://doi.org/10.4233/uuid:46178824-bb80-4247-83f1-dc8a9ca7d8e3 (visited on June 4, 2025).

[21] T. Sinnige. *Engine Integration - AE4115 Experimental Simulations Lecture 11*. English. Lecture Slides. Delft, Dec. 2023.

[22] J. B. Barlow, W. H. Rae, Jr., and A. Pope. *Low-Speed Wind Tunnel Testing*. English. 3rd ed. Wiley-Intersciency, Feb. 1999. ISBN: 0-471-55774-9.

[23] G. Eitelberg. *AE4115: Experimental Simulations Reader*. May 2021.

[24] T. Sinnige. *Wind-Tunnel Boundary Corrections*. Lecture Slides. Delft, Dec. 2023.

[25] N. van Arnhem, R. Vos, and L. L. M. Veldhuis. "Aerodynamic Loads on an Aft-Mounted Propeller Induced by the Wing Wake". In: *AIAA Scitech 2019 Forum*. Jan. 2019. DOI: 10.2514/6.2019-1093.

[26] M. Drela and H. Youngren. *XFOIL 6.99*. 2013. URL: https://web.mit.edu/drela/Public/web/xfoil/.

[27] J. Serpieri. "Cross-Flow Instability: Flow diagnostics and control of swept wing boundary layers". en. PhD Thesis. Delft: Delft University of Technology, Mar. 2018. DOI: 10.4233/uuid:3dac1e78-fcc3-437f-9579-048b74439f55.

[28] R. Nederlof, D. Ragni, and T. Sinnige. "Experimental Investigation of the Aerodynamic Performance of a Propeller at Positive and Negative Thrust and Power". English. In: *AIAA AVIATION 2022 Forum*. AIAA AVIATION 2022 Forum. United States: American Institute of Aeronautics and Astronautics Inc. (AIAA), 2022. DOI: 10.2514/6.2022-3893.

[29] T. Sinnige. Private communication via email. Email received in June 2025.

[30] Surrey Sensors Ltd. *Digital seven-hole probe system*. en-GB. 2025. URL: https://www.surreysensors.com/products/digital-seven-hole-probe-system/ (visited on Apr. 27, 2025).

[31] N. van Luijk and R. Vos. "Experimental Investigation of Vortex Flow Over a Flying V Subsonic Transport". In: *AIAA SCITECH 2025 Forum*. Orlando, Florida, Jan. 2025. DOI: 10.2514/6.2025-0258.

[32] R. R. Duivenvoorden, T. Sinnige, and L. L. M. Veldhuis. "Impact of Helix Characteristics on Slipstream Deformation in Propeller–Wing–Flap Interaction". In: *AIAA Journal* (July 2025), pp. 1–20. ISSN: 0001-1452. DOI: 10.2514/1.J064763. (Visited on July 27, 2025).

[33] S. Shaw-Ward, A. Titchmarsh, and D. M. Birch. "Calibration and Use of n-Hole Velocity Probes". In: *AIAA Journal* 53.2 (2015), pp. 336–346. DOI: 10.2514/1.J053130.

[34] O. Wright and W. Wright. "The Wright Brothers' Aeroplane". In: *The Century Magazine* 76.5 (Sept. 1908), pp. 641–650. URL: https://digital.lib.ecu.edu/encore/ncgre000/00000037/00036710/00036710.pdf.

[35] J. Weissinger. *The Lift Distribution of Swept-Back Wings*. Tech. rep. NACA-TM-1120. NTRS Author Affiliations: National Advisory Committee for Aeronautics. Langley Aeronautical Lab. NTRS Document ID: 20030064148 NTRS Research Center: Langley Research Center (LaRC). Mar. 1947. URL: https://ntrs.nasa.gov/citations/20030064148 (visited on Mar. 24, 2025).

[36] J. C. Sivells and R. H. Neely. *Method for calculating wing characteristics by lifting-line theory using nonlinear section lift data*. Tech. rep. NTRS Author Affiliations: NTRS Report/Patent Number: NACA-TR-865 NTRS Document ID: 19930091938 NTRS Research Center: Legacy CDMS (CDMS). Jan. 1947. URL: https://ntrs.nasa.gov/citations/19930091938 (visited on July 23, 2025).

[37] J. D. Anderson, Jr., S. Corda, and D. Wie. "Numerical lifting line theory applied to drooped leading-edge wings below and above stall". In: *Journal of Aircraft* 17 (Dec. 1980). DOI: 10.2514/3.44690.

[38] W. F. Phillips and D. O. Snyder. "Modern Adaptation of Prandtl's Classic Lifting-Line Theory". In: *Journal of Aircraft* 37.4 (2000), pp. 662–670. DOI: 10.2514/2.2649.

[39] D. Hunsaker. "A Numerical Lifting-Line Method Using Horseshoe Vortex Sheets". In: *Utah Space Grant Consortium* (May 2011). URL: https://digitalcommons.usu.edu/spacegrant/2011/Session1/4.

[40] J. R. Chreim, F. R. Esteves, M. d. M. Pimenta, G. R. S. Assi, J. L. D. Dantas, and A. M. Kogishi. "Validation of a Novel Lifting-Line Method for Propeller Design and Analysis". In: *Practical Design of Ships and Other Floating Structures*. Ed. by T. Okada, K. Suzuki, and Y. Kawamura. Singapore: Springer Singapore, 2021, pp. 616–635. ISBN: 978-981-15-4624-2.

[41] J. R. Chreim, J. L. D. Dantas, K. P. Burr, G. R. S. Assi, and M. M. Pimenta. "Verification & validation of lifting line α- and Γ-formulations for 3-D planforms under viscous flows". In: *The Aeronautical Journal* 127.1314 (2023), pp. 1473–1490. DOI: 10.1017/aer.2023.9.

[42] J. Katz and A. Plotkin. *Low-Speed Aerodynamics*. 2nd ed. Cambridge Aerospace Series. Cambridge University Press, 2001. ISBN: 0-521-66219-2.

[43] Ansys. *Ansys Fluent | Fluid Simulation Software*. en-US. URL: https://www.ansys.com/products/fluids/ansys-fluent (visited on July 11, 2025).

[44] NASA. *NACA Airfoils - NASA*. en-US. URL: https://www.nasa.gov/image-article/naca-airfoils/ (visited on July 14, 2025).

[45] Airfoil Tools. *NACA 4 digit airfoil generator (NACA 2412 AIRFOIL)*. URL: http://airfoiltools.com/airfoil/naca4digit (visited on July 14, 2025).

[46] J. van Ingen. "The eN Method for Transition Prediction. Historical Review of Work at TU Delft". In: *38th Fluid Dynamics Conference and Exhibit*. Fluid Dynamics and Co-located Conferences. American Institute of Aeronautics and Astronautics, June 2008. DOI: 10.2514/6.2008-3830. (Visited on Aug. 24, 2025).

[47] E. Langedijk. Private communication via email. Email received in April 2025.

A

XPROP-Λ Airfoil Trailing Edge Adjustments

This appendix shows the effects of increasing the trailing edge thickness of XPROP-Λ to ensure that it is always a minimum of 0.2 mm. All results have been obtained using XFOIL [26], conducted at the Reynolds number expected at the provided radial position at an advance ratio of 0.8 and a freestream Mach number of 0.12. The normalised trailing edge thickness is shown in figure A.1. The airfoils outboard of $r/R = 0.755$ have been modified. The effect of these modifications on the airfoil polars can be seen in figures A.3 to A.10, which shows that the effect of these modifications is small when the airfoil is not stalled. The calculations shown in these figures were done at Reynolds numbers representative of a case where $J = 0.8$ and $M = 0.12$. The shape change of the airfoil at $r/R = 1$ is shown in figure A.2, to provide an example of the magnitude of shape change required. This airfoil is also the airfoil with the shape change of the largest magnitude, as seen in figure A.1.

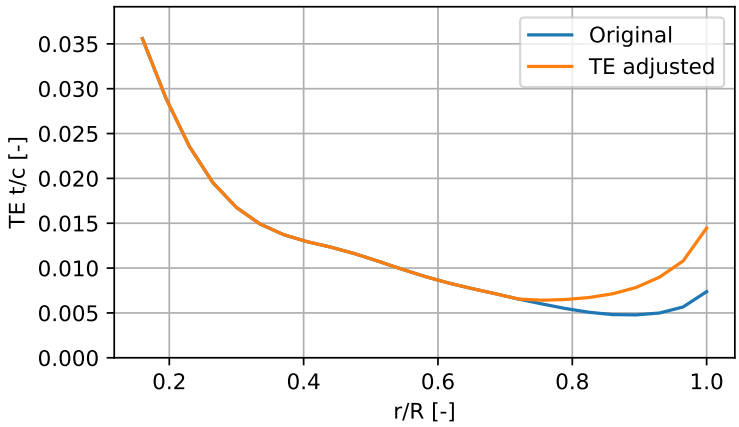

Figure A.1: Normalised trailing edge thickness distribution comparison.

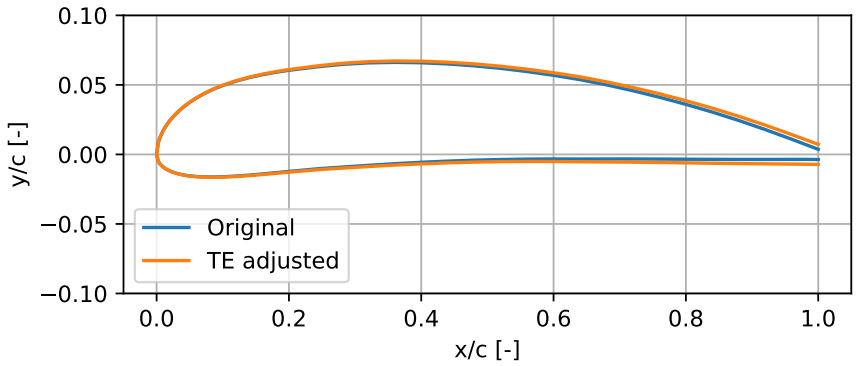

Figure A.2: Change in airfoil shape due to TE thickness adjustments, at $r/R = 1$.

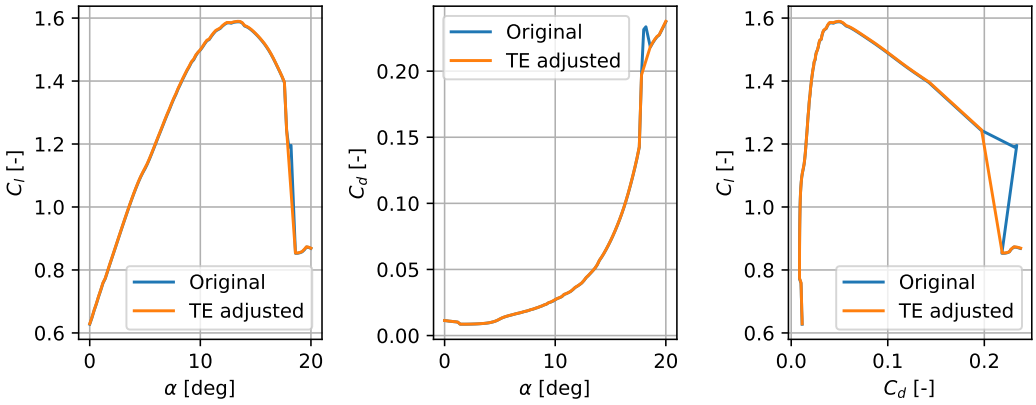

Figure A.3: Effect of TE adjustment at r/R = 0.755.

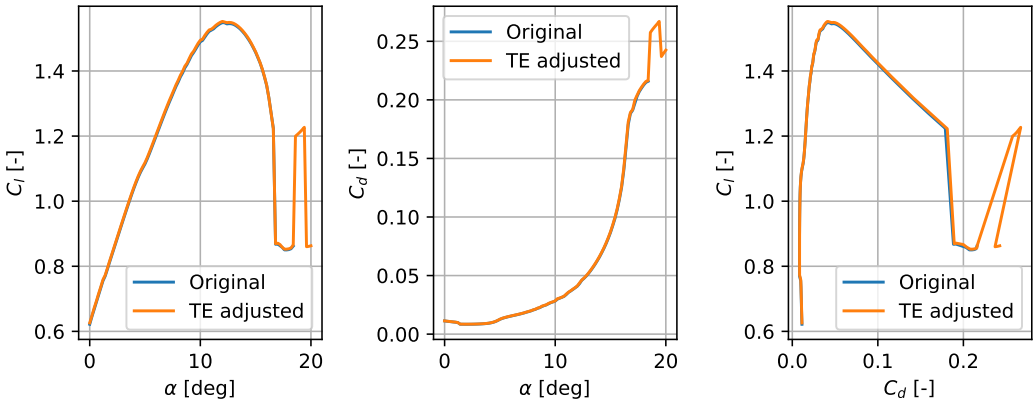

Figure A.4: Effect of TE adjustment at r/R = 0.790.

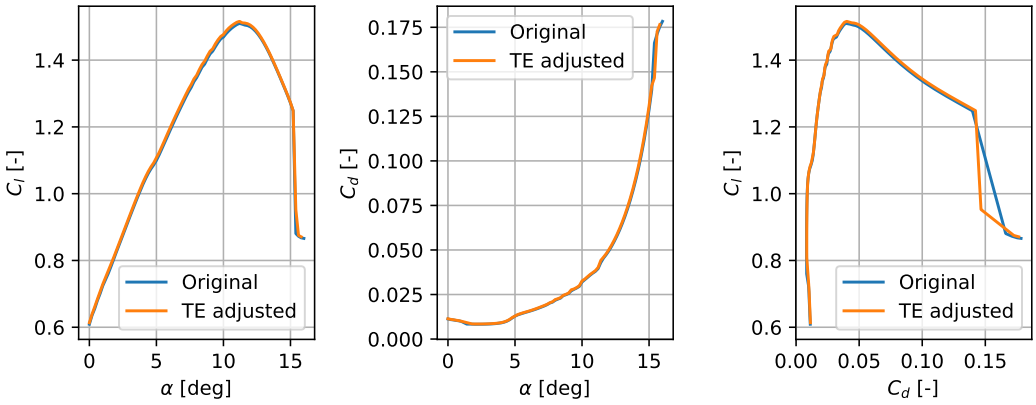

Figure A.5: Effect of TE adjustment at r/R = 0.825.

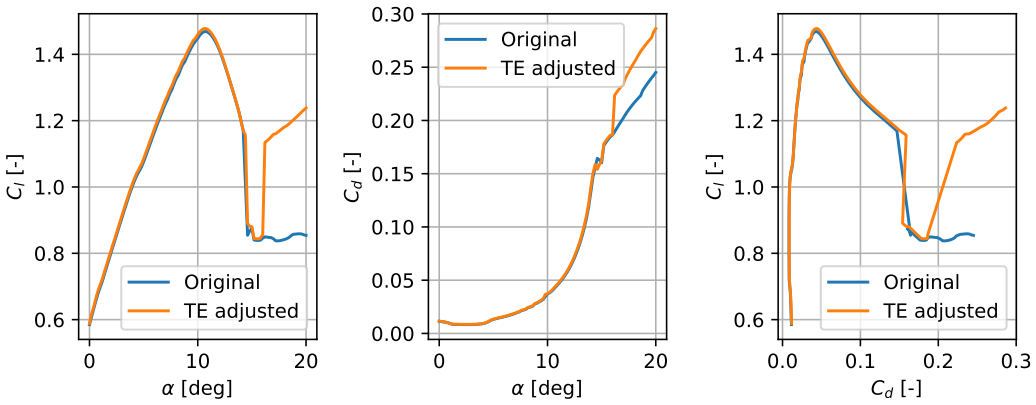

Figure A.6: Effect of TE adjustment at r/R = 0.860.

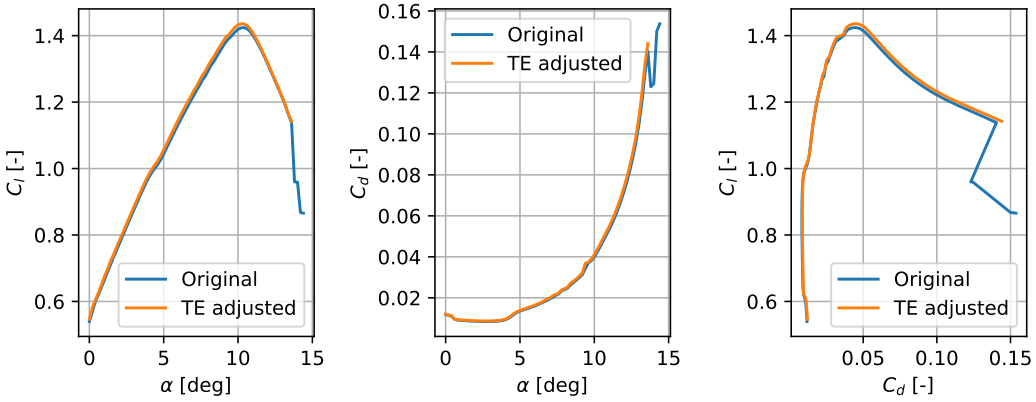

Figure A.7: Effect of TE adjustment at r/R = 0.895.

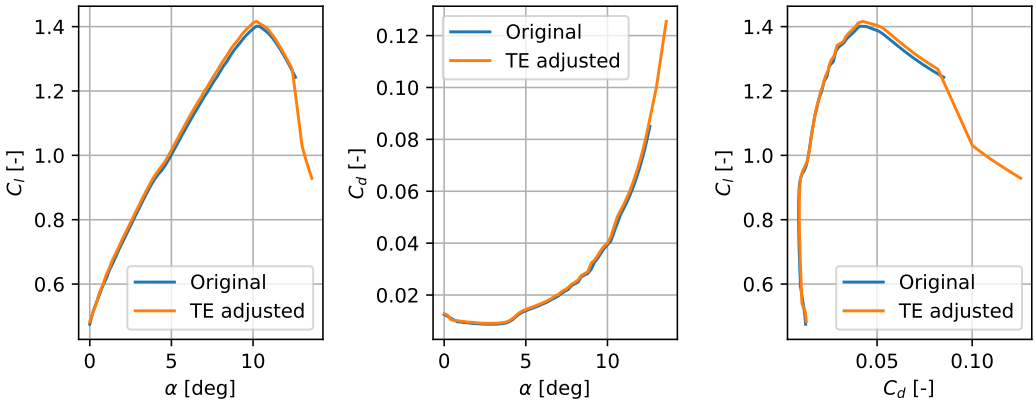

Figure A.8: Effect of TE adjustment at r/R = 0.930.

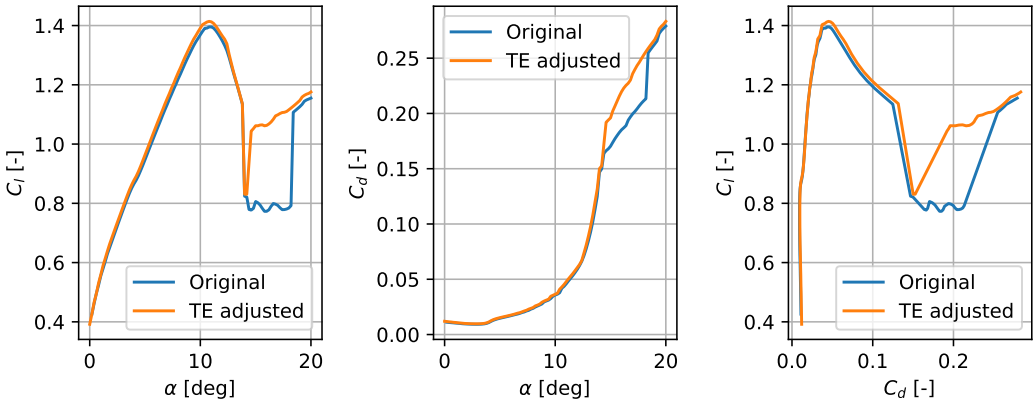

Figure A.9: Effect of TE adjustment at r/R = 0.965.

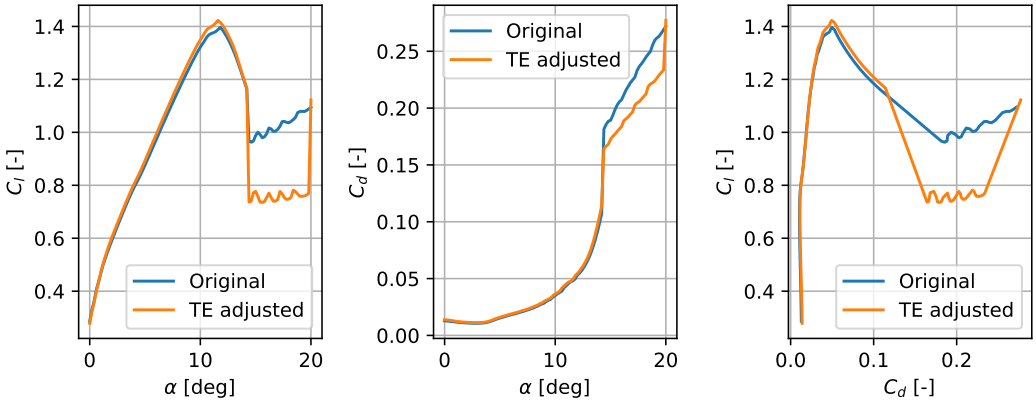

Figure A.10: Effect of TE adjustment at r/R = 1.

B

Schematic Drawing of the LTT

This appendix contains a schematic drawing of the low turbulence tunnel.

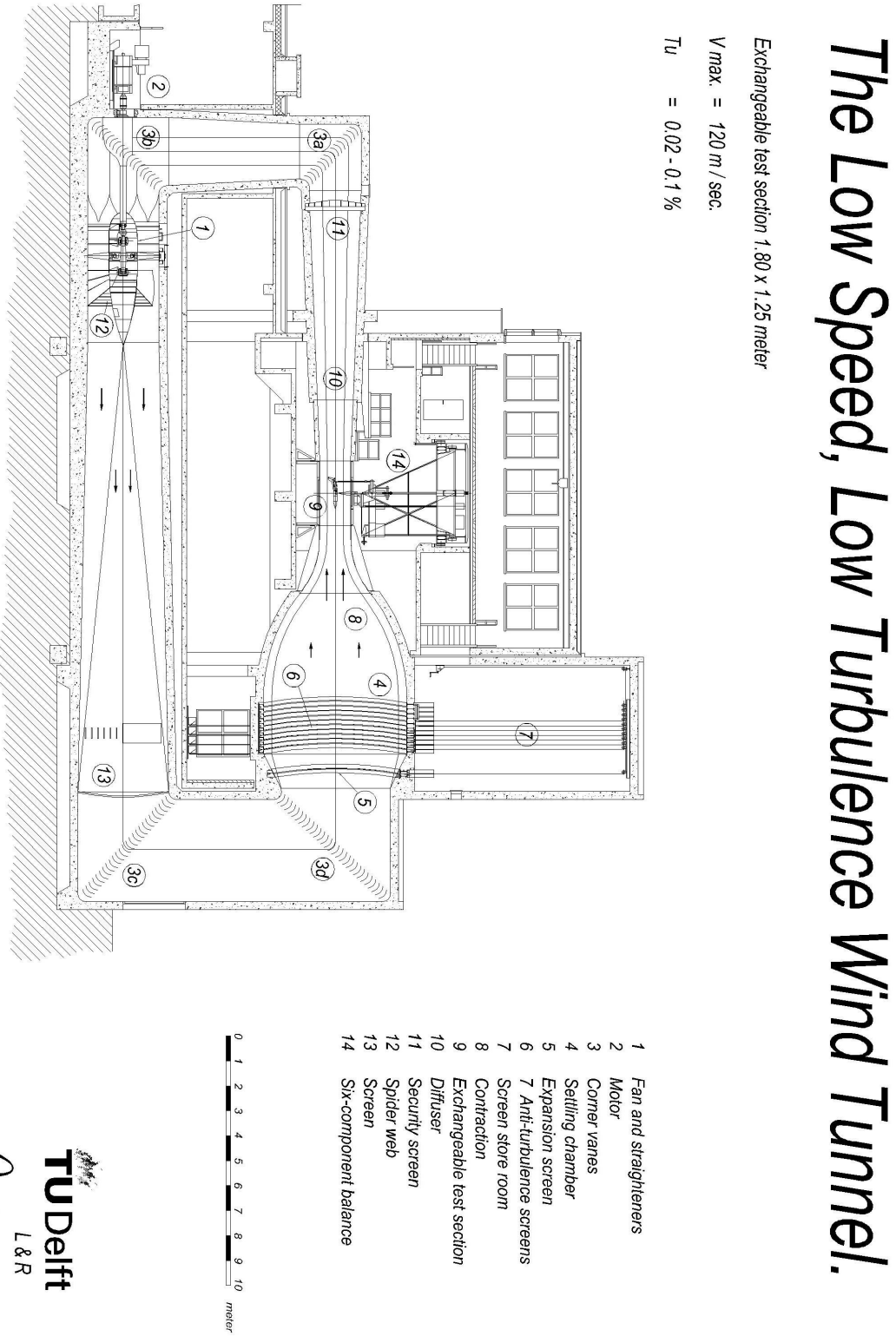

Figure B.1: Schematic of the Low Speed, Low Turbulence Wind Tunnel. From Langedijk [47, private communication].

C

Blockage Effects

Section 4.4.1 explains how the walls of a wind tunnel influence the flow in a closed test-section by altering the freestream velocity, and therefore advance ratio. This appendix presents an overview of the effect of the wind tunnel boundary corrections. The conditions shown in figures C.1 and C.2 are XPROP at 30° pitch and XPROP-Λ at 45°respectively, both at M = 0.12.

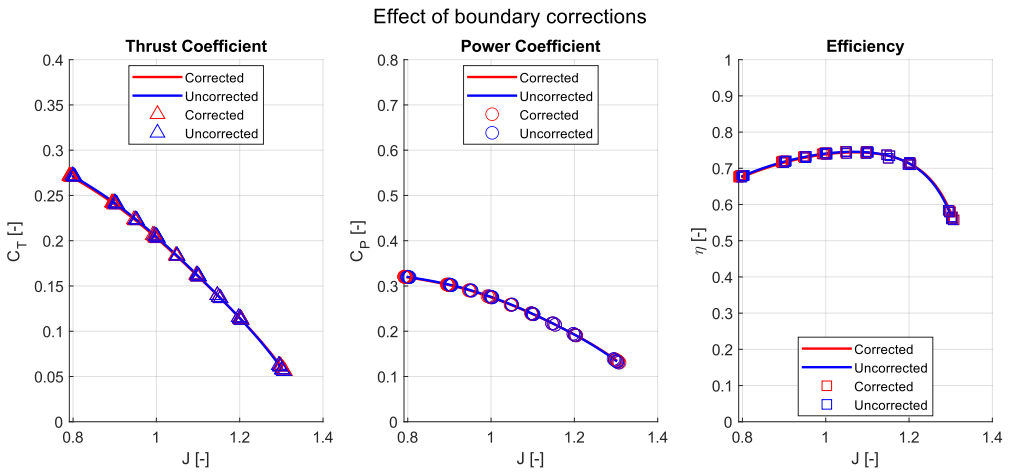

Figure C.1: Comparison of corrected and uncorrected performance data for XPROP at a pitch angle of 30° and a Mach number of 0.12.

The figures provided an indication that the effect of the boundary corrections is small, which can be quantified. Table C.1 shows the extremes of the advance ratio ranges examined during the wind tunnel test. It shows that the largest change in advance ratio due to the boundary corrections is less than 1%. Furthermore, it also shows that the minimal values for J are reduced, whilst the maximum values are increased. The solid blockage coefficient is positive, whereas the slipstream blockage coefficient is negative. A positive overall correction coefficient results in an increase in corrected J, whereas a negative one does the opposite, as shown in equation (4.1). The change from negative to positive differences indicates that the magnitude of the slipstream blockage coefficient is smaller than the solid blockage coefficient for a subset of the tested conditions.

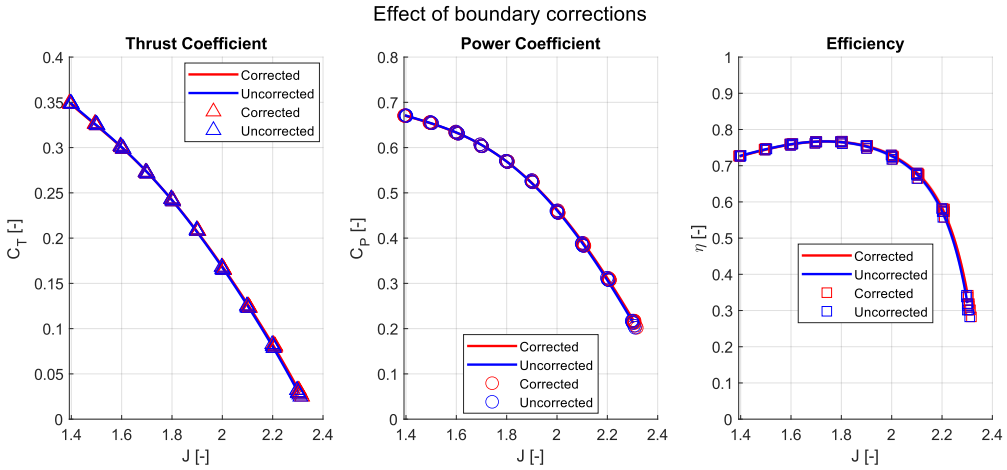

Figure C.2: Comparison of corrected and uncorrected performance data for XPROP-Λ at a pitch angle of 45° and a Mach number of 0.12.

Table C.1: Advance ratio (J) range comparison with and without correction.

Pitch Angle [°]	Condition	Uncorrected	Corrected	Difference [%]
45	Min J	1.396	1.392	−0.272 %
	Max J	2.310	2.317	+0.302 %
30	Min J	0.798	0.791	−0.858 %
	Max J	1.306	1.308	+0.195 %

D

Additional Experimental Results

This appendix contains figures that were obtained from the experimental results, which can be viewed in addition to those shown in chapter 6.

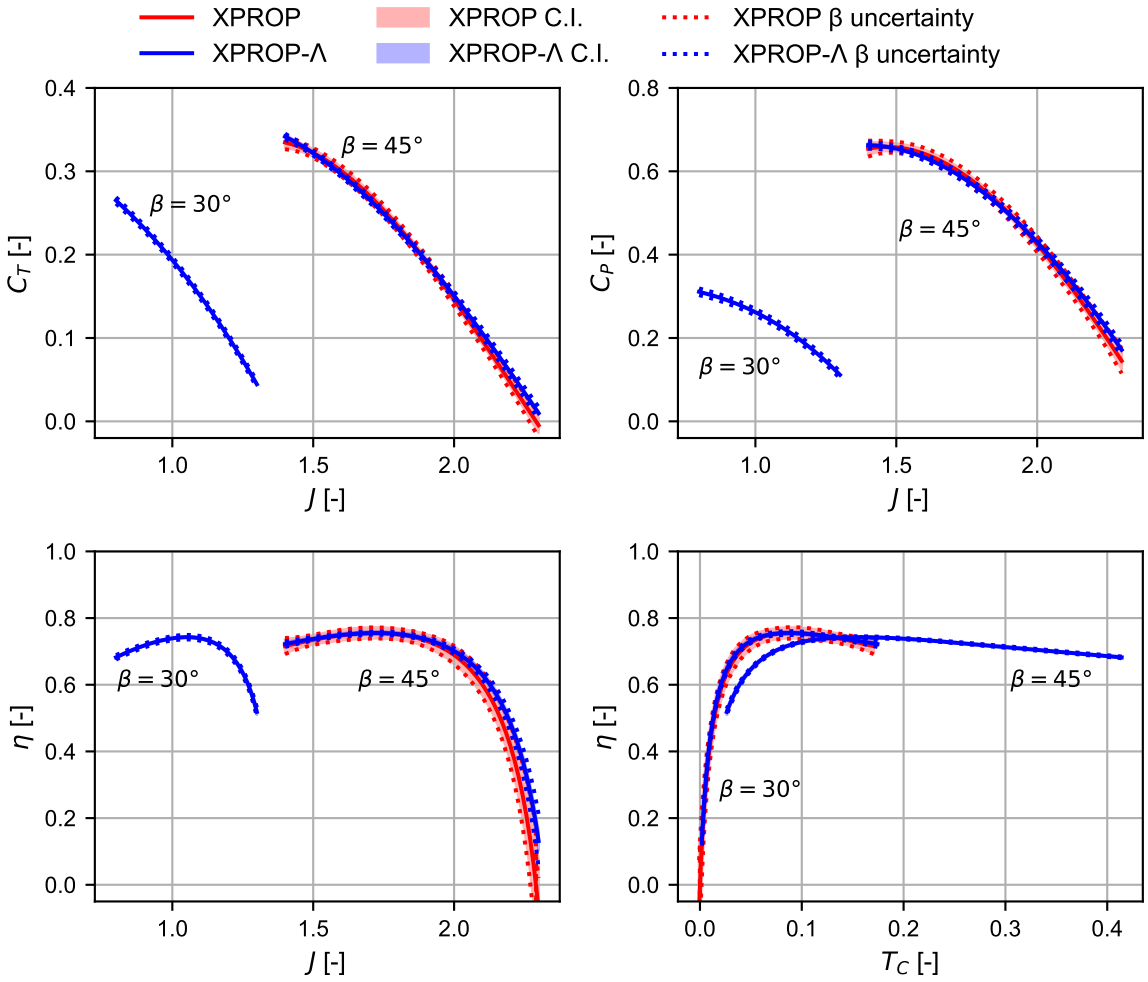

Figure D.1: Performance curves from wind tunnel measurements, for $\beta = 30°$ and $\beta = 45°$ at $M = 0.09$. Includes 95% confidence intervals as well as the effect of pitch angle uncertainty.

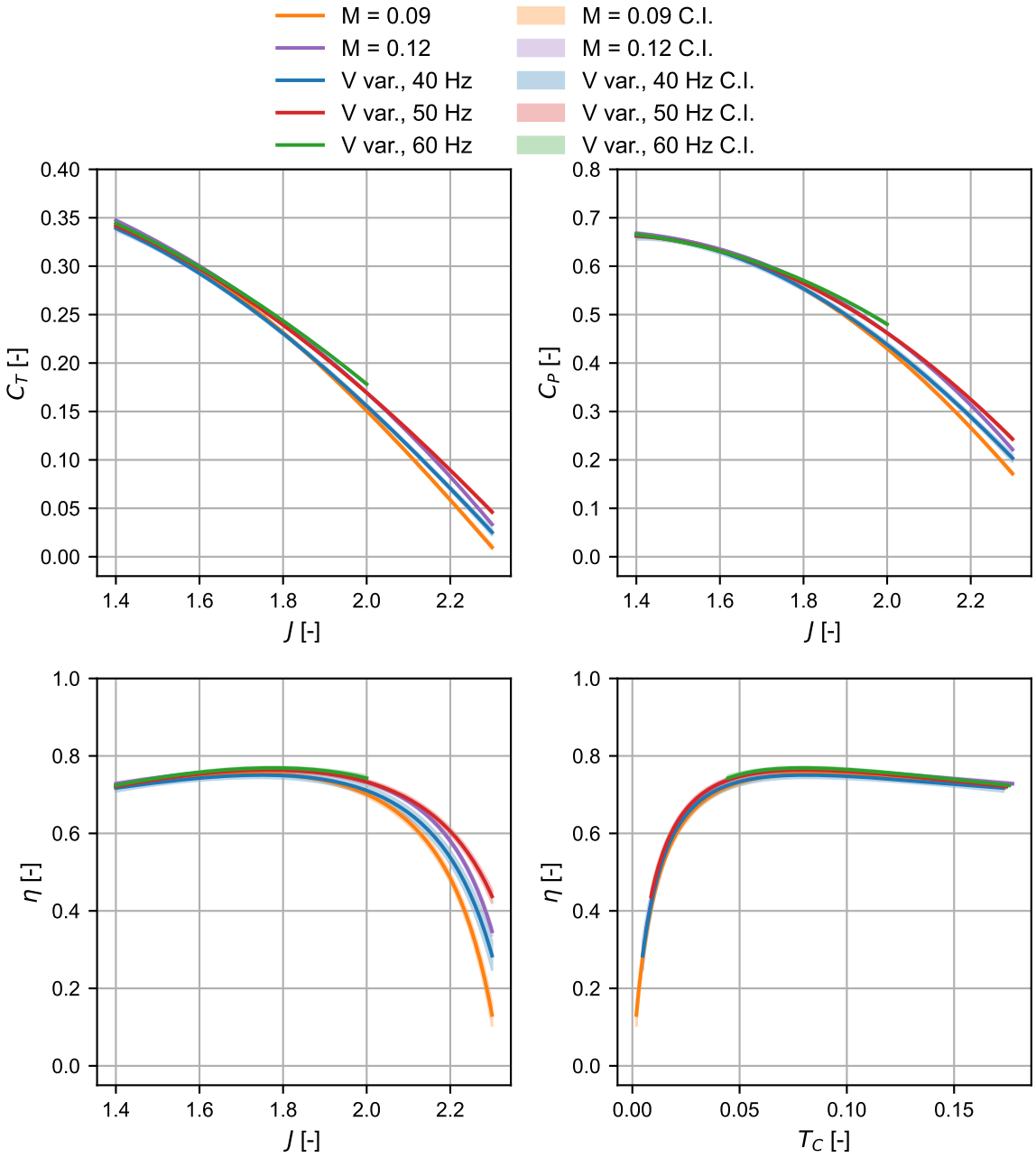

Figure D.2: Overview of measured results for XPROP-Λ at $\beta = 45°$, for the five different measurement conditions.

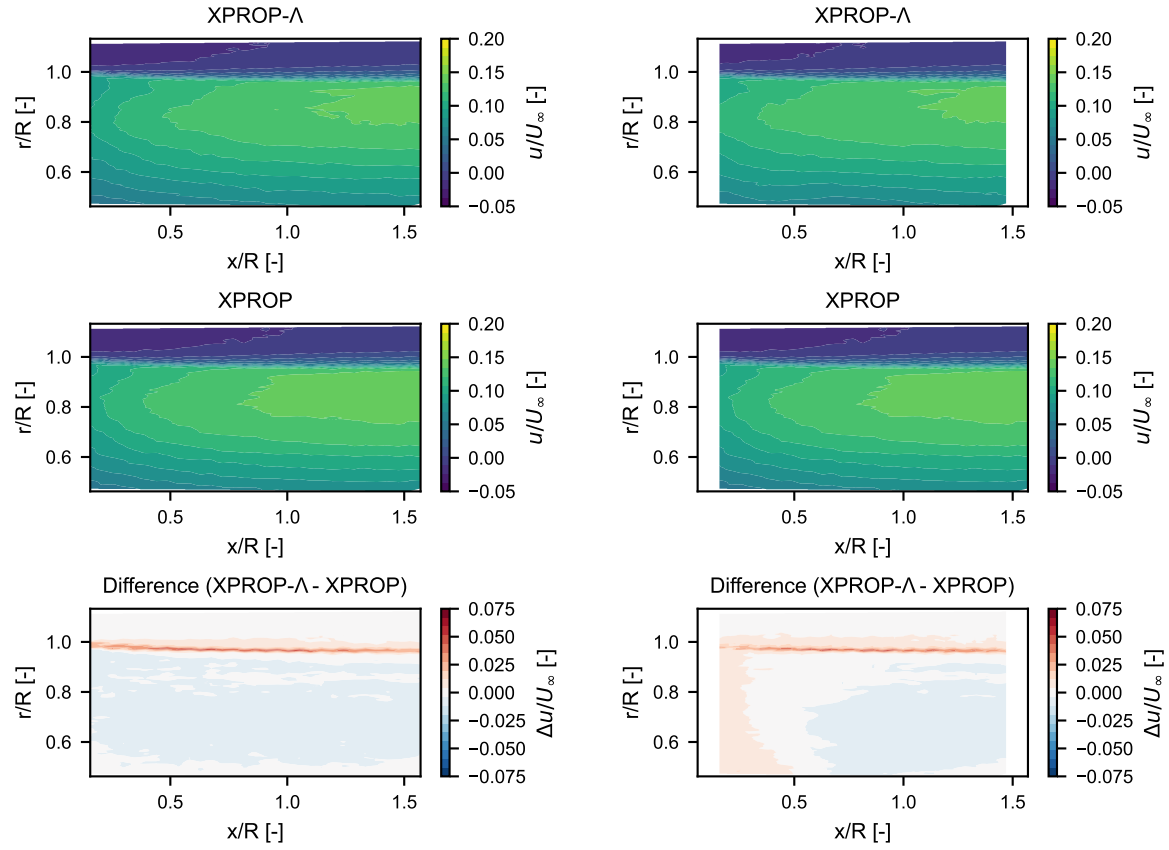

(a) No grid transformation applied

(b) XPROP-Λ data transposed forward by 20.32 mm

Figure D.3: Normalised propeller induced axial velocity u/U_∞, at $\beta = 45°$.

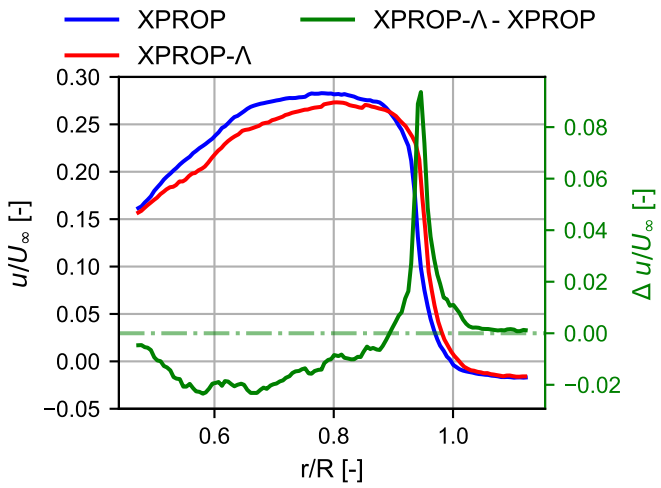

Figure D.4: Spanwise distribution of propeller-induced axial velocity behind the propeller at $\beta = 30°$. Note that there are two different y-axis scales shown. Slice at an axial position of $x/R = 1.41$.

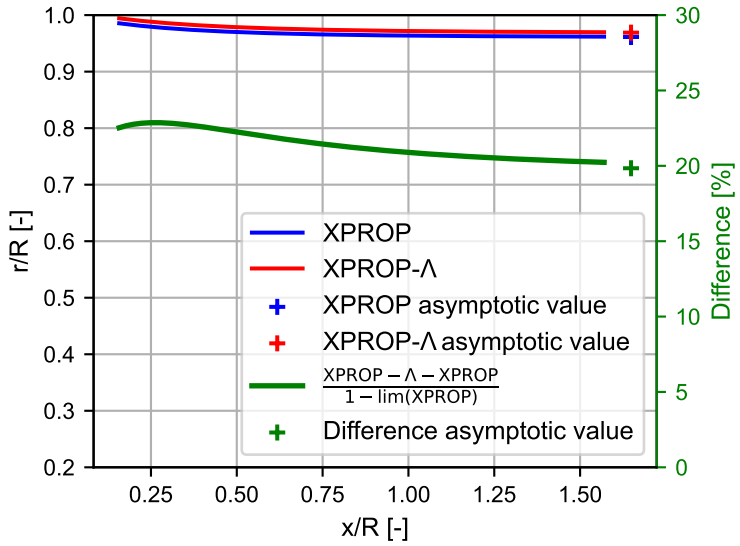

Figure D.5: Comparison of tip vortex locations for $\beta = 45°$. With propeller-off data subtracted and with normalised axes.

E

Additional Comparisons between Computational and Experimental Results

This appendix contains figures that compare the lifting-line results with the experimental results, in addition to those shown in chapter 7.

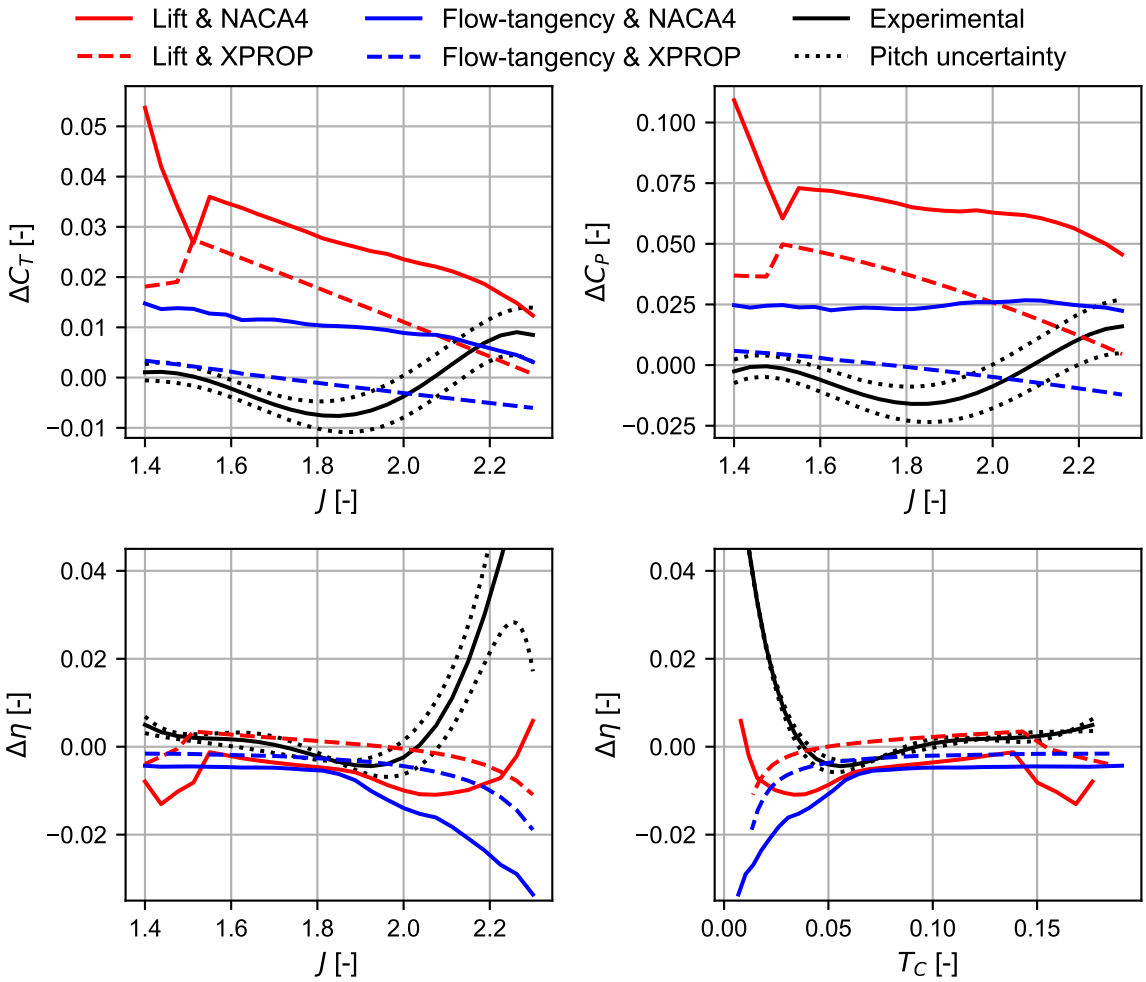

Figure E.1: Difference between XPROP-Λ and XPROP at $\beta = 45°$, shown in C_T, C_P and η. Lines to indicate the uncertainty in the experimental results due to the manual pitch setting are included.

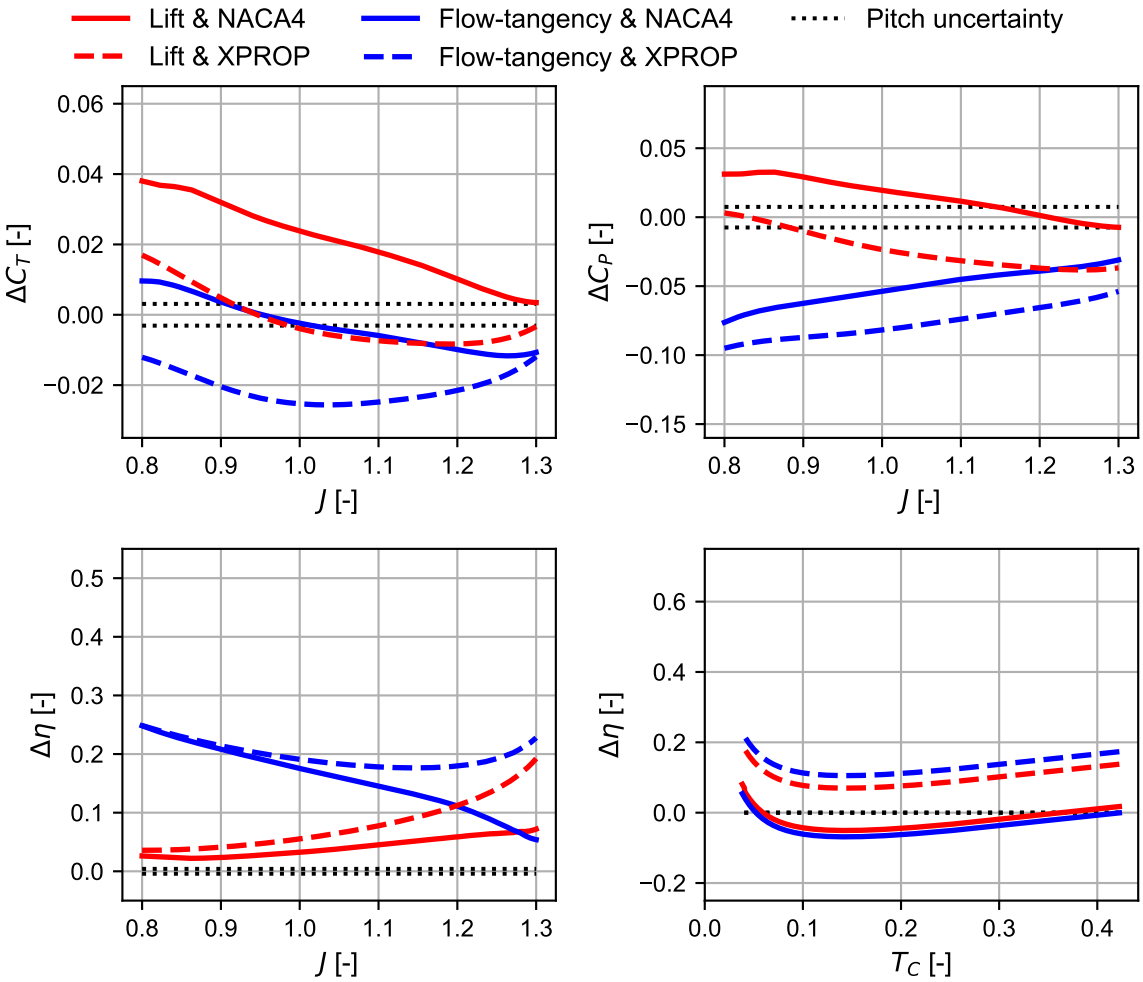

Figure E.2: Difference between the lifting-line methods and experimental results, shown for XPROP-Λ at $\beta = 30°$. Uncertainty margins for the experimental results are included around zero. The difference is expressed as lifting-line − experimental.

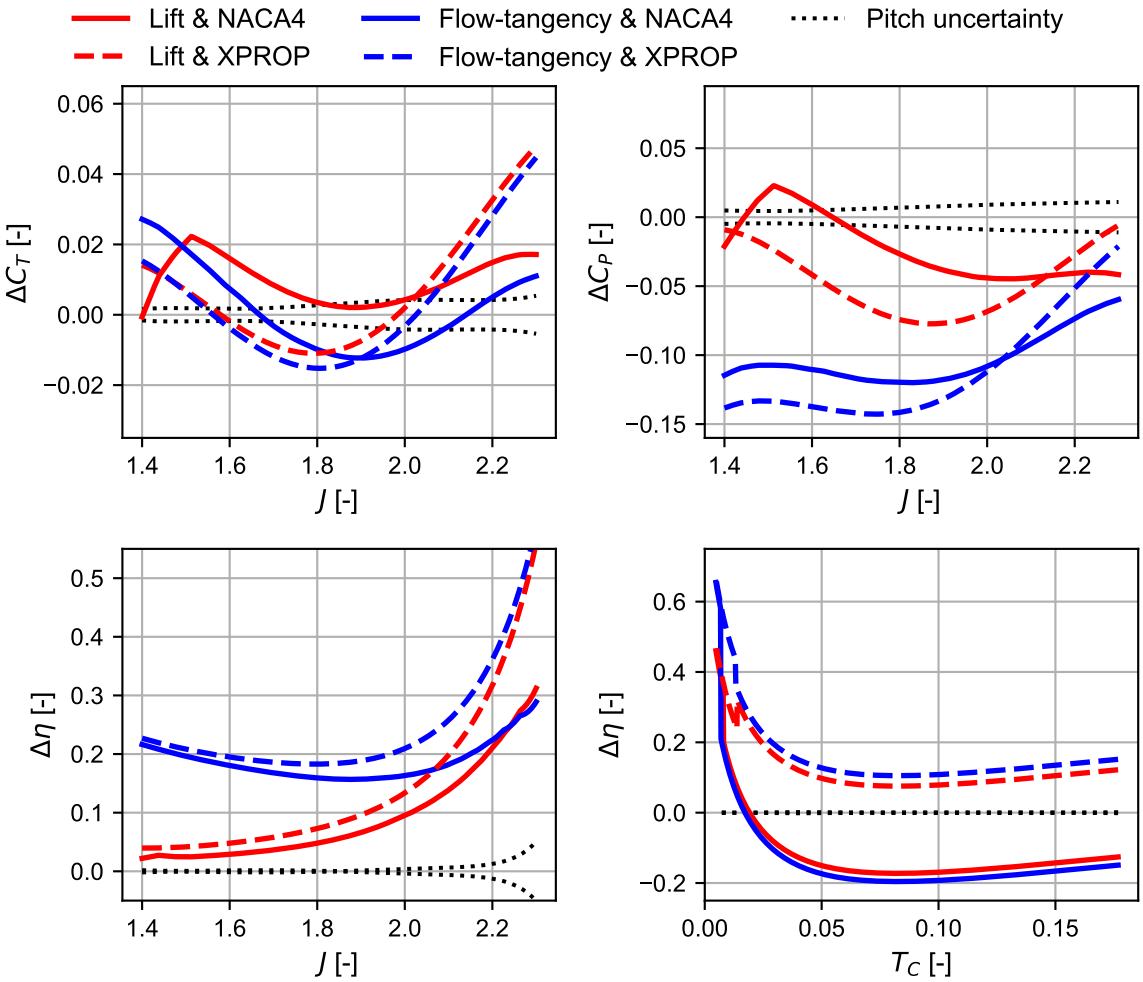

Figure E.3: Difference between the lifting-line methods and experimental results, shown for XPROP at $\beta = 45°$. Uncertainty margins for the experimental results are included around zero. The difference is expressed as lifting-line − experimental.